
Electronic Theses and Dissertations, 2004-2019

2009

Design, Fabrication And Testing Of A Low Temperature Heat Pipe Thermal Switch With Shape Memory Helical Actuators

Othmane Benafan
University of Central Florida

 Part of the [Engineering Commons](#)

Find similar works at: <https://stars.library.ucf.edu/etd>

University of Central Florida Libraries <http://library.ucf.edu>

This Masters Thesis (Open Access) is brought to you for free and open access by STARS. It has been accepted for inclusion in Electronic Theses and Dissertations, 2004-2019 by an authorized administrator of STARS. For more information, please contact STARS@ucf.edu.

STARS Citation

Benafan, Othmane, "Design, Fabrication And Testing Of A Low Temperature Heat Pipe Thermal Switch With Shape Memory Helical Actuators" (2009). *Electronic Theses and Dissertations, 2004-2019*. 1508. <https://stars.library.ucf.edu/etd/1508>

DESIGN, FABRICATION AND TESTING OF A
LOW TEMPERATURE HEAT PIPE THERMAL SWITCH WITH
SHAPE MEMORY HELICAL ACTUATORS

by

OTHMANE BENAFAN
B.S. University of Central Florida, 2008

A thesis submitted in partial fulfillment of the requirements
for the degree of Master of Science
in the Department of Mechanical, Materials and Aerospace Engineering
in the College of Engineering and Computer Science
at the University of Central Florida
Orlando, Florida

Summer Term
2009

© 2009 Othmane Benafan

ABSTRACT

This work reports on the design, fabrication and testing of a thermal switch wherein the open and closed states are actuated by shape memory alloy elements while heat is transferred by a heat-pipe. The motivation for such a switch comes from NASA's need for thermal management in advanced spaceport applications associated with future lunar and Mars missions. For example, as the temperature can approximately vary between 40 K to 400 K during lunar day/night cycles, such a switch can reject heat from a cryogen tank in to space during the night cycle while providing thermal isolation during the day cycle. By utilizing shape memory alloy elements in the thermal switch, the need for complicated sensors and active control systems are eliminated while offering superior thermal isolation in the open state. Nickel-Titanium-Iron (Ni-Ti-Fe) shape memory springs are used as the sensing and actuating elements. Iron (Fe) lowers the phase transformation temperatures to cryogenic regimes of operation while introducing an intermediate, low hysteretic, trigonal R-phase in addition to the usual cubic and monoclinic phases typically observed in binary NiTi. The R-phase to cubic phase transformation is used in this application. The methodology of shape memory spring design and fabrication from wire including shape setting is described. Heat transfer is accomplished via heat acquisition, transport and rejection in a variable length heat pipe with pentane and R-134a as working fluids. The approach used to design the shape memory elements, quantify the heat transfer at both ends of the heat pipe and the pressures and stresses associated with the actuation are outlined. Testing of the switch is accomplished in a vacuum bell jar with instrumentation feedthroughs using valves to control the flow of liquid nitrogen and heaters to simulate the temperature changes. Various

performance parameters are measured and reported under both transient and steady-state conditions. Funding from NASA Kennedy Space Center for this work is gratefully acknowledged.

Dedicated
to
my Parents

ACKNOWLEDGMENTS

First and foremost, I would like to express my sincere gratitude to my advisor Dr. Raj Vaidyanathan for introducing me to graduate research and giving me the opportunity to pursue a Masters degree in Mechanical Engineering, and for his valuable advice and guidance throughout my thesis project and research. My gratitude also goes out to Dr. William U. Notardonato (NASA-KSC) and Dr. Barry J. Meneghelli (ASRC) for involving me in developing a shape memory alloy thermal switch for NASA's thermal management.

I would like to thank Dr. Ali P. Gordon, Dr. Jayanta Kapat and Dr. William U. Notardonato for their valuable advice and for serving on my defense committee. I would also like to thank my office friends and colleagues Shipeng Qiu, R. Mahadevan Manjeri, Matthew D. Fox and Vinu B. Krishnan for responding to my never ending questions and sharing their knowledge in shape memory alloys with me. My sincere gratitude is also extended to the AMPAC administrative staff, Ms. Angelina Feliciano, Ms. Cynthia Harle, Ms. Karen Glidewell, and Ms. Kari Stiles for dealing with all the paperwork and ordering project and lab materials. I also thank Richard E. Zotti of CREOL and Mark D. Velasco of ASRC for their contributions in parts machining and helpful suggestions.

Above all I would like to thank all my friends, my sisters Rabia, Naima, Souad and Kaoutar, my brother Hicham, and Eunice who have advised and encouraged me to sail through this journey at UCF. Finally I humbly thank and dedicate this work to my parents, *Mueha* and *Buiga*, for their boundless love and support, and for their guidance not only in this work but also in everyday decisions.

TABLE OF CONTENTS

LIST OF FIGURES.....	x
LIST OF TABLES.....	xv
LIST OF ACRONYMS/ABBREVIATIONS.....	xvi
CHAPTER ONE: INTRODUCTION.....	1
1.1 Motivation.....	1
1.2 Organization.....	4
CHAPTER TWO: LITERATURE REVIEW.....	5
2.1 Shape Memory Alloys.....	5
2.1.1 Shape Memory Effect.....	6
2.1.2 Superelasticity.....	9
2.2 Applications of Shape Memory Alloys.....	10
2.3 The R-Phase in NiTi System.....	12
2.4 Thermal Switches.....	13
CHAPTER THREE: NiTiFe SHAPE MEMORY ALLOY HELICAL ACTUATORS.....	17
3.1 Helical Spring Analyses.....	17
3.2 Helical Shape Memory Alloy Actuators	19
3.3 Helical Shape Memory Alloy Actuator Design.....	20
3.3.1 Equations in Reduced Form.....	23
3.3.2 Equations in Full Form.....	26
3.3.3 Finite Element Method.....	27

3.3.4	Comparisons Between Elastic Theory and the Finite Element Method	29
3.4	Fabrication of Actuators	38
3.5	Thermal Switch Actuation	42
CHAPTER FOUR: VARIABLE LENGTH TWO-PHASE HEAT PIPE		44
4.1	Overview	44
4.2	Closed Two-Phase Thermosyphon Design	47
4.2.1	Heat Transfer at the Evaporator	47
4.2.2	Heat Transfer at the Condenser	50
4.2.3	Limitations of Two-Phase Thermosyphon	52
4.3	Heat Pipe Fabrication and Assembly	53
4.4	Thermophysical Properties of the Working Fluids	55
CHAPTER FIVE: THERMAL SWITCH ASSEMBLY AND OPERATION		57
5.1	Thermal Switch Components and Final Assembly	57
5.2	Switch Operation	60
CHAPTER SIX: TEST SETUP AND METHODOLOGY		62
6.1	Heat Pipe Evacuation and Charging	62
6.2	Thermal Switch Test Setup	64
6.3	Testing Methodology	71
6.4	Instrumentation and LabVIEW® Data Acquisition	72
6.4.1	Temperature Virtual Instrument	73
6.4.2	Displacement Virtual Instrument	75
6.4.3	Load Virtual Instrument	77

CHAPTER SEVEN: RESULTS AND DISCUSSION.....	79
7.1 Differential Scanning Calorimetry.....	79
7.2 SMA Actuators Temperature Distribution.....	82
7.3 Performance of the Shape Memory Helical Actuators	84
7.4 Performance of the Thermal Switch.....	91
CHAPTER EIGHT: CONCLUSIONS AND FUTURE WORK.....	99
8.1 Conclusions.....	99
8.2 Future Work and Recommendations.....	100
APPENDIX A: DESIGN CALCULATIONS.....	102
A-1 Spring Design Equations and Calculations.....	103
A-2 Comparison of SMA Spring Design Equations.....	108
A-3 Heat Pipe Internal Stress Analysis Equations.....	110
A-4 Heat Transfer Design Equations and Calculations (for R-134a).....	111
A-5 Heat Transfer Design Equations and Calculations (for Pentane).....	116
A-6 Liquid Pool Calculations (with Pentane): Film Thickness Calculation.....	120
APPENDIX B: DESIGN DRAWINGS.....	124
REFERENCES.....	143

LIST OF FIGURES

Figure 2.1:	Atomic arrangements for the shape memory effect of a binary alloy: (a) undeformed austenite (b) twinned martensite (prior to deformation) (c) detwinned martensite (following deformation) (d) shape recovery to austenite after heating.....7
Figure 2.2:	Transformation temperatures and hysteresis associated with the shape memory effect.....8
Figure 2.3:	Superelasticity: (a) austenite (b) stress-induced martensite (c) shape recovery on reverse transformation to austenite.....9
Figure 2.4:	Superelastic behavior during loading and unloading at constant temperature: ABC during loading resulting in the forward phase transformation; DEF during unloading resulting in the reverse transformation.....10
Figure 2.5:	Shape memory alloy actuated variable geometry chevrons [26].....11
Figure 2.6:	Example of a differential thermal expansion thermal switch. (a) open-state at high temperature (b) closed-state at low temperature [31].....14
Figure 2.7:	Example of a gas-gap thermal switch with an adsorption pump [32].....15
Figure 2.8:	Example of a sealed bellows thermal switch [33].....16
Figure 3.1:	SMA helical spring length: (a) high temperature phase (b) low temperature phase.....20
Figure 3.2:	Global and local reference coordinate systems for the spring.....21
Figure 3.3:	Free body diagram (a) resultant moment (b) resultant force.....21
Figure 3.4:	Finite element mesh used to model spring.....28
Figure 3.5:	Shear stress distribution across coil section in a helical SMA spring: (a) FEA (b) prediction from theory (spring axis to the right).....30
Figure 3.6:	$\tau_{\theta z}$ shear stress distribution for a spring cross-section with small helix angle $\alpha \approx 2^\circ$ (austenite, spring axis to the right).....31
Figure 3.7:	Comparison of maximum shear stress ($\tau_{\theta z}$) using elastic theory and FEA (austenite).....32

Figure 3.8:	σ_z distribution for $F= 9$ N in helical coil (austenite).....	33
Figure 3.9:	σ_z as a function of helical angle for various loads (austenite).....	34
Figure 3.10:	Spring displacement in tension for small helix angle $\alpha \approx 2^\circ$ (austenite, bottom of spring fixed and load applied at the top end).....	35
Figure 3.11:	Correlation between spring extension and helical angle (austenite).....	36
Figure 3.12:	Correlation between spring extension and helical angle (R-phase).....	37
Figure 3.13:	Helical shape memory alloy actuators and spring winding mandrels.....	38
Figure 3.14:	Mandrel containing coiled SMA wire in the furnace.....	39
Figure 3.15:	Spring geometry 3 after shape setting and final electrical discharge machining to increase contact.....	40
Figure 3.16:	Load-extension response of the SMA springs at room temperature.....	41
Figure 3.17:	Arrangement of the shape memory (dark shading) and bias springs (light shading) (a) at high temperature with the SMA spring pre-loaded and the bias spring compressed in the open or “off” position; and (b) at low temperature with the SMA spring extended and the bias spring in the closed or “on” position (c) Sectional view of the shape memory and bias springs.....	43
Figure 3.18:	Arrangement of the shape memory (dark shading) and bias springs (light shading) in the switch (a) at high temperature with the SMA spring pre-loaded and the bias spring compressed in the open or “off” position; and (b) at low temperature with the SMA spring extended and the bias spring in the closed or “on” position.....	43
Figure 4.1:	Sections in a heat pipe involving two-phase flow.....	45
Figure 4.2:	Critical regions in a pool boiling curve [70].....	48
Figure 4.3:	Assembly of the closed two-phase thermosyphon: (a) schematic, with the regions <i>A</i> , <i>B</i> , and <i>C</i> being the condensation, adiabatic, and evaporation regions, respectively (b) final assembly.....	54
Figure 5.1:	Schematic of final thermal switch assembly (dimensions in mm).....	58

Figure 5.2:	Final thermal switch assembly. The bias spring in the front was removed to show the position of the SMA spring.....	59
Figure 5.3:	Principle of switch operation: (a) The open or “off” position during a lunar day (hot) (b) and the closed or “on” position during a lunar night (cold).....	61
Figure 6.1:	Pressure manifold for heat pipe evacuation and charging.....	63
Figure 6.2:	Heat pipe evacuation /charging setup.....	64
Figure 6.3:	Test stand with thermal switch: (a) schematic (b) final setup.....	65
Figure 6.4:	Single-loop cooper tube around thermal switch.....	66
Figure 6.5:	Fabrication of the single-loop copper tube.....	66
Figure 6.6:	Glass bell jar with instrumentation feedthroughs.....	69
Figure 6.7:	Thermal switch inside the bell jar fixture.....	70
Figure 6.8:	Thermal switch and single-loop cooling coils connected to liquid nitrogen lines.....	70
Figure 6.9:	Switch in instrumented vacuum bell jar setup for testing. LabVIEW [®] software was used for data acquisition and control of the test temperature conditions (heater and flowing liquid nitrogen through coils).....	71
Figure 6.10:	LabVIEW [®] data acquisition system.....	72
Figure 6.11a:	Virtual instrument block diagram for temperature measurement.....	73
Figure 6.11b:	Virtual instrument front panel for temperature measurement.....	74
Figure 6.12a:	Virtual instrument block diagram for displacement measurement.....	75
Figure 6.12b:	Virtual instrument front panel for displacement measurement.....	76
Figure 6.13a:	Virtual instrument block diagram for acquiring load cell data (NI code).....	77
Figure 6.13b:	Virtual instrument front panel for acquiring load cell data (NI code).....	78
Figure 7.1:	Differential Scanning Calorimetry curves of the shape set NiTiFe wire.....	80
Figure 7.2:	DSC response of NiTiFe in the as-received, shape set and tested conditions.....	81

Figure 7.3:	Cooling and heating rates of the four SMA helical springs.....	82
Figure 7.4:	Temperature distribution along the length of the SMA spring.....	83
Figure 7.5:	Experimental and theoretical load-extension response of the springs in the austenite and R-phase and the bias springs.....	84
Figure 7.6:	Stroke-temperature response of the shape memory helical actuators. The transformation temperatures R_f , R_s , A_s , and A_f under the bias load are -15.2, -75.5, -61.3 and 3.1 ± 2 °C respectively.....	86
Figure 7.7:	Stroke-time response of the shape memory helical actuators to assess open-loop strains. After the third cycle from room temperature to -100 °C at 10°C/min, the open loop axial deformation is negligible as shown by δ_3 for an overall switch extension of 5 mm.....	86
Figure 7.8:	Stroke-temperature response of the shape memory helical actuators under varying bias loads. F_b denotes the total bias force from stainless steels springs, bellows and weight of the heat pipe. The maximum stroke for (a), (b), (c), and (d) are 1.85, 2.94, 5.0, and 7.13 mm, respectively. The graphs y-axes are scaled identically.....	87
Figure 7.9:	Stroke-time response of the shape memory helical actuators under varying bias loads. F_b denotes the total bias force from stainless steels springs, bellows and weight of the heat pipe. The graphs y-axes are scaled identically.....	88
Figure 7.10:	Shear stress evolution with temperature in a spring during 5 mm extension against a total bias load of 39 N.....	89
Figure 7.11:	Effect of load on transformation temperatures.....	90
Figure 7.12:	Heat transfer rate as a function of contact pressure.....	92
Figure 7.13:	Contact force with switch extension. The minimum required contact force is from Fig. 7.12.....	92
Figure 7.14:	Baseline test with no working fluid (conduction only). An average heat transfer rate of 3.6 W was obtained.....	94
Figure 7.15:	Heat throughput using pentane: (a) F.R. = 0.5, Q = 8.6 W (b) F.R. = 0.7, Q = 11.3 W (c) F.R. = 0.9, Q = 12.9 W (d) F.R. = 1.5, Q = 7.1 W.....	95
Figure 7.16:	Heat throughput using pentane: (a) F.R. = 0.5, Q = 7.1 W (b) F.R. = 0.7, Q = 9.1 W (c) F.R. = 0.9, Q = 10.2 W (d) F.R. = 1.5, Q = 5.8 W.....	96

Figure 7.17:	Heat transfer rate with fill ratio, with pentane and R-134a as working fluids in the heat pipe. L_f is the liquid pool length and L_e is the length of the evaporator.....	97
Figure 7.18:	Average heat transfer rate using pentane.....	98
Figure 7.19:	Average heat transfer rate using R-134a.....	98

LIST OF TABLES

Table 3.1:	Mechanical properties of NiTiFe used in the analytical and FEM models	28
Table 3.2:	NiTiFe Spring dimensions used in the analytical and FEM models.....	28
Table 3.3:	Shape memory alloy spring geometries (wire diameter 2.159 mm).....	40
Table 3.4:	Shape memory alloy spring constants (wire diameter 2.159 mm).....	40
Table 4.1:	Thermophysical saturation properties for pentane (liquid phase).....	55
Table 4.2:	Thermophysical saturation properties for pentane (vapor phase).....	56
Table 4.3:	Thermophysical saturation properties for R-134a (liquid phase).....	56
Table 4.4:	Thermophysical saturation properties for R-134a (vapor phase).....	56
Table 7.1:	Transformation temperatures of NiTiFe in the as-received, shape set and tested conditions.....	81

LIST OF ACRONYMS/ABBREVIATIONS

A _f	Austenite finish
A _s	Austenite start
CTPT	Closed Two-Phase Thermosyphon
DSC	Differential Scanning Calorimetry
EDM	Electrical-Discharge Machining
F.R.	Fill Ratio
KSC	Kennedy Space Center
LOX	Liquid Oxygen
M _f	Martensite finish
M _s	Martensite start
NASA	National Aeronautics and Space Administration
NI	National Instruments
NiTi	Nickel-Titanium (alloy)
NiTiFe	Nickel Titanium Iron (alloy)
R _f	R-phase finish
R-phase	Rhombohedral-phase
R _s	R-phase start
SE	Superelasticity
SMA	Shape Memory Alloy
SME	Shape Memory Effect

CHAPTER ONE: INTRODUCTION

1.1 Motivation

The need for thermal management in both ground and space-based aerospace applications has gained greater interest in the last decade. Earth orbiting spacecrafts and future outposts on the moon and Mars contain structures that require effective thermal control. Heat exchangers and other heat rejection systems are currently used in high temperature applications, but thermal solutions are limited in the low temperature regime where there are specific needs, e.g., to minimize or eliminate cryogen boil-off and parasitic heat loads, to transfer heat on-demand in cases where there are restrictions on the number of chillers or coolers, etc., among others. Among many devices used to solve these problems, thermal switches have been at the forefront. Gas-gap, paraffin, and differential thermal expansion thermal switches have been developed and used [1-4]; however, these devices usually require external sensors, electric heaters or pumps, and do not integrate sensor and actuator capability in a single mechanism. Shape memory alloys (SMAs) are materials that integrate both sensory and actuation functions due to a temperature-induced solid-state phase transformation that can bring about shape changes against external loads. These “smart” alloys recover considerable inelastic distortion (up to 8% strain) against large stresses (up to 500 MPa) associated with the shape memory effect (SME) and pseudo-elasticity (stress removal recovery) [5-10]. Among many classes of shape memory alloys, near equi-atomic NiTi is a commonly used SMA owing to its favorable mechanical properties [11], but devices that incorporate binary NiTi are limited to operating near room temperature. The

transformation in NiTi occurs between a higher temperature cubic phase called austenite phase and a lower temperature monoclinic phase called martensite phase and has a hysteresis associated with it. Addition of a third element such as iron (Fe) introduces a stable intermediate trigonal R-phase with improved fatigue response and reduced hysteresis while suppressing the phase transformation and shifting it to lower temperatures [12-17]. Strains associated with the R-phase are typically limited to about 1% and hence helical spring SMA elements are used in this work to attain large strokes and adequate work output. Helical actuators provide greater strokes and uniform stress distribution when compared to other element forms such as strips (e.g., Ref. [18]). In addition, these novel actuators are lightweight and compact in size compared to the conventional actuators such as electric motors, hydraulic cylinders, or pneumatic actuators. SMA helical actuators have further advantages in space applications; for instance, they operate in a spark-free way avoiding any faulting or ignition of electrical components that can interrupt the continuity of operation.

Previously, low temperature shape memory alloy thermal switches were developed and tested at the University of Central Florida (UCF) based on conduction [18, 19]. These conduction switches were designed for use in space applications for zero boil-off control, heat transfer between two cryogenic storage tanks and parasitic heat load reduction from secondary redundant cryocoolers. Use of a variable length, two-phase heat pipe promotes heat acquisition, transport and rejection via evaporation and condensation in addition to conduction. Two-phase heat pipes are advantageous in that they offer enhanced heat transfer and allow reductions in component weight and volume without decreasing performance. Furthermore, two-phase heat pipes are self-contained without any pumping mechanism thereby eliminating the need for external pumps.

Since heat pipes do not require large contact areas for efficient heat transfer, parasitic heat loads are minimized due to complete thermal isolation and low surface radiation in the open or “off” position.

Thus the objective of this work is to combine low temperature helical SMA actuators with a variable length, two-phase heat pipe in a thermal switch to meet NASA’s thermal management needs. A heat pipe incorporated in such switches can provide heat transfer involving two-phase flow via evaporation and condensation of the working fluid. The ability of the switch to alternate between the closed or “on” and the open or “off” states without external sensors and mechanisms potentially finds direct applications in advanced spaceport technologies associated with future lunar and Mars missions. The proposed passive control SMA thermal switch eliminates the need for external mechanical means for actuation or pumping fluid making it an efficient device and a less complicated system to integrate in space structures.

Procedures related to the design, construction, combination of parts and final assembly are presented. Experiments were done to quantitatively obtain performance parameters such as deflection curves, force output, and heat transfer rates. Data was collected while testing under vacuum conditions in a sealed glass bell jar with multiple instrumentation feedthroughs for thermocouples, the load cell, the linear encoder, heating pads, liquid nitrogen flow, vacuum valves, and the viewing port. LabVIEW[®] was used for data acquisition and control of the test temperature conditions. Experimental results were compared with analytical and computational results where possible.

1.2 Organization

The work presented is subdivided into chapters organized as follows: Chapter 2 is an introduction to shape memory alloys along with their applications. A brief introduction to thermal switches and their operation is also presented. Chapter 3 presents the design and fabrication of the low temperature shape memory alloy helical actuators used based on spring theories and the finite element method. Chapter 4 presents the design methodology and fabrication of a gravity-assisted two-phase heat pipe. The approach used to quantify the heat transfer rate at both ends of the pipe is outlined. Chapter 5 describes the final switch assembly and operation. Chapter 6 gives a brief overview of the test setup, instrumentation and procedures used to quantify the thermal switch performance parameters. Chapter 7 presents results and discusses material characterization, helical actuators performance and heat transfer aspects. Finally, Chapter 8 presents conclusions and recommendations. Relevant design calculations and machine drawings are included in the Appendix.

CHAPTER TWO: LITERATURE REVIEW

Shape memory alloys have received considerable interest in the last two decades due to their favorable thermo-mechanical characteristics, leading to their use in various applications ranging from medical to aerospace industries. Among many classes of shape memory alloys, binary nickel-titanium alloys exhibiting both shape memory and superelastic behavior are commonly used. This chapter describes the phase transformation in NiTi alloys and metallurgical aspects. Use of an intermediate R-phase for actuation at low temperatures as a result of element addition is described. An introduction to thermal switches and their applications is outlined in the last section of this chapter.

2.1 Shape Memory Alloys

Shape memory alloys are novel materials that remember their pre-deformed shape by undergoing a reversible solid-state phase transformation induced by changes in temperature and/or stress. This phase change is first-order and is characterized by no change in chemical composition or atomic diffusion, and takes place in the form of shearing deformation of the crystallographic structure between a low-symmetry so-called martensite phase and a high-symmetry so-called austenite parent phase. Depending on stoichiometry, the austenitic phase has a cubic (B2) structure and it is usually associated with high-temperatures; alternatively, the martensitic phase has a monoclinic (B19') structure and is associated with low-temperatures. Shape memory alloys can recover considerable inelastic deformation (up to 8% uniaxial strain) against large stresses (up to 500 MPa) which gives them the ability to be used as actuators [11].

Among many classes of SMAs, NiTi alloys and copper based alloys have been at the forefront due to large strain recovery coupled with superior force generation when compared to other alloy systems. Observations of SMA behavior were first investigated and discovered in 1932 in Au-Cd system by Arne Ölander [20]. In 1938, Greninger and Mooradian observed the shape memory effect in copper-zinc (Cu-Zn) and copper-tin (Cu-Sn) alloys [21]. Around 30 years later in 1962, such behavior was discovered in nickel-titanium (NiTi) in several studies conducted at the U.S. Naval Ordnance Laboratories [22]. Since then, extensive research has been devoted to better understand the physical and mechanical properties of these materials.

The shape change in SMAs results from thermal or stress induced transformation. Thermally induced phase transformation, resulting in the shape memory effect (SME), occurs by cycling the material between high and low temperatures with or without a pre-stress. As the material transforms back from low to high temperature, the martensite phase becomes unstable and transforms back to the parent phase (austenite) recovering all the macroscopic strains. The stress-induced transformation, resulting in superelasticity (SE), occurs by loading the material in its austenite phase to form stress-induced martensite (SIM). Upon unloading, the material goes back to its original shape without permanent plastic deformation. Details of these two behaviors are discussed in the next sections.

2.1.1 Shape Memory Effect

The shape memory effect refers to the ability of the alloy to recover or “remember” its original shape by increasing the temperature while in its low temperature phase. When cooling from the stiffer austenite phase, the material undergoes a displacive martensitic transformation to

a more compliant martensite phase where the material can be macroscopically deformed by detwinning. Upon heating, a reversible transformation takes place resulting in recovery of the accumulated strain. Figure 2.1 illustrates the transformation cycle associated with the shape memory effect of a binary system (e.g., NiTi). As the unstressed material is cooled from the austenite phase (Fig. 2.1a), the material transforms to a twinned martensite structure without macroscopic deformation due to the lower symmetry (Fig. 2.1b). During loading, (e.g., tension, compression, shear, torsion), detwinned martensite is formed to accommodate the strains resulting in macroscopic deformation (Fig. 2.1 c). Finally, unloading and heating to the initial state cause a reverse transformation to the parent phase leading to complete shape recovery (Fig. 2.1d). Detwinned martensite can also be formed directly, without twinning, if the material is loaded in the austenite phase before cooling.

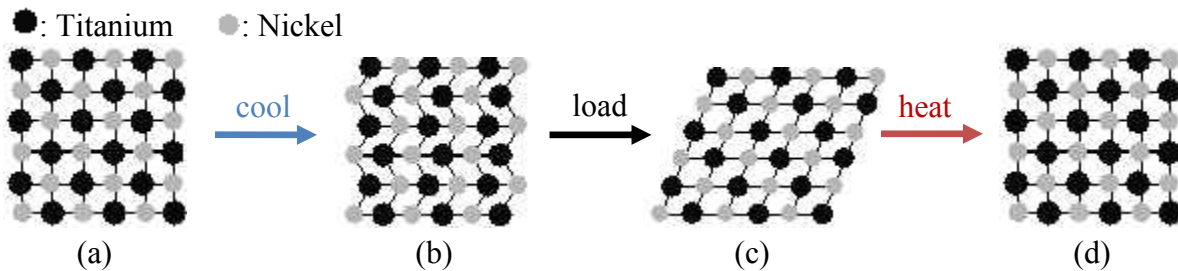


Figure 2.1: Atomic arrangements for the shape memory effect in a binary alloy: (a) undeformed austenite (b) twinned martensite (prior to deformation) (c) detwinned martensite (following deformation) (d) shape recovery to austenite after heating

The thermally activated transformation can be characterized by four transformation temperatures while cycling between the austenite parent phase and the martensite phase. When cooling from the austenite phase, the first appearance of the martensite phase takes place at the martensite start temperature denoted by M_s ; at this point the material exists in a hybrid phase. Further cooling to where no more transformation is observed is considered to be the martensite

finish temperature, M_f , where the austenite phase has completely transformed to martensite. Heating the material results in a reverse transformation; the transformation starts at the austenite start temperature, A_s , as the material recovers the transformation strains up to the austenite finish temperature, A_f . This process is shown graphically in Fig. 2.2. In this work, the transformation temperatures were measured using the linear intercept method by drawing tangent lines along the transformation curve (Fig. 2.2.). The difference between the starting temperatures for the forward and backward transformation (M_s and A_s) is the hysteresis. This hysteresis can be as much as 40 to 50 °C for NiTi and as low as a few degrees for NiTiFe.

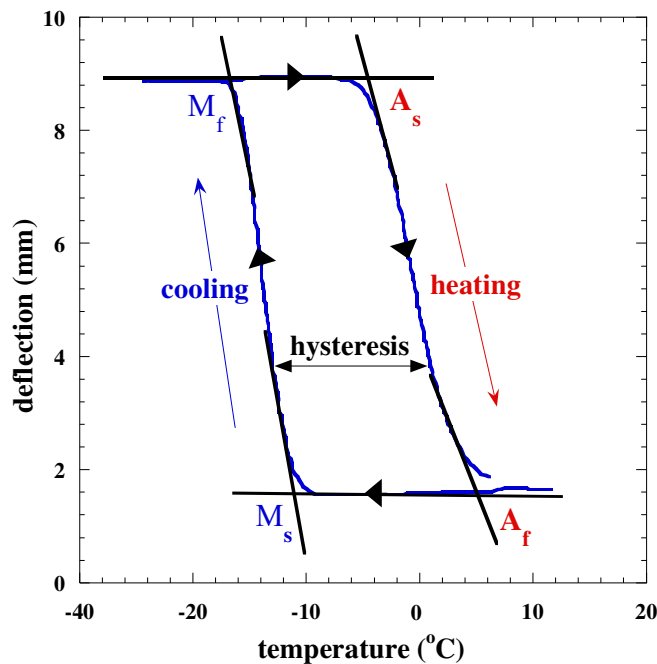


Figure 2.2: Transformation temperatures and hysteresis associated with the shape memory effect

There are two manifestations of the shape memory effect: one-way and two-way shape memory effect. The one-way effect is when the material remembers only its original shape and returns to it upon heating. This one-directional mechanism requires some external bias load to

take the material to the desired deformed shape at low temperatures (e.g., biased actuators). On the other hand, two way shape memory refers to the material ability to remember its deformed and original shape in both phases.

2.1.2 Superelasticity

Superelasticity or pseudoelasticity behavior refers to the ability of shape memory alloys to transform to martensite during loading at temperatures above A_f . During loading, the stress-induced transformation leads to high strain generation as austenite transforms to stress-induced martensite without plastic deformation. Upon unloading, the strain is completely recovered at temperatures above the austenite finish temperature due to the reverse transformation. During this transformation, there is no twinned martensite and macroscopic deformation is primarily obtained during the phase transformation due to the applied stress (Fig. 2.3).

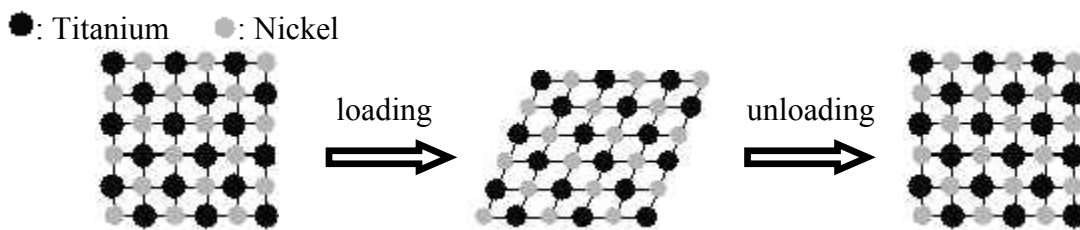


Figure 2.3: Superelasticity: (a) austenite (b) stress-induced martensite (c) shape recovery on reverse transformation to austenite

Figure 2.4 shows a typical superelastic loading cycle under isothermal conditions. Starting from a temperature above A_f with no load, a stress is applied that causes elastic deformation (A) followed by formation of stress-induced martensite (B). Further loading results in elastic deformation of the detwinned martensite (C). During unloading, martensite elastically

unloads to a point (D) where reverse transformation to stable austenite takes place recovering all the strains (E) to be finally followed by elastic recovery (F).

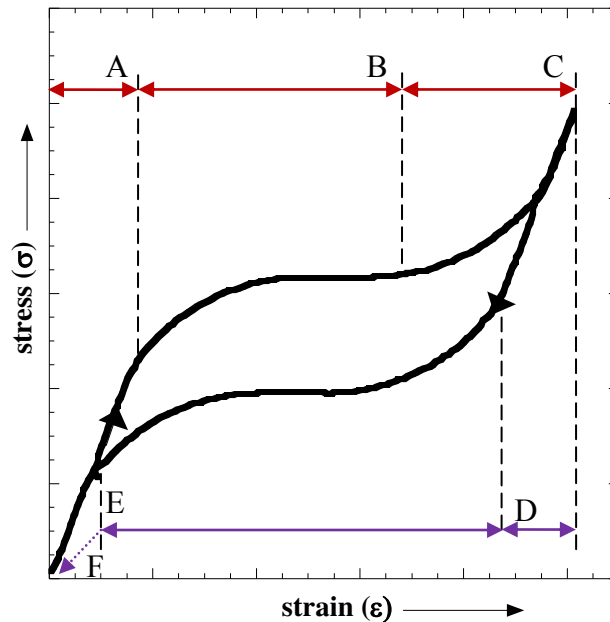


Figure 2.4: Superelastic behavior during loading and unloading at constant temperature: ABC during loading resulting in the forward phase transformation; DEF during unloading resulting in the reverse transformation

2.2 Applications of Shape Memory Alloys

Favorable thermo-mechanical properties of shape memory alloys have led them to be used in a variety of applications that require reliability and multi-functionality. Over the past decades, the ability of SMAs to convert thermal energy into mechanical work (e.g., actuators) has gained attention in applications ranging from medical fixtures to aerospace and naval equipments. The field of aeronautics integrated many devices with SMAs. In 1969, hydraulic pipe couplings were introduced by Raychem Corporation using low temperature SMAs to join pipes in the Grumman Aerospace Corporation F-14 jet fighters [23]. In 1994, active control

SMA release bolts developed by the TiNi Alloy Company were used for release mechanisms in the spacecraft Clementine [24]. Shape memory alloy powered adaptive aircraft inlet internal walls was employed by NASA Langley Research Center (NASA LaRC) and the Office of Naval Research (ONR) in The Smart Aircraft and Marine Project System DemonstratiON (SAMPSON) program [25]. Boeing designed and flight tested a variable geometry chevron that integrates SMA beam components as shown in Fig. 2.5 [26]. The goal of chevrons is to eliminate engine noise, and in this case, SMA elements are used to alter their geometry.



Figure 2.5: Shape memory alloy actuated variable geometry chevrons [26]

Other aerospace applications that incorporate SMAs are fixed-wing aircraft applications, landing gears, flaps and more. SMAs have also been used in spacecrafts for vibration damping and actuation applications.

Another major field that uses shape memory alloys is the medical industry. Applications such as orthodontic wires, stents, lengthening limbs and cardiovascular and orthopedic applications all integrate SMAs in some form to help provide better performance. There are many other fields besides the ones mentioned here that benefit from advantageous attributes of SMAs such as transportation industry, civil industry and every day products and more. However, they are not described in detail since the shape memory effect rather than the superelastic effect is the focus of this thesis.

2.3 The R-Phase in NiTi System

Among many classes of shape memory alloys, near equi-atomic NiTi alloys are the most commonly used. These alloys exhibit both the shape memory effect and superelastic behavior as they transform from the high temperature, cubic (B2) austenite phase to the low temperature, monoclinic (B19') martensite phase. In most cases, the transformation temperatures of NiTi occur between room temperature and 100 °C accompanied by a wide hysteresis of about 40 °C. Applications that require low temperature operation cannot use these alloys; consequently, modification of binary NiTi is necessary to shift the transformation temperatures and reduce the hysteresis to fit specific limits. Formation of a stable intermediate R-phase with improved fatigue response and reduced hysteresis, suppresses the phase transformation and shifts it to lower temperatures (below 0 °C) [13, 14]. The R-phase can be introduced by annealing below the recrystallization temperature after cold-working [27, 28], ageing after solution treatment, thermal cycling or adding a ternary element such as iron [16]. Several studies have shown the multi-stage R-phase transformation to be transient in binary NiTi and nickel rich systems that do not suit

commercial applications [29, 30]. Addition of a ternary alloy such as Fe, on the other hand, offers phase transformations at low temperature with stable characteristics. The cubic austenite to trigonal R-phase transformation in NiTiFe is associated with a narrow hysteresis (~ 2 °C) and better fatigue life due to low strains ($\sim 1\%$) when compared to the B19' phase.

2.4 Thermal Switches

Demand for effective thermal control devices for space and ground-base applications has grown due to advanced technological thermal management needs. In the aerospace industry, thermal control is accomplished via single-phase cooling systems or two-phase technologies such as capillary pumped loops (CPLs) or loop heat pipes (LHPs), among others. In most cases, it is desirable to thermally isolate the system to create an adiabatic environment but most thermal control devices do not provide such flexibility. The use of thermal switches to couple/decouple heat sinks from the heat source has proven to be advantageous. Most of the thermal switches have the objective of affecting heat flow to reduce or eliminate parasitic heat loads, isolate vibrations and provide high heat flux during engagement. A wide range of thermal switches have been developed for application at temperatures ranging from 673 °C to -272 °C [1-4]. Mechanical thermal switches such as differential thermal expansion switches (Fig. 2.6) are based on the differences in the coefficient of thermal expansion (CTE) of two materials. During cooling, the outer element comprising of the high CTE material contracts around a low CTE material causing the switch to make contact [31]. As the temperature is elevated, the high CTE material expands more than the low CTE material causing thermal isolation. Heat transfer through the switch is

based on conduction between the two bodies during thermal contact. A disadvantage of such switches is the possibility of cold welding during contact over long time periods. Another example of a thermal switch is the gas-gap heat switch that operates by filling or evacuating a gap between the surfaces with gas using external pumps [32]. When the gas is filled, heat transfer is enabled across the gap due to convection associated with gas flow; conversely, during evacuation, convection is interrupted discontinuing heat transfer. In some switches, contact between the two surfaces is permanent, and in some cases, the mechanical contact is controlled by an external actuation mechanism.

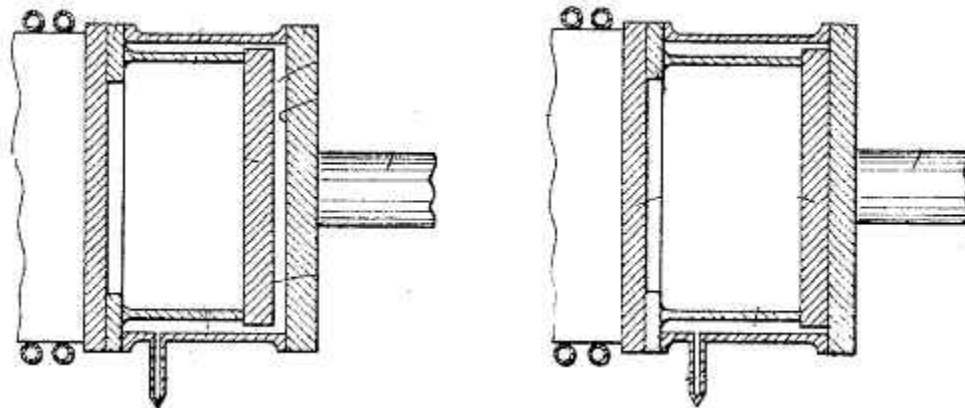


Figure 2.6: Example of a differential thermal expansion thermal switch. (a) open-state at high temperature (b) closed-state at low temperature [31]

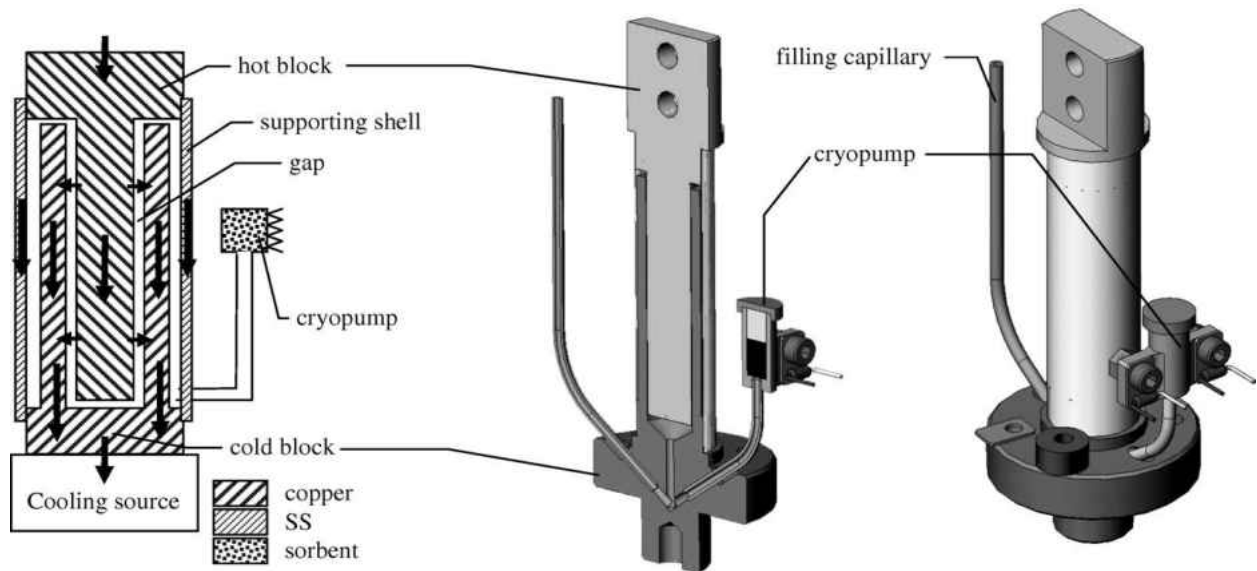


Figure 2.7: Example of a gas-gap thermal switch with an adsorption pump [32]

Gas-gap heat switches depend on external mechanisms such as actuators or pumps making them more complex and bulky.

Another common heat switch is a fluid-loop thermal switch. In these devices, heat flow is controlled by heat exchangers, pumps and working fluids that gain heat from one location and reject it at a different location. Examples of such devices include capillary pumped loops, heat pipes and pumped gas loops. Fig. 2.8 shows a thermal switch based on the principle of fluid-loop operation [33]. An extendible bellow contains a working fluid on the inside forming a sealed heat pipe type mechanism. Temperature variation results in pressure changes inside the bellow that expands or contracts to make or break contact.

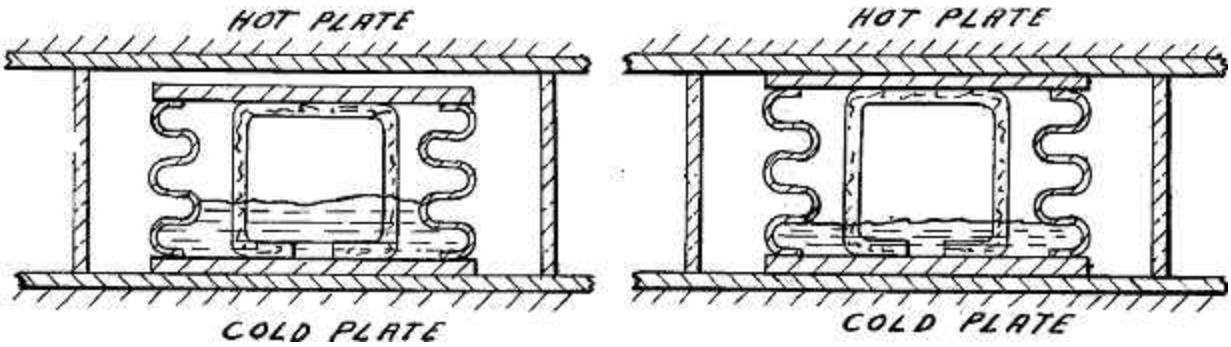


Figure 2.8: Example of a sealed bellows thermal switch [33]

Other types of switches have been developed for use at high temperatures or cryogenic regimes. However, most of these switches require some external mechanisms such as fluid pumps or mechanical actuators for proper operation. In this thesis, an SMA actuated heat pipe switch is designed, fabricated and tested. Having the combined ability of sensing and actuating, the developed SMA thermal switch eliminates the need for any external mechanisms providing for simpler design.

CHAPTER THREE: NiTiFe SHAPE MEMORY ALLOY HELICAL ACTUATORS

Shape memory alloy (SMA) actuators have received renewed interest in the last two decades due to their unique thermo-mechanical characteristics. These ‘smart’ actuators combine both sensory and actuation capability in a single mechanism due to a temperature induced solid-state phase transformation that can bring about shape changes against external loads. Reduced helical spring design equations have been applied to design shape memory alloy compression and tension helical actuators [34, 35]. This approach yields erroneous approximations due to the small helix angle assumption and associated neglect of the bending and direct shear effects on the helix. This chapter reports on the effect of the helix angle on SMA helical springs by direct comparison between the reduced equations, equations in full form, a finite element model (FEM), and experimental results. The effects of the spring’s geometry including the coil radius, helix angles and extension under load are examined. Due to significant changes in the shear modulus during the martensitic phase transformation (~300%), the response of both the high temperature cubic, B2, austenitic phase as well as the low temperature trigonal R-phase are quantified. Axial extensions and the accompanying stress distributions along the coil are also presented.

3.1 Helical Spring Analyses

Helical tension/compression springs have been widely used in a variety of applications due to their elastic ability to extend or contract and recover upon application or removal of

functional loads. Helical springs are used as mechanical devices that store elastic potential energy and generate stroke as a function of applied load. However, advanced thermo-mechanical technologies require helical springs to work as actuators with the ability to sense and actuate in response to other parameters in addition to load. Shape memory alloy helical springs are advantageous over conventional spring materials in their thermo-elastic response. They couple thermal and mechanical effects and produce adequate actuation energy densities. Shape memory alloy helical springs generate stroke as a function of applied stress and/or temperature making them suitable for sensing and actuating applications where changes in temperature are a factor.

It is as important to decide on the correct theoretical approach with minimum assumptions to design a helical actuator. A frequently adopted approach for SMA helical spring design has been the application of the reduced form of torsion and bending theories. These simplified formulations are insufficient to capture the bending and helix effects resulting in deviations between experimental and theoretical predictions. Several approaches have been adopted to solve the static response of helical springs, e.g., the transfer matrix method (TMM) [36], the boundary element method (BEM) [37-39], or the finite element method (FEM) [40-42]. However, the implementation of the analyses has mostly ignored the effect of the helical angle for simplification. In this work, effects of the helix angle in SMA helical springs were investigated by direct comparison between the reduced equations, equations in full form, a finite element model (FEM) and experimental results. Geometrical and displacement constraints are described with the aid of a free body diagram. The displacement and stress distributions along the coil are quantified for both the austenite and the R-phase.

3.2 Helical Shape Memory Alloy Actuators

Shape memory alloys have great potential in actuator applications due to their high strength-to-weight ratio and work output associated with the phase transformation. Conventional systems such as hydraulic or pneumatic actuators transmit high power in large scale actuators, but their performance is significantly reduced as they scale down in size. This limitation is addressed by using SMA actuators in the form of helical springs. Helical actuators provide larger stroke when compared to other forms such as wire, beams or strips (e.g., Ref. [18]). Other thermal actuators have been used in the past such as wax or bimetal actuators, but these methods are affected by several limitations such as slow response time or geometrical constraints [43]. The use of SMA helical actuators eliminates these limitations and provides greater advantages over other alternatives. Motion in SMA actuators is generated by conversion of thermal energy (heat addition or removal) to mechanical energy (stroke) due to the temperature-induced solid-state phase transformation described in the preceding sections.

Throughout this study, the initial undeformed length, L_o , of the spring exists in the high temperature austenite phase. In this phase, the spring constant is at its maximum value due to the high shear modulus, (e.g., 20 GPa). Applying a pre-load, P , introduces an initial extension, $\delta_{initial}$, which takes the spring to a new pre-deformed length. As the material undergoes a temperature induced phase transformation to the R-phase, the spring stiffness reduces due to reduction in the shear modulus, (e.g., 8 GPa), and exhibits a final deflection, $\delta_{working}$, to a maximum length, L_m , as shown in Fig. 3.1.

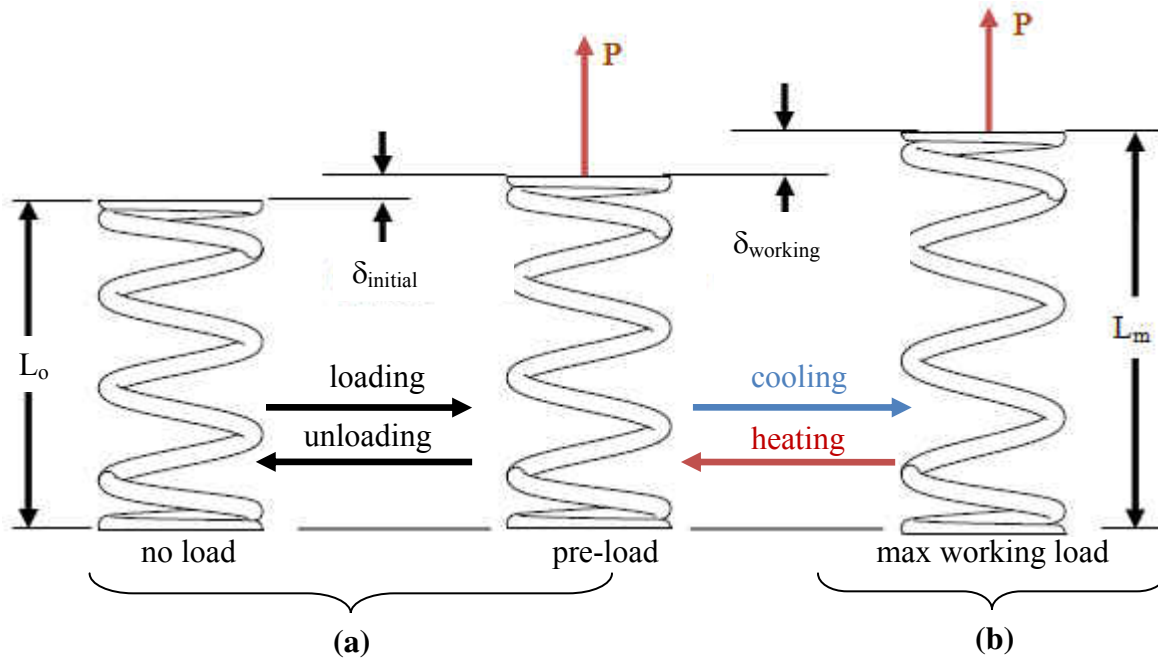


Figure 3.1: SMA helical spring length: (a) high temperature phase (b) low temperature phase

3.3 Helical Shape Memory Alloy Actuator Design

A circular cross-section helical spring subjected to uniaxial loading was examined in this study as shown in Fig. 3.2 with the adopted global and local orthogonal coordinate systems (O, X, Y, Z) and (o, t, n, b), respectively. The cross-section of the spring with wire diameter, d , mean coil diameter, D , and helix angle, α , subject to a compressive or tensile load, F , experiences shear force, F_s , and a moment couple, $FD/2$, that contributes to bending effects as the coil curvature changes and to twisting effects from the resulting torque (Fig. 3.3a-b) [44]. The single headed arrow represents the uniaxial force in the indicated direction and the double headed arrow represents moment about the indicated direction.

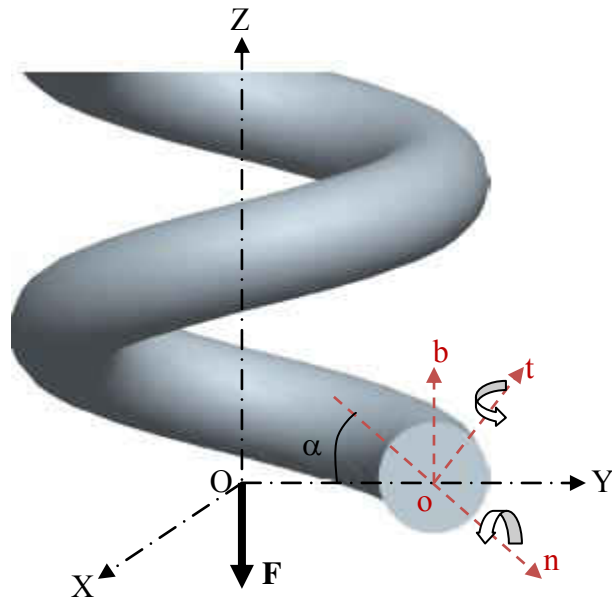


Figure 3.2: Global and local reference coordinate systems for the spring

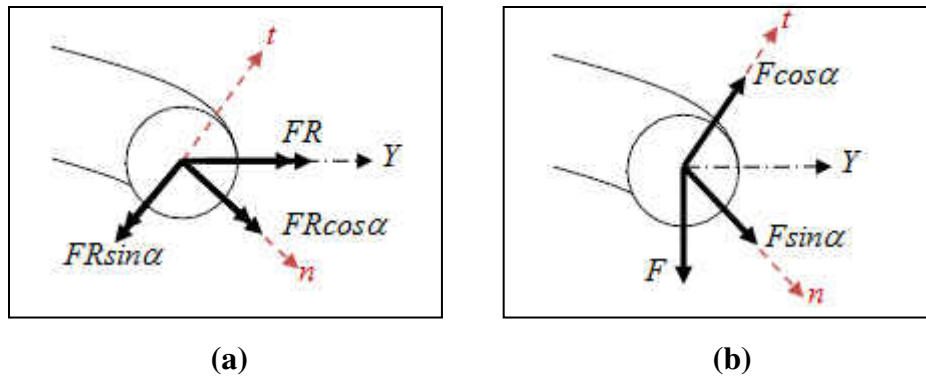


Figure 3.3: Free body diagram (a) resultant moment (b) resultant force

The resultant force and moment vectors acting on the helix cross-section can be decomposed into six forces and moments expressed in the local coordinate system as

$$\bar{\mathbf{R}} = \{N \ F_n \ F_b \ M_t \ M_n \ M_b\} \Rightarrow \bar{\mathbf{R}} = \begin{bmatrix} (F \sin \alpha) + \left(F \frac{D}{2} \cos \alpha\right) \\ (F \cos \alpha) + \left(F \frac{D}{2} \sin \alpha\right) \\ \int_S \sigma_{tb} dA + \int_S -y \sigma_t dA \end{bmatrix} \begin{Bmatrix} \bar{e}_t \\ \bar{e}_n \\ \bar{e}_b \end{Bmatrix} \quad (3.1)$$

where \bar{e}_t , \bar{e}_n , and \bar{e}_b are the unit vectors in the local coordinate system, N is the axial load in the spring axis direction, F_b is the normal shear force, M_t is the torsional moment, and M_b is the normal bending moment. Note that the effect of the binomial force and moment components are small and can be neglected [45]. The position of any point on the helix in the undeformed and deformed configurations can be determined if the initial position is known. The parametric equations for a helix in general are given by

$$X = \frac{D}{2} \cos \theta \quad Y = \frac{D}{2} \sin \theta \quad Z = \frac{p}{2\pi} \theta \quad (3.2)$$

where θ and p are the polar angle and helix pitch, respectively. The location of any undeformed point along the neutral axis of the helix in the global coordinate system is then given as

$$\mathbf{X} = \frac{D}{2} \cos \theta \mathbf{I} + \frac{D}{2} \sin \theta \mathbf{J} + \frac{p}{2\pi} \theta \mathbf{K} \quad (3.3)$$

Taking derivatives of the above equation yields expressions for position in the local coordinate system. The displacement vector is given by the difference between the deformed and undeformed positions as shown below:

$$\delta(T, \sigma) = \begin{Bmatrix} \delta_x \\ \delta_y \\ \delta_z \end{Bmatrix} = \begin{Bmatrix} x(X, t) - X \\ y(Y, t) - Y \\ z(Z, t) - Z \end{Bmatrix} \quad (3.4)$$

3.3.1 Equations in Reduced Form

The commonly used SMA spring design methodology for actuator applications is based on a reduced form of general elastic theory. This approach neglects curvature and direct shear effects by assuming the spring elements as a straight wire in pure torsion. From the simple theory of torsion [46], every section subjected to a torque experiences a state of pure shear. The uncorrected stress neglecting direct shear loading and wire curvature may be obtained from

$$\frac{T_a}{J} = \frac{\tau}{R} = \frac{G\theta}{L} \quad (3.5a)$$

where T_a is the applied torque, J is the polar second moment of area of coil cross-section, G is the shear modulus, R is the outside radius, and θ is the angle of twist on a length L . Solving for the shear stress from Eq. 3.5a yields

$$\tau = \frac{8FD}{\pi d^3} \quad (3.5b)$$

where F is the applied load, D is the mean diameter, and d is the wire diameter. However, Eq. 3.5b gives an average stress on the outside edge of the coil. In order to determine the maximum stresses which occur on the inside of the spring, the latter equation is modified using a correction factor of the form

$$\tau_{\max} = \kappa \frac{8FD}{\pi d^3}, \quad \kappa = \begin{cases} \kappa = 1 \rightarrow \text{pure torsion} \\ \kappa_s = 1 + \frac{0.5}{C} \rightarrow \text{shear stress correction factor} \\ \kappa_w = \frac{4C-1}{4C-4} + \frac{0.615}{C} \rightarrow \text{Wahl's factor (Ref. [45])} \end{cases} \quad (3.5c)$$

where C is the spring index ($C=D/d$), and κ is the stress factor that takes on three values depending on the stress state due to torsional shear, direct shear, curvature stress concentration, or some combination. In the derivation of Eq. 3.5c, the shear and bending moments were neglected, and the small helix angle was considered to be zero.

Extension of the helical spring can be obtained from the principle of total strain energy. Neglecting shear effects, the total strain energy must equal the total work done given by

$$U_e = W \Rightarrow \frac{T_c^2 L}{2G(T, \sigma)J} + \frac{M^2 L}{2E(T, \sigma)I} = \frac{1}{2} F \delta(T, \sigma) \quad (3.6a)$$

where T_c and M are the moment components in the local coordinate system, $G(T, \sigma)$ is the shear modulus, $E(T, \sigma)$ is the elastic modulus (both dependent on the temperature, T , and stress, σ), and I is the second moment of area. Rearranging and solving for the extension, Eq. 3.6a becomes

$$\delta(T, \sigma) = \frac{1}{4} \pi N_a D^3 F \sec \alpha \left[\frac{\cos^2 \alpha}{G(T, \sigma)J} + \frac{\sin^2 \alpha}{E(T, \sigma)I} \right] \quad (3.6b)$$

where N_a is the number of active coils and α is the helix angle. Rearranging the above equation and using torsion theory [44], an expression for the variable spring constant $k(T, \sigma)$ is found to be

$$k(T, \sigma) = \frac{4 \left[\frac{\cos^2 \alpha}{G(T, \sigma)J} + \frac{\sin^2 \alpha}{E(T, \sigma)I} \right]^{-1}}{\pi N_a D^3 \sec \alpha} \quad (3.7a)$$

Equations 3.6b and 3.7a are valid for both close-coiled and open-coiled helical springs subjected to uniaxial loading. In the case of small helix angles, (i.e., $\alpha \leq \pi/15$), the spring is considered close-coiled in which case the bending and shear stresses can be neglected leaving a

predominantly torsional stress state. Assuming small helix angles (i.e., $\cos \alpha = 1$ and $\sin \alpha = 0$), Eqs. 3.6b and 3.7a reduce to conventional equations for close-coiled helical springs.

For small α ,

$$\alpha \approx 0 \rightarrow \cos^2 \alpha \approx 1 \text{ and } \sin^2 \alpha \approx 0$$

$$\delta(T, \sigma) = \frac{1}{4} \pi N_a D^3 F \frac{1}{1} \left[\frac{1}{G(T, \sigma) J} + \frac{0}{E(T, \sigma) I} \right]$$

$$\delta(T, \sigma) = \frac{1}{4} \pi N_a D^3 F \left[\frac{1}{G(T, \sigma) \frac{\pi d^4}{32}} \right]$$

$$\delta(T, \sigma) = \frac{8 N_a D^3 F}{G(T, \sigma) d^4} \quad (3.7b)$$

Similarly,

$$k(T, \sigma) = \frac{G(T, \sigma) d^4}{8 N_a D^3} \quad (3.7c)$$

The shear modulus can be quantified using shape memory alloy models that take into account the degree of martensitic transformation [47].

For helical SMA springs, these equations are applied to the high and low temperature phases as the shear modulus changes with temperature or stress. As mentioned previously, this approach neglects the effect of direct shear and bending stress as the load is applied. In the following section, the full theory is examined and compared with the discussion in this section.

3.3.2 Equations in Full Form

Exact methods have been developed for helical springs under uniaxial loads. The following approach applies to uniform cross-section wires where each section of the coil exhibits the same resultant forces and moments [38]. This boundary value problem approach due to Ancker and Goodier does not consider the third and higher order terms of the series. Adapting from Ref. [38], the maximum stresses on the inside of a coil in tension are given in cylindrical coordinates as

$$\tau_{r\theta} = \tau_{rz} = \sigma_r = 0 \quad (3.8a)$$

$$\tau_{\theta z} = \frac{8FD}{\pi d^3} \left(1 + \frac{5}{4C} + \frac{7}{8C^2} + \dots \right) \quad (3.8b)$$

$$\sigma_{\theta} = \frac{8FD}{\pi d^3} \left(\frac{(-2 + \nu + 4\nu^2)}{4(1 + \nu)C} \tan \alpha + \dots \right) \quad (3.8c)$$

$$\sigma_z = \frac{8FD}{\pi d^3} \left(2 \tan \alpha + \frac{(11 + 12\nu)}{4(1 + \nu)C} \tan \alpha + \dots \right) \quad (3.8d)$$

Equations 3.8a-d were combined to determine the maximum shear and normal stresses on the inside of the coil

$$\tau_{\max} = \sqrt{\tau_{\theta z}^2 + \frac{1}{4}\sigma_{\theta}^2} = \frac{8FD}{\pi d^3} \left(1 + \frac{5}{4C} + \frac{7}{8C^2} + \frac{\tan^2 \alpha}{2} + \dots \right) \quad (3.9a)$$

$$\sigma_{\max} = \frac{8FD}{\pi d^3} \left(1 + \frac{5}{4C} + \frac{7}{8C^2} + \frac{3 \tan^2 \alpha}{2} + \frac{(9 + 13\nu + 4\nu^2)}{8(1 + \nu)C} \tan \alpha + \dots \right) \quad (3.9b)$$

Assuming small changes in coil diameter during extension, Ancker and Goodier developed an expression for the spring extension based on elastic theory.

$$\delta = \frac{8PD^3N_a}{Gd^4} \left(1 - \frac{3}{16C^2} + \frac{(3+\nu)}{2(1+\nu)} \tan^2 \alpha + \dots \right) \quad (3.10)$$

These equations yield small errors when small helix angles are used. In the case of large extensions, modified equations are used and can be found in Ref. [45].

3.3.3 Finite Element Method

The finite element method (FEM) was used to compare the two approaches used for helical spring design. Since the resultant moments, forces and the stress distributions are equal at any given section, only half turn of the helical spring are shown. The model was discretized using 4312 solid elements (Brick 20 node 186) using ANSYS[®] and ANSYS Workbench[®]. Figure 3.4 shows the finite element mesh used. Boundary conditions were applied to obtain the stress as the spring extends. Elastic deformation was solely considered. One end of the coil was fully constrained against translation and rotation to simulate the operating conditions of the SMA actuators used in the thermal switch. An axial load along the spring axis was applied along the other end. The material properties and dimensional parameters used in the study are listed in Tables 3.1 and 3.2 respectively. The macroscopic shear and Young's moduli for both phases were determined from experimental data obtained from this work assuming linear isotropic behavior. However, it is important to note that NiTiFe alloy exhibits anisotropic behavior and nonlinearity due to detwinning during the martensitic phase transformation that was not considered here. Also, these mechanical properties were taken to be constant in each phase and not vary with stress or temperature. Poisson's ratios used are those of a NiTi alloy [48].

Table 3.1: Mechanical properties of NiTiFe used in the analytical and FEM models

Spring	Austenite	R-Phase
Young's Modulus (GPa)	53	21
Poisson Ratio	0.33 Ref. [46]	0.31
Shear Modulus (GPa)	20	8

Table 3.2: NiTiFe Spring dimensions used in the analytical and FEM models

Wire diameter	Coil diameter	Number of active coils
2.159 mm	15.24 mm	9

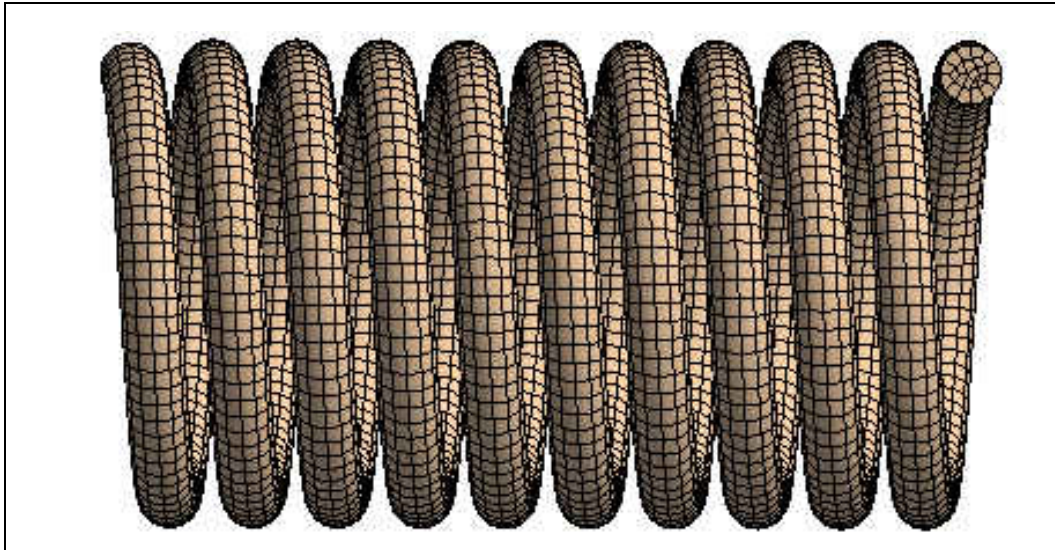


Figure 3.4: Finite element mesh used to model spring

3.3.4 Comparisons between Elastic Theory and the Finite Element Method

The maximum shear stresses, $\tau_{\theta z}$, for a small helix angle, $\alpha \approx 2^\circ$, were calculated using Eqs. 3.5b, 3.5c, 3.8b, and compared with results from a finite element model. This analysis showed that the shear stresses are maximum at the inner radius of the coil, which is not captured by Eq. 3.5b which assumes pure torsion. Equation 3.5c derived by Wahl provides both the torsional shear and bending shear on the neutral axis of a cantilever beam with circular cross-section. Equation 3.8b takes into account the maximum shear stresses that occur at the inner radius of the spring. Figure 3.6 shows the $\tau_{\theta z}$ shear stress distribution in a cross-section of a spring coil from FEM. The boundary conditions and constraints were imposed to simulate a uniaxial spring in tension for different applied loads with its ends fixed against rotation. It is shown that the maximum shear occurs at the inner radius of the spring for all loads considered. This was also verified using different helix angles of $\alpha = 5, 10, 15$ and 20 degrees.

The shear stress distributions across any coil cross-section are compared with the predictions from theory in Fig. 3.5. A combination of the torsional shear stress, direct shear stress and stress concentration due to curvature are sketched in Fig. 3.5b. The maximum shear stress occurs at the inner most fiber of the cross-section as shown in Fig. 3.5a obtained by FEA.

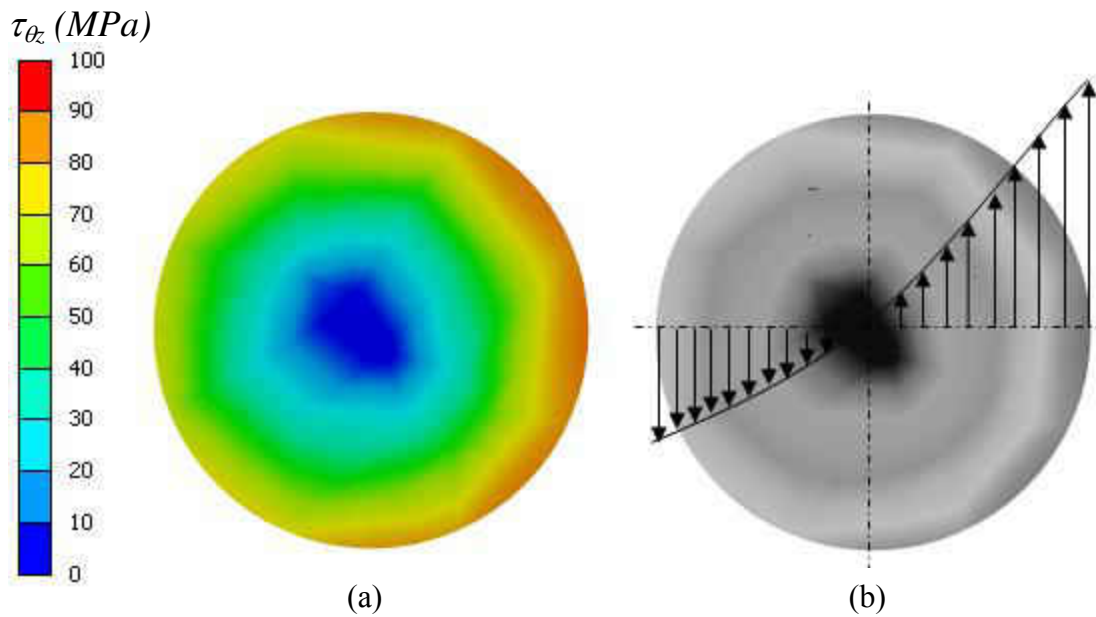


Figure 3.5: Shear stress distribution across coil section in a helical SMA spring: (a) FEA (b) prediction from theory (spring axis to the right)

Figure 3.6 presents the shear stress distribution, $\tau_{\theta z}$, on the wire's cross-section for a helical spring in tension. Comparisons of the theoretical $\tau_{\theta z}$ shear stress values with the finite element analysis (FEA) are shown in Fig. 3.7. FEA results are within 1% and 2% error from the values obtained using Equations 3.5c and 3.8b respectively. However Equation 3.5b, which assumes pure torsion in the coil, differs by 18 % from the FEA results.

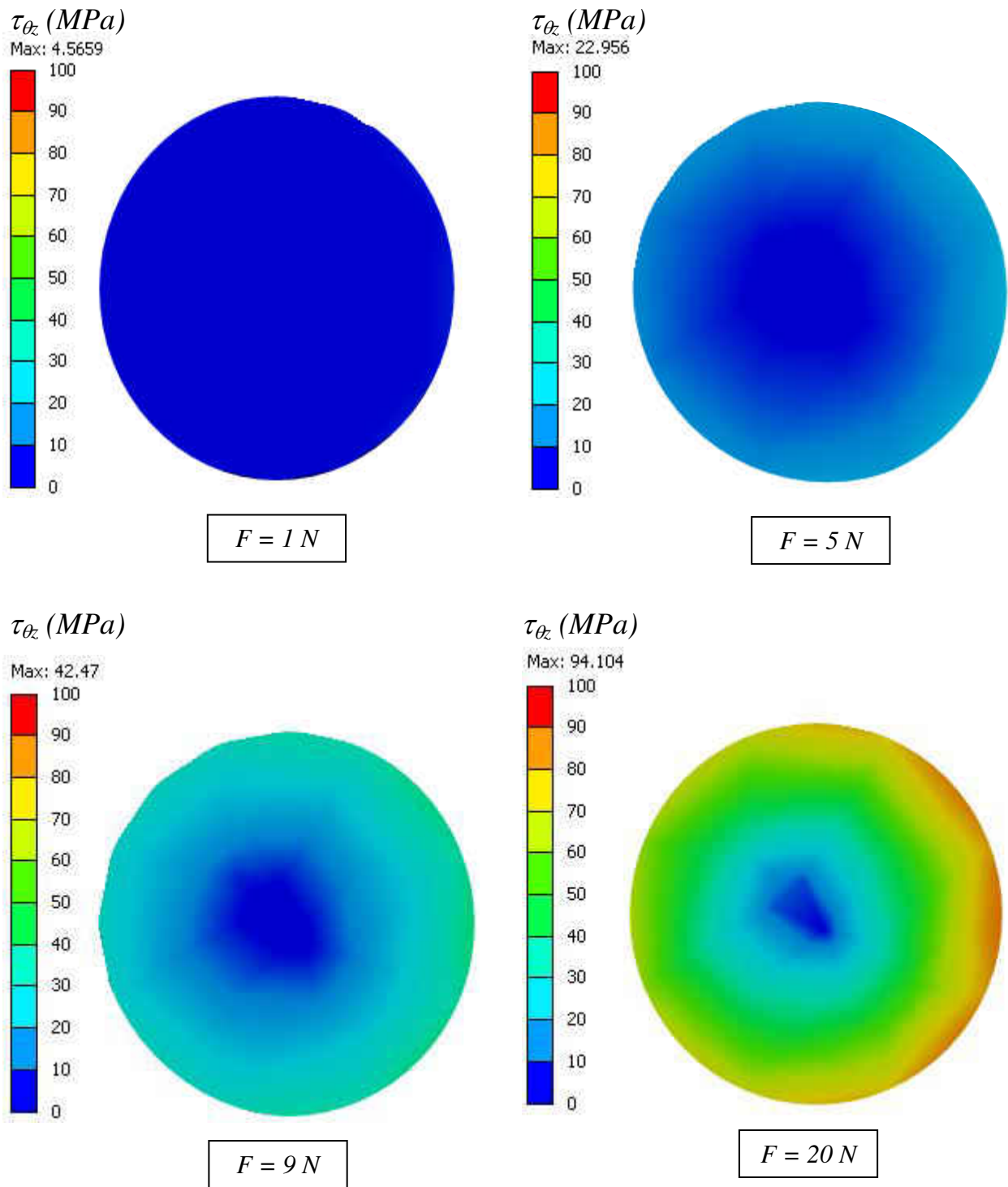


Figure 3.6: $\tau_{\theta z}$ shear stress distribution for a spring cross-section with small helix angle $\alpha \approx 2^\circ$ (austenite, spring axis to the right)

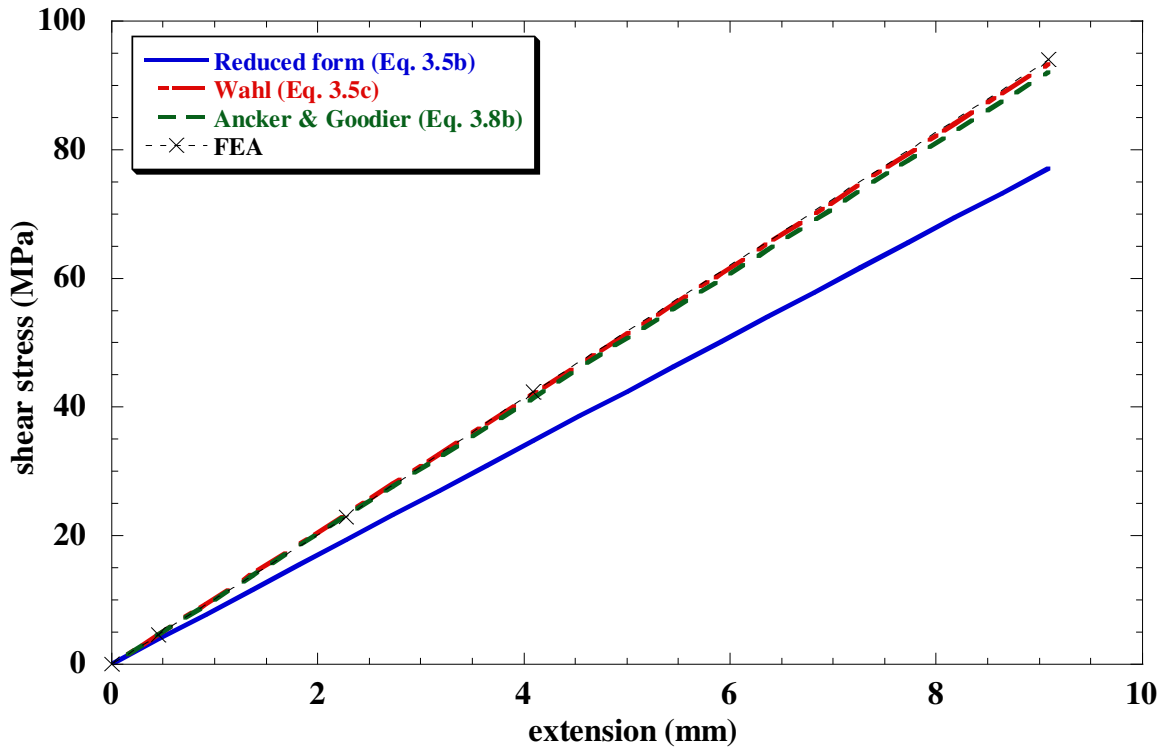


Figure 3.7: Comparison of maximum shear stress (τ_{0z}) using elastic theory and FEA (austenite)

To show that the helix angle has an effect on the stress distribution along the coil, the normal stresses along the spring axis, σ_z , were investigated using FEA and Eq. 3.8d. Figure 3.8 shows the normal stress distribution for different helix angles in the austenite phase using a load of $F = 9\text{ N}$. Similar to the shear stress (τ_{0z}), the maximum normal stresses occur at the inner radius of the coil. Figure 3.9 shows the results obtained using both Eq. 3.8d and FEA for various helix angles.

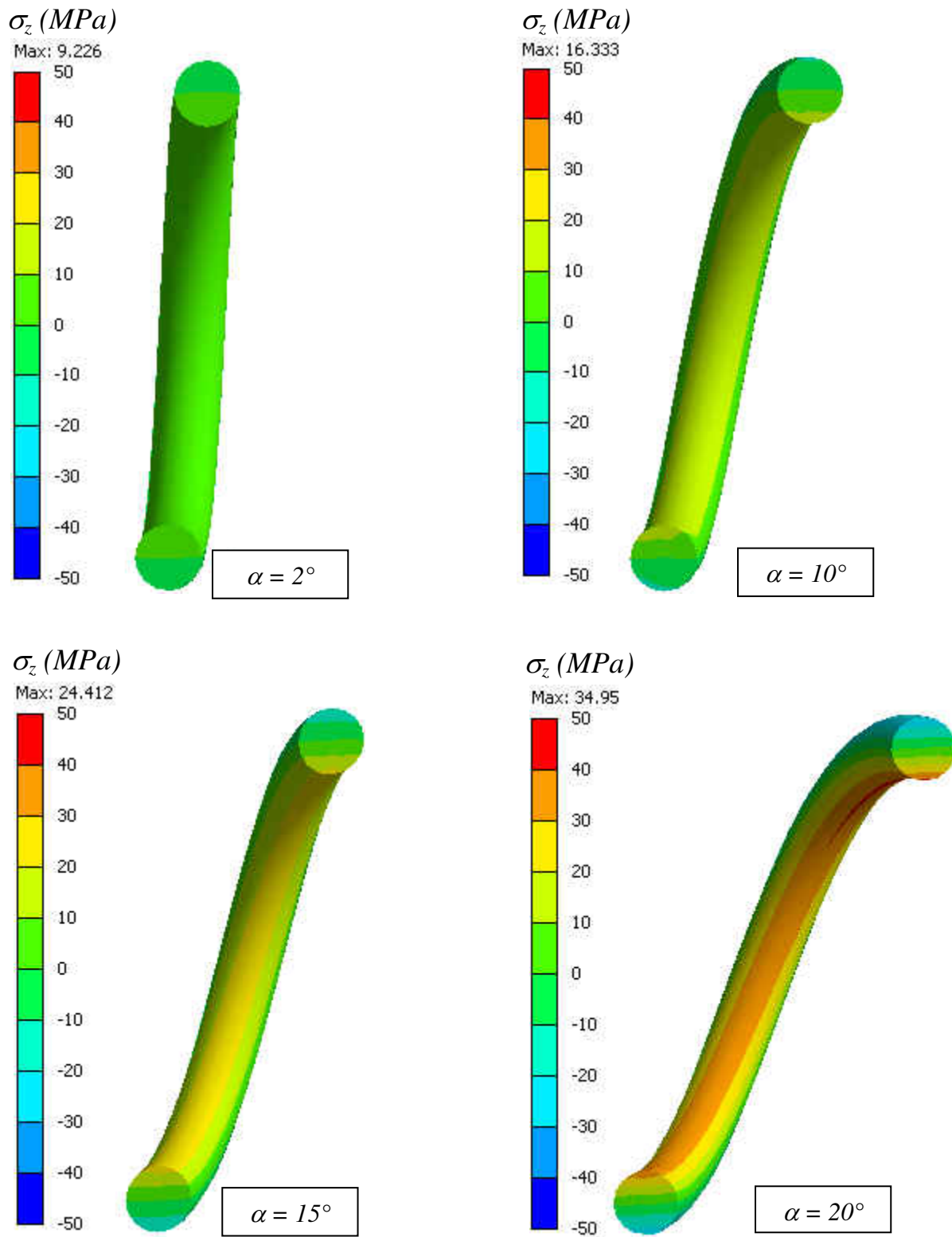


Figure 3.8: σ_z distribution for $F=9$ N in helical coil (austenite)

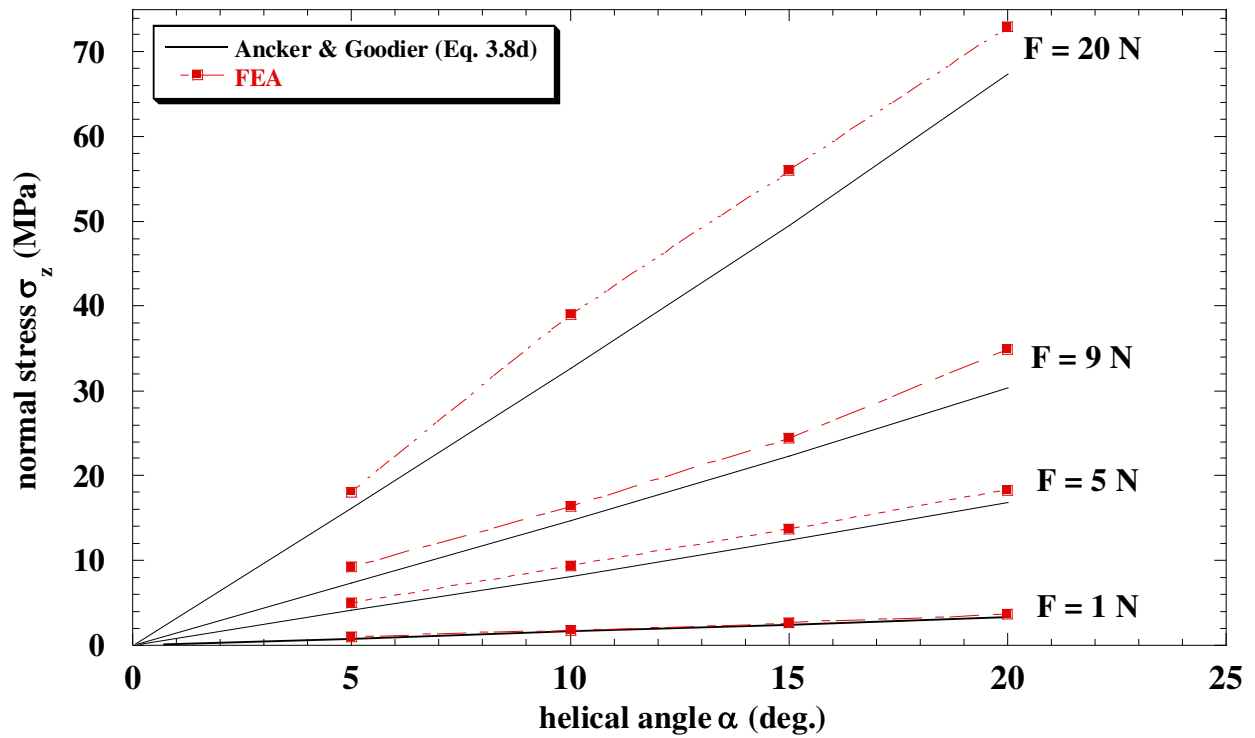


Figure 3.9: σ_z as a function of helical angle for various loads (austenite)

The spring constant is obtained from the slope of the load-extension response of the elastic region during loading. Spring extensions along the coil axis were investigated using the theoretical approaches described in the earlier sections and FEA for various loads and helix angles. Analyses were carried out in both phases as shown for one case in Figure 3.10.

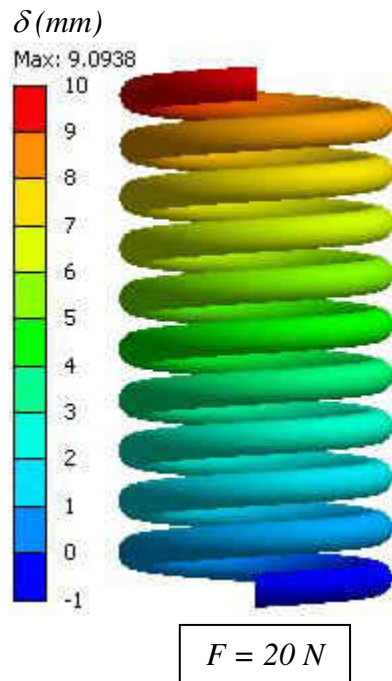
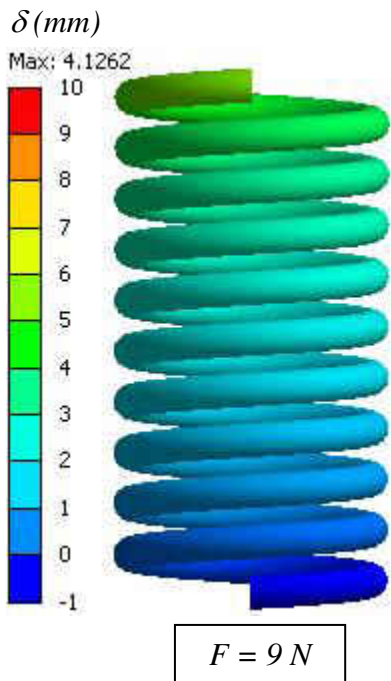
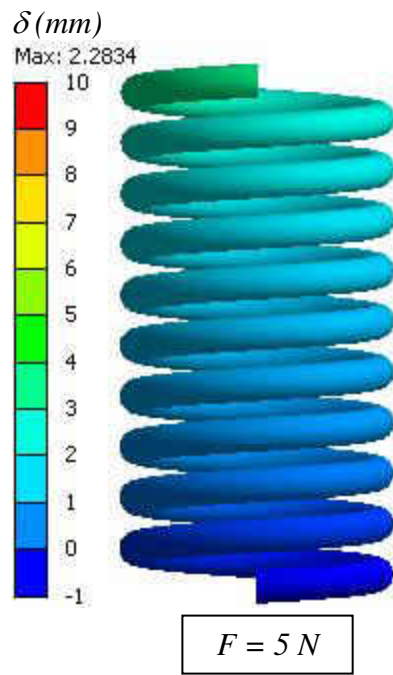
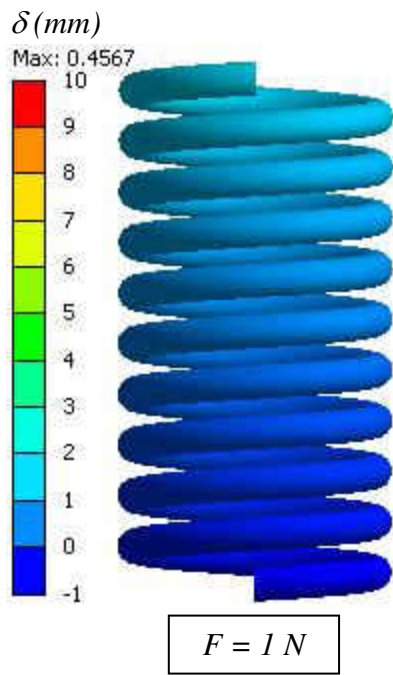


Figure 3.10: Spring displacement in tension for small helix angle $\alpha \approx 2^\circ$ (austenite, bottom of spring fixed and load applied at the top end)

Spring extensions as a function of the helical angle are shown for the austenite phase in Fig. 3.11 and for the R-phase in Fig. 3.12. For small helix angles and small loads, the equations give similar results for both phases. However, upon increasing the helical angle and the load, the results diverge due to large extension. Therefore, for springs that are not close-coiled, the simplified approaches do not capture the true deformation of the spring and the complete theory has to be used for accurate results.

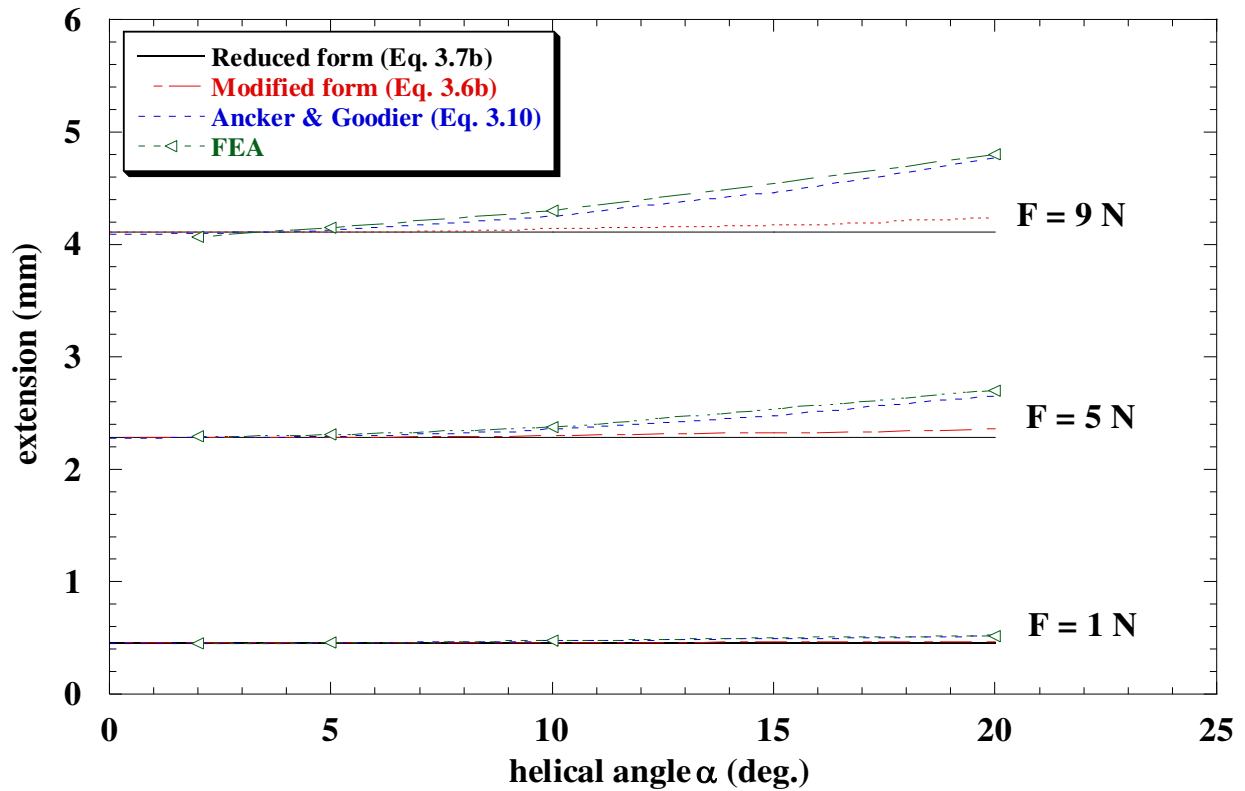


Figure 3.11: Correlation between spring extension and helical angle (austenite)

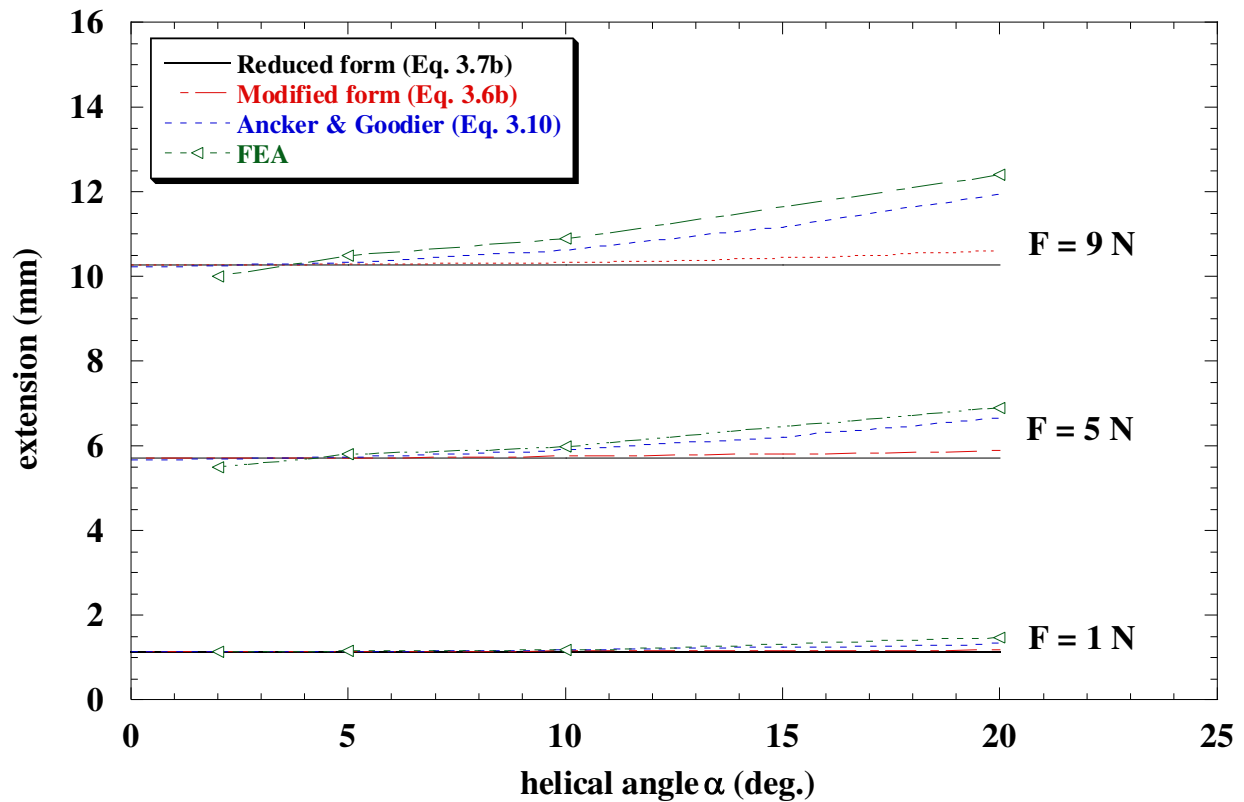


Figure 3.12: Correlation between spring extension and helical angle (R-phase)

The comparisons between FEM and theory (both in reduced and full forms) presented in this section highlight the limitations of the theory. It was shown from FEA that maximum stresses occurred at the inner radius of the springs which in turn were predicted by the equations from elastic theory in full form and not by the ones in reduced or simplified form. Furthermore, it was established that the spring extension is influenced by the helical angle and which should be considered especially in the design of open-coiled springs.

3.4 Fabrication of Actuators

The SMA helical actuators were fabricated at the UCF machine shop. The as drawn NiTiFe SMA wire was coiled at room temperature around a solid mandrel machined with a helical channel along its length corresponding to the wire diameter, mean diameter, pitch and number of coils (Fig. 3.13). Three mandrels were made for three different spring geometries by machining solid brass cylinders and helical channels. For example, for the first spring, a 25.4 mm diameter solid brass cylinder was reduced down to 15.24 mm corresponding to the outside diameter of the spring. A 2.159 mm deep channel (2.5 turns/inch) was cut through the length of the cylinder. At the tip of the mandrel, a small hole was drilled to insert the wire (bent at 90°) and initiate the wire winding process. Once the mandrels were ready, they were individually clamped in a lathe chuck spinning at low speeds to facilitate the spring winding process. As the wire was being coiled, a brass sleeve with an inner diameter equal to the outer spring diameter was pushed in to keep the wire from springing back.

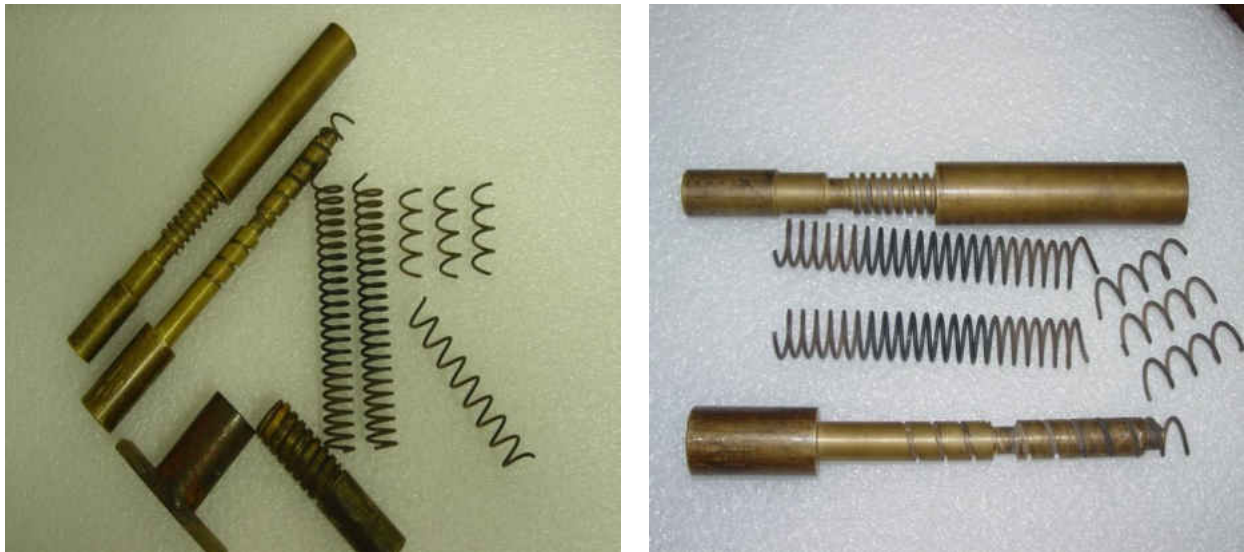


Figure 3.13: Helical shape memory alloy actuators and spring winding mandrels

The fixture containing the coiled wire was placed in a furnace for shape setting (Fig. 3.14). This was accomplished by heating at 500 °C for 25 minutes in air in a muffle furnace, followed by an ice-water quench. The helical springs were then removed from the fixture and subjected to a final Electrical Discharge Machining (EDM) operation to ground the ends in order to facilitate their fastening in the switch (Fig. 3.15). For each geometry, a total of four SMA springs were made following the same heat treatment conditions. The resulting spring geometries are shown in Table 3.3.



Figure 3.14: Mandrel containing coiled SMA wire in the furnace

The initial coils of spring geometry 3 had a tighter winding (square ends) in order to facilitate electrical discharge machining of the ends so as to create a flat contact surface to better accept/transfer load, better alignment (to avoid buckling), and most importantly, to make greater

surface contact (approx. $\sim 290^\circ$) for improved heat conduction during operation. Given this modification, spring geometry 3 was used in the subsequent work reported here even though some initial results from the other geometries are presented for completeness.

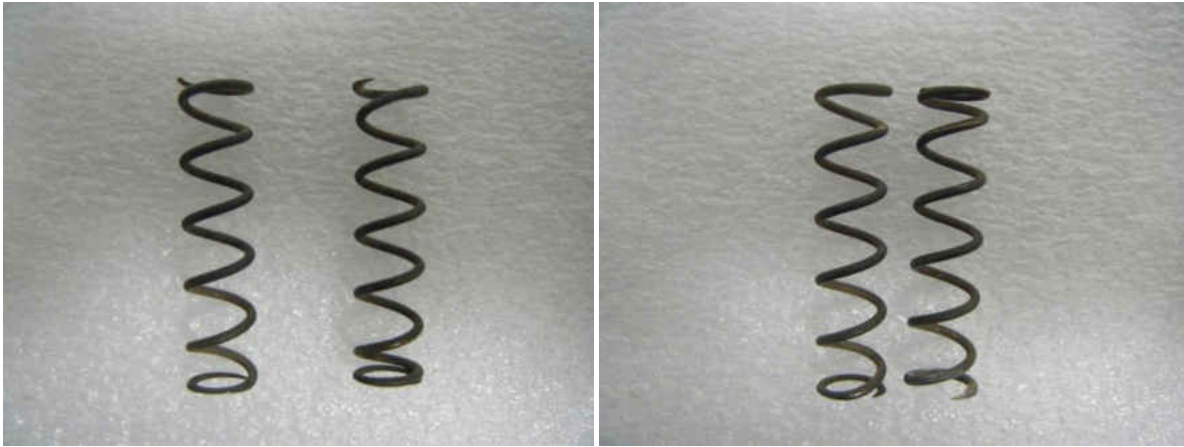


Figure 3.15: Spring geometry 3 after shape setting and final electrical discharge machining to increase contact

Table 3.3: Shape memory alloy spring geometries (wire diameter 2.159 mm)

Spring	D (mm)	Pitch (mm)	Free length (mm)	End condition
1	17.8	10.9	63.5	Plain
2	12.7	15.9	50.8	Ground
3	13.1	12.7	63.5	Cut

Table 3.4: Shape memory alloy spring constants (wire diameter 2.159 mm)

Spring	Spring constant N/mm	
	Austenite	R-Phase
1	1.878	0.482
2	8.587	2.209
3	4.283	1.517

Prior to installing the springs in the thermal switch, mechanical testing was conducted on a servo-hydraulic load frame to determine the spring constants in the austenitic state at room temperature. The SMA springs were placed on flat grips in order to apply a gradual load in compression. Load-displacement data was collected for each spring using a 220 N load cell and a LVDT attached to the load frame upper grip. Results corresponding to the four springs with spring geometry 3 are plotted in Fig. 3.16.

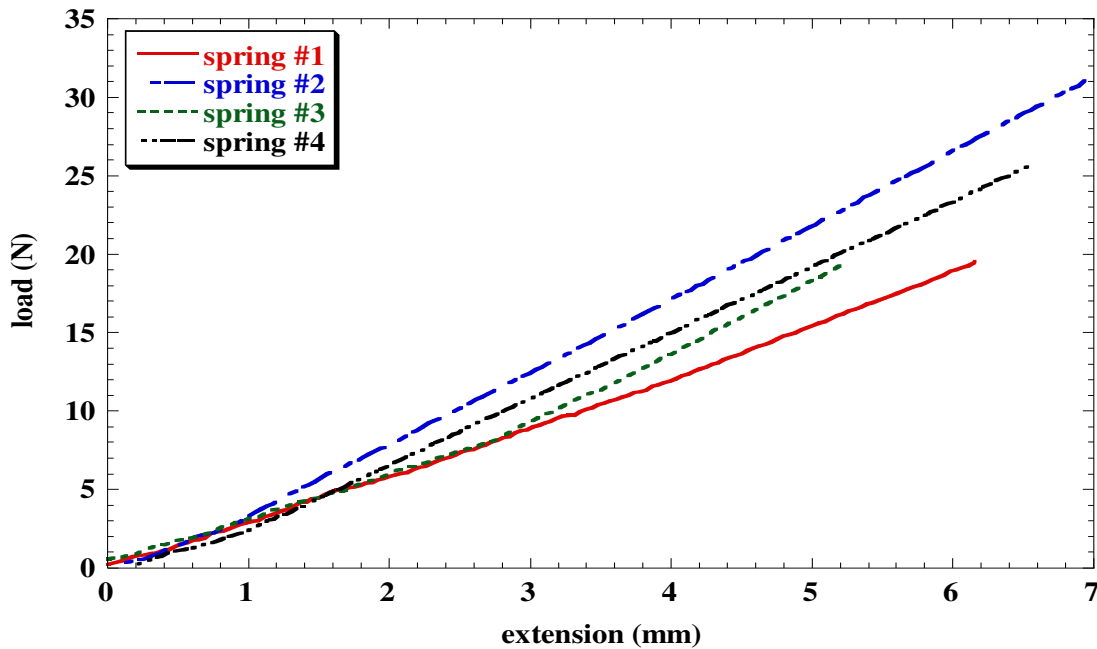


Figure 3.16: Load-extension response of the SMA springs at room temperature

The slopes of the load-extension lines represent the spring constants under loads not exceeding the elastic limit of the alloys and are reported in Table 3.4. The average spring constant of the four springs with spring geometry 3 was 4.283 N/mm and this corresponds to a shear modulus of 19.4 GPa for austenite from Equation 3.7a compared to the initial value of 21 GPa.

Sets of stainless steel bias springs (four each) were designed and custom made to provide the necessary force to extend the switch during the SMA phase transformation. The calculations are presented in Appendix A. The geometry of the bias springs was selected with an inside diameter large enough to fit over the SMA springs and avoid contact during extension. They were made longer than the SMA springs in order to provide a bias force during the open and closed positions of the switch. The bias spring constants were selected to be between that of the austenite and R-phase SMA spring constants to provide force balance during actuation. Multiple bias springs (sets of four), were obtained in order to modify the switch extension as needed.

3.5 Thermal Switch Actuation

Actuation of the thermal switch occurs through a combination of the SMA springs and the compression stainless steel bias springs connected in parallel between the switch base and a moving plate (Fig. 3.17-18). The actuation is characterized as a push-pull mechanism activated by a change in temperature. The SMA actuators were designed to hold (pull) the switch in the open or “off” position in the high temperature phase (e.g., day cycle on the lunar surface). Initially at room temperature, the bias springs are compressed by the SMA spring force to keep the switch open. In this state, the force of the SMA springs in the austenite phase is greater than the total bias force (with contributions from the weight of the components, internal heat pipe pressure and the unextended bias springs). As the temperature drops below the transformation temperature, the SMA springs transform to their more compliant phase as the compressed bias springs overcome the SMA stiffness and extend. At this instance, the total bias force pushes the moving plate causing the switch to close. Conversely, during the reverse transformation, the

SMA springs transform back to their stiffer phase and pull the switch to the open or “off” position by compressing the bias springs.

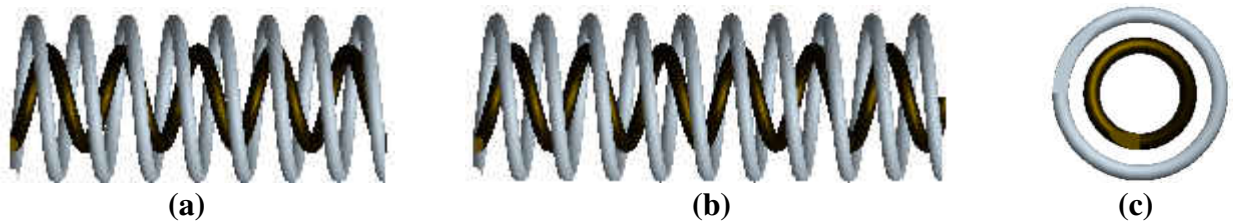


Figure 3.17: Arrangement of the shape memory (dark shading) and bias springs (light shading): (a) at high temperature with the SMA spring pre-loaded and the bias spring compressed in the open or “off” position; and (b) at low temperature with the SMA spring extended and the bias spring in the closed or “on” position (c) Sectional view of the shape memory and bias springs

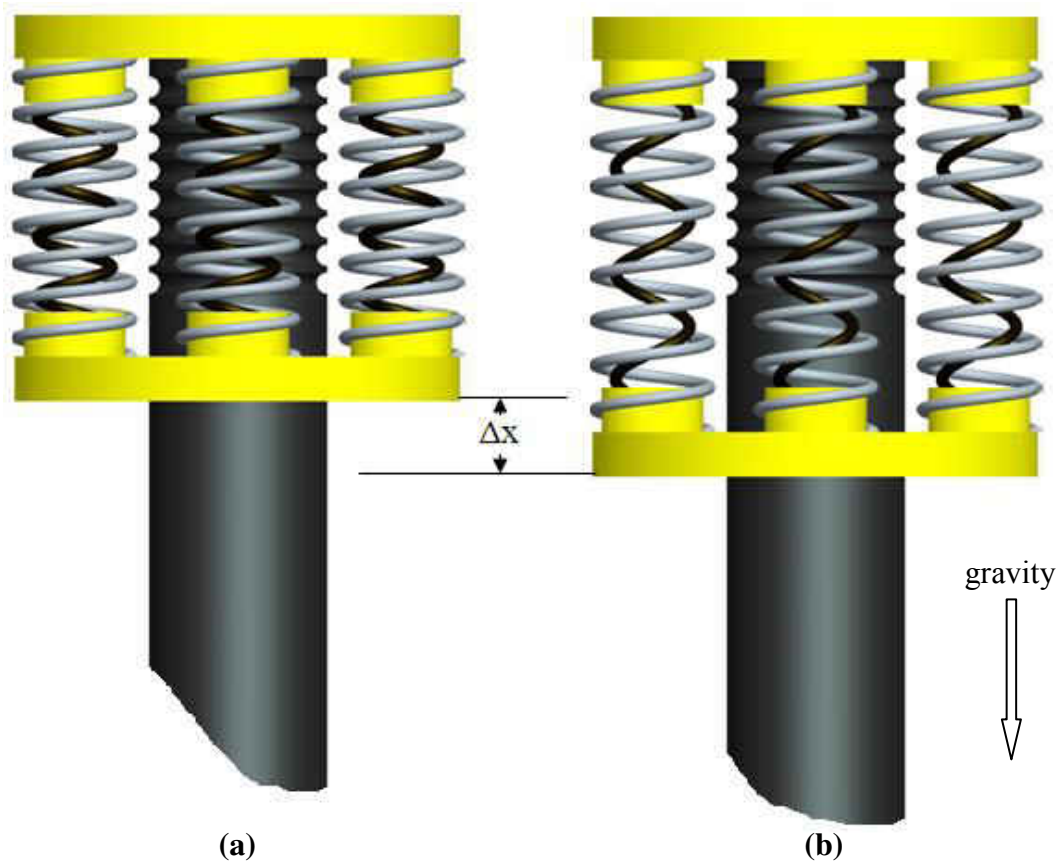


Figure 3.18: Arrangement of the shape memory (dark shading) and bias springs (light shading) in the switch: (a) at high temperature with the SMA spring pre-loaded and the bias spring compressed in the open or “off” position; and (b) at low temperature with the SMA spring extended and the bias spring in the closed or “on” position

CHAPTER FOUR: VARIABLE LENGTH TWO-PHASE HEAT PIPE

4.1 Overview

A heat pipe incorporates heat transfer mechanisms that provide considerable advantages over other heat transfer devices due to larger heat transport even with very small temperature gradients. Heat pipes based on two-phase systems offer greater thermal capacity during working fluid phase changes with smaller mass flow rates [49]. The first engineering application was investigated and designed in the early nineteenth century by A.M. Perkins. This early age thermosyphon was used in a steam boiler to transfer heat from a furnace [50, 51]. The name “heat pipe” was first introduced by Grover in the 1960s when he was studying phase changes in a heat transport device [52]. Since then, heat pipes have been employed in various applications in the aerospace, electric power, chemical and HVAC industries. Design terminology and operating conditions of closed form heat pipes (thermosyphons) have been outlined by many researchers and various theories have been developed for the mechanism of heat and mass transfer involving two-phase flow [53-58]. For example, Wang et al. [59] used computational fluid dynamics (CFD) to study two-phase flow and phase changes involving porous media. Tabatabai and Faghri investigated the two-phase flow characteristics and transition boundaries in micro tubes [60]. Wang and Vafai evaluated the transient thermal performance of heat pipes [61].

Heat pipes can be considered to be composed of three main sections: an evaporator (heat source) section, an adiabatic section and a condenser (heat sink) section (Fig. 4.1). As the working fluid liquid pool at the evaporator end heats up, bubbles form and move upward as they grow in size and get rejected from the liquid pool by buoyancy forces. The working fluid

transforms to vapor due to heat addition, and absorbs an amount of heat equivalent to the latent heat of vaporization. As the vapor moves upward toward the condenser at lower temperature, the working fluid vapor condenses and flows back to the evaporator region in the form of a film or droplets assisted by gravity in the case of a thermosyphon. Finally, the liquid reaches the bottom of the heat pipe, mixes with the liquid pool and evaporates again allowing a heat gain/release mechanism inside the heat pipe. The heat pipe used in this work is a gravity-assisted heat pipe where the condensate streams downward assisted by gravitational forces and no capillary system is used. Due to this gravity-driven requirement, the condenser region has to be above the evaporator region for proper operation.

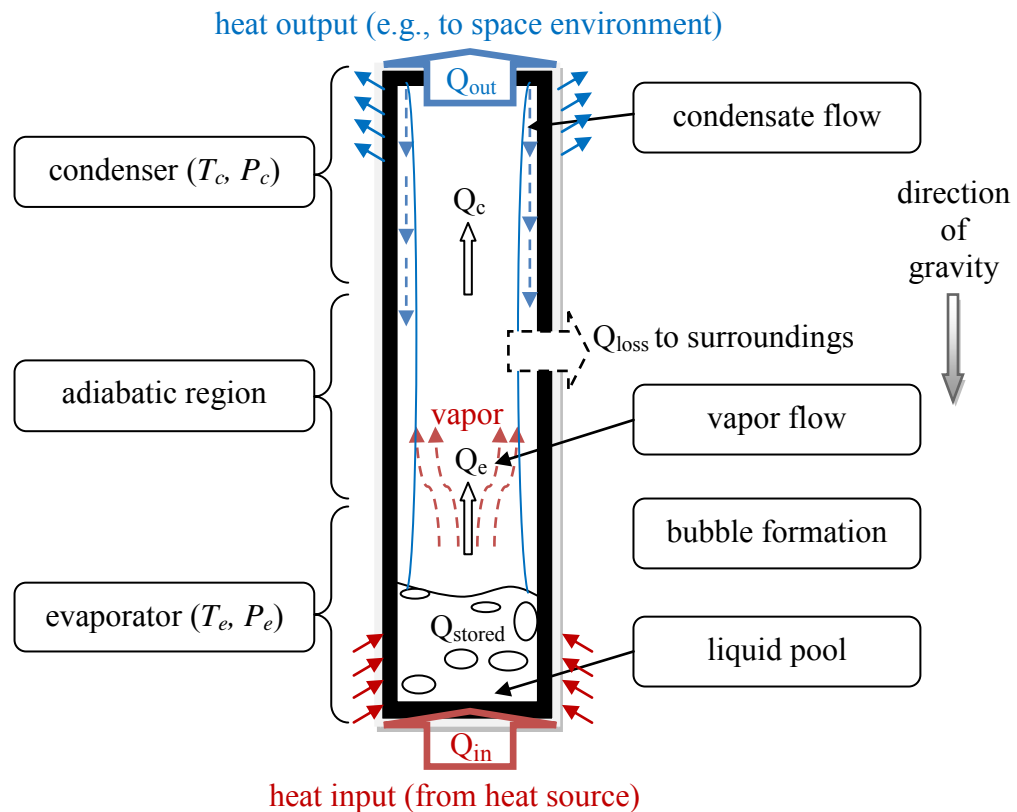


Figure 4.1: Sections in a heat pipe involving two-phase flow

In general, the energy balance for a defined control volume can be expressed as

$$E_{in} = E_{stored} + E_{generated} + E_{out} \quad (4.1)$$

Assuming the heat leaving the evaporator with uniform heat addition is equal to the heat entering the condenser with uniform temperature distribution, energy balance in a heat pipe gives

$$Q_{in} = Q_{stored} + Q_{loss} + Q_{out} \quad (4.2)$$

The heat discharged, Q_e , and heat received, Q_c , can be expressed as

$$Q_e = h_e A_e (T_{s,e} - T_{e,sat}) \quad (4.3a)$$

$$Q_c = h_c A_c (T_{c,sat} - T_{s,c}) \quad (4.3b)$$

where h is the heat transfer coefficient, A is the internal surface area, T is the wall temperature, T_{sat} is the saturation temperature, and 'e', 'c' and 's' stand for the evaporator, condenser and surface respectively. The surface temperature of both regions is taken as the average temperature of the entire region.

Given the constraints associated with the operation of the switch in this work, the heat pipe has to be entirely sealed and at the same time allow movements enforced by the SMA actuators. The heat pipe used here accomplishes heat transfer through boiling, evaporation and condensation of the selected working fluid. The analyses presented are based on theoretical models of pool boiling and parametric effects, evaporation, and laminar film condensation on a vertical wall [62-64]. Various parameters such as operating temperature and pressure, working

fluid volume, end boundary conditions, and transport limitations are considered to ensure maximum performance.

4.2 Closed Two-Phase Thermosyphon Design

The underlying theory of a closed two-phase thermosyphon (CTPT) is based on bubble formation and liquid evaporation as the lower end of the pipe is heated. The vapor travels upward transporting heat towards the condenser that is at a lower temperature, causing the vapor to condense and thereby releasing the latent heat. At that point, the fluid returns back to the lower end in the form of droplets or a film assisted by gravitational effects. During this process, heat is transported via the latent heat of vaporization of the working fluid, operating in a thermodynamic saturated state, and rejected during condensation. Several assumptions have been made to quantify the heat rate at both ends of the device starting with assuming constant fluid properties at the evaporator and condenser sides. Uniform heat input at the low end, negligible interfacial shear stresses of the vapor and liquid film, low film velocity (negligible momentum and energy change), and finally laminar condenser film flow were also assumed.

4.2.1 Heat Transfer at the Evaporator

Heat transfer at the evaporator was determined using pool boiling theory [65-70]. Farber and Scoriah characterized the pool boiling process using the heat transfer coefficient in Newton's law of cooling over a range of temperature differences (Fig. 4.2). During the heating process, bubbles form at nucleation sites and move up due to buoyancy forces to the liquid-vapor

interface. Depending on the temperature difference, various forms of boiling can occur starting with interface evaporation, nucleate boiling, film boiling and finally radiation as show in Fig. 4.2.

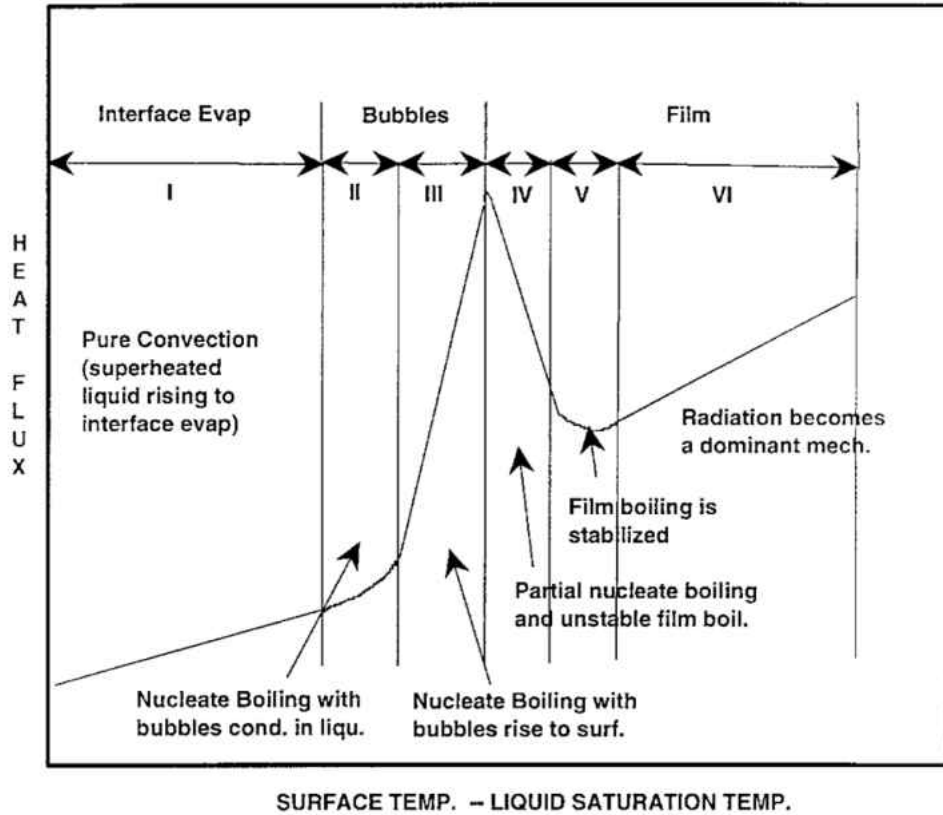


Figure 4.2: Critical regions in a pool boiling curve [70]

The average heat transfer coefficient for nucleate boiling in a two-phase closed thermosyphon was obtained empirically [62] as:

$$\bar{h}_e = 0.32 \left(\frac{\rho_l^{0.65} k_l^{0.3} c_{p,l}^{0.7} g^{0.2}}{\rho_v^{0.25} h_{fg}^{0.4} \mu_l^{0.1}} \right) \left(\frac{P_e}{P_a} \right)^{0.23} q_e''^{0.4} \quad (4.4a)$$

where ρ is density, k is thermal conductivity, c_p is specific heat at constant pressure, g is gravitational acceleration, h_{fg} is latent heat of vaporization, μ is dynamic viscosity, P_e and P_a are

evaporator and atmospheric pressure, q'' is the incident heat flux, and l and v stand for liquid and vapor respectively.

Another model based on nucleate pool boiling in the working fluid pool was reported by Rohsenow [68] as

$$\bar{h}_e = \left(\frac{q}{h_{fg}} \right)^{2/3} \left(\frac{\mu_l}{\sqrt{\frac{\sigma}{g(\rho_l - \rho_v)}}} \right)^{1/3} \frac{c_{p,l}}{C_{sf}} \frac{1}{Pr_l^{1.7}} \quad (4.4b)$$

where σ is the surface tension, C_{sf} is the solid-fluid constant, taken to be 0.0154 for polished pentane-copper combination [71], and Pr is the Prandtl number. Finally the experimental heat transfer coefficient was obtained using

$$\bar{h}_e = \frac{Q_{avg-measured}}{\pi D_p L_e (T_{avg} - T_e)} \quad (4.4c)$$

where D_p is the pipe inner diameter, L_e is the evaporator length, and $Q_{avg-measured}$ is the heat throughput obtained experimentally. For design purposes, the theoretical heat transfer rate at the evaporator was quantified using Equation 4.4a and rearranged to give

$$Q_e = \left[0.32 \left(\frac{\rho_l^{0.65} k_l^{0.3} c_{p,l}^{0.7} g^{0.2}}{\rho_v^{0.25} h_{fg}^{0.4} \mu_l^{0.1}} \right) \left(\frac{P_e}{P_a} \right)^{0.23} A_e^{0.6} (T_e - T_{sat}) \right]^{5/3} \quad (4.5)$$

Equation 4.5 was later compared with the experimental results. Detailed calculations are presented in Appendix A.

4.2.2 Heat Transfer at the Condenser

Assuming no heat losses across the CTPT, the heat rate at the condenser must be equal to the heat rate at the evaporator assuming small fin effect (Appendix A) and small radiation from the surface. Using Nusselt and Rohsenow's film condensation approach [72-75], the heat transfer coefficient at the condenser was determined to be

$$\bar{h}_c = 0.943 \left[\frac{g \rho_l (\rho_l - \rho_v) k_l^3 \sin(\theta) h'_{fg}}{\mu_l L_c (T_{sat} - T_c)} \right]^{1/4} \quad (4.6)$$

where θ is the inclination angle from the vertical, L_c is condenser length and h'_{fg} is the modified latent heat given as

$$\begin{aligned} h'_{fg} &= h_{fg} (1 + 0.68Ja) \\ Ja &= \frac{c_{p,l}(T_c - T_{sat})}{h_{fg}} \\ \therefore h'_{fg} &= h_{fg} + 0.68c_{p,l}(T_{sat} - T_c) \end{aligned}$$

where Ja is Jakob number. In this design, the heat pipe is placed vertically making a 90° angle with the horizontal reference. In another approach given by Faghri et al. [55, 76], the condenser heat transfer coefficient was obtained in terms of the Reynolds and Nusselt numbers. Starting with the Reynolds number (in the adiabatic section) expressed in this context by

$$\text{Re}_l = \frac{w\delta}{\nu_l} = \frac{Q}{\pi D \mu_l(T_c) h_{fg}(T_c)} \quad (4.7)$$

where w is the velocity, δ is the liquid film thickness and ν_l is the kinematic viscosity of the liquid and using the modified Nusselt number correlation, the average heat transfer coefficient can be rewritten in terms of the average Nusselt number as

$$\bar{h}_c = \bar{Nu} \cdot k_l(T_c) \left(\frac{v_l^2}{g} \left(\frac{\rho_l(T_c)}{\rho_l(T_c) - \rho_v(T_c)} \right) \right)^{-1/3} \quad (4.8)$$

Equation 4.8 is valid for a range of Nusselt numbers given by:

$$\bar{Nu} = 0.925 \text{Re}_l^{-1/3} \quad \text{for} (\text{Re}_l < 325) \quad (4.9a)$$

Other correlations for film condensation based on experimental data were given by Gross [54]

$$\bar{Nu} = \left[\left(0.925 (1 - 0.63(p^*)^{3.3})^{-1} \text{Re}_l^{-1/3} \right)^2 + \left(0.044 \text{Pr}_l^{2/5} \text{Re}_l^{1/6} \right)^2 \right]^{1/2} \quad (4.9b)$$

where p^* is the pressure ratio of the thermosyphon to the working fluid pressure, and by Uehara et al. [77]

$$\bar{Nu} = 0.884 \text{Re}_l^{-1/4} \left(0.5 < \text{Re}_l < 325 \text{Pr}_l^{-0.96} \right) \quad \text{For laminar range} \quad (4.9c)$$

$$\bar{Nu} = 0.044 \text{Pr}_l^{2/5} \text{Re}_l^{1/6} \left(\text{Re}_l > 325 \text{Pr}_l^{-0.96} \right) \quad \text{For turbulent range} \quad (4.9d)$$

In this current design, the heat pipe is placed vertically making a 90° angle with the horizontal reference. Substituting Equation 4.6 into Equation 4.3b, the theoretical condenser heat rate can be reworked as

$$Q_c = 0.943 \left[\frac{g \rho_l (\rho_l - \rho_v) k_l^3 \sin(\theta) h'_{fg}}{\mu_l L_c} \right]^{1/4} A_c (T_{sat} - T_c)^{3/4} \quad (4.10)$$

with liquid properties evaluated at the film temperature, and the vapor density and latent heat at the saturation temperature [78, 79]. Detailed calculations are presented in Appendix A.

4.2.3 Limitations of Two-Phase Thermosyphons

While closed two-phase thermosyphons (CTPTs) have worked efficiently over many years, nevertheless, a number of restrictions are associated with the operation of these devices that determine the maximum attainable heat transfer. Various parameters of a CTPT and the working fluid have to be carefully selected to avoid resistance against heat transport or even elimination of the operative mechanisms. Common limitations and the methods adopted to overcome them are described in this section.

- The *viscous limit* or *vapor pressure limit* is a constraint that influences the heat transfer capacity when the vapor pressure at the colder side of the heat pipe approaches zero. The saturation vapor pressure at the evaporator equalizes the pressure drop required to move the vapor to the condenser region resulting in very low or no mass flow from the evaporator section. This limitation occurs mainly when the CTPT is operating below the normal operating range of the working fluid [76]. In this current design, this restriction was eliminated by choosing the appropriate working fluids (pentane and R-134a).
- The *sonic limit* occurs when the vapor flow velocity reaches sonic rates due to low vapor pressure. This limit can take place at start up and during normal operation resulting in poor function [76]. However, designing a small CTPT eliminates this limitation.
- The *entrainment limit* is one of the most critical operation restrictions because it not only affects the heat transfer rate, but also can cause complete burn out or destruction of the heat pipe. Entrainment occurs when the drag force of the vapor fluid exceeds the surface tension of the returning condensate which causes entrapment of liquid fluid with vapor. This occurrence limits the amount of fluid that returns to the liquid pool in order to keep the heat

pipe cycle going and may result in dry out at the evaporator region [80]. The choice of working fluid and its surface tension are critical in avoiding this problem.

- Finally, the *boiling limit* and *condenser limit* depend on the boundary conditions and the geometry of the ends of the CTPT [81]. The cooling rate of the condenser predicts the maximum heat rate that can be conducted. Similarly, the input heat flux needs to be determined correctly and accounted for in the design so that the fluid will not boil completely.
- For Proper heat pipe operation with maximum heat transfer rate, the contact surface between the heat source and the evaporator end has to be clean at all times and free of dust to reduce or eliminate contact resistance.

4.3 Heat Pipe Fabrication and Assembly

A wickless, gravity-assisted, closed two-phase thermosyphon (CTPT) was fabricated with the goal of providing on demand heat transfer via a three stage process consisting of heat acquisition, transport, and rejection in this order. The key issues associated with the design of the CTPT are geometry, working fluid, and end boundary conditions. The CTPT geometry incorporates cylindrical containment, an evaporator (heat source) section, and a condenser (heat sink) section rigidly attached to form a sealed chamber. Oxygen-free high conductivity (OFHC) copper was selected to construct the evaporator and condenser due to high thermal conductivity, while the containment pipe was made of stainless steel to avoid corrosion and handle high internal pressures. The lower end geometry was constructed as a flat surface with cylindrical walls to promote uniform heating and bubble formation; and the upper end was formed with a

spherical shape to increase surface area and guide the liquid film condensate to flow back along the smooth containment pipe wall. To enable expansion and contraction of the CTPT, extensible bellows made by welding 316L SS flanges and a AM350 core were connected closer to the upper end allowing strokes up to 4 mm from the neutral position. A schrader valve is used to allow for the evacuation and charging of the working fluid. A schematic and picture of the assembled CTPT with its various regions are shown in Fig. 4.3.

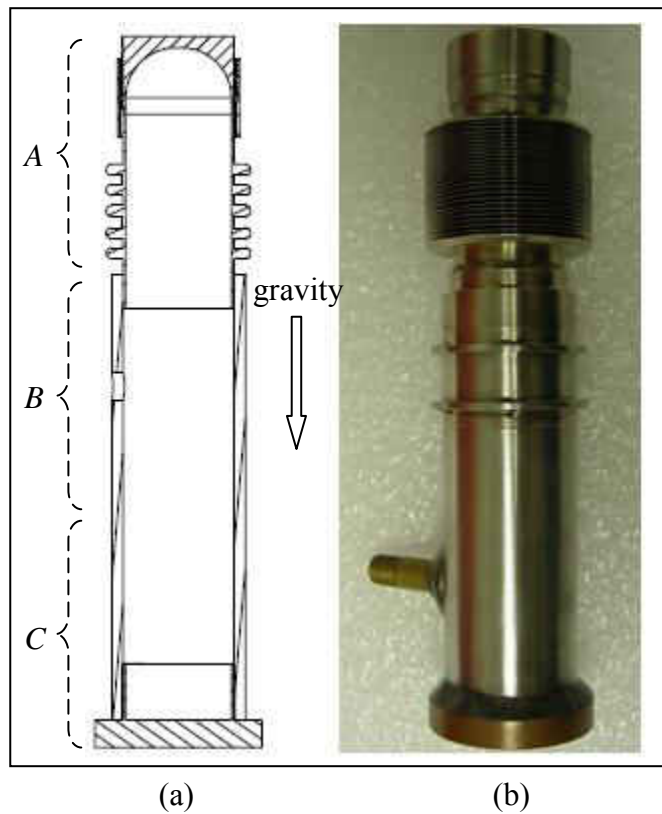


Figure 4.3: Assembly of the closed two-phase thermosyphon: (a) schematic with the regions *A*, *B*, and *C* being the condensation, adiabatic, and evaporation regions, respectively (b) final assembly

The final heat pipe geometry such as the evaporator and condenser lengths was optimized by iteration starting with small length values and increasing them until the heat transfer was

maximized. This method was done using the heat transfer equations for both ends of the heat pipe.

4.4 Thermophysical Properties of the Working Fluids

The working fluids were appropriately selected for the operation temperature and pressure, and to avoid corrosion or gas generation due to chemical reaction with the pipe materials. Pentane and R-134a were the working fluids selected. These working fluids were selected based on the actuators operation temperature; however, for lunar and Mars applications, other working fluids should be used to meet cryogenic requirements such as argon, hydrogen or helium among other cryogens. The saturation thermophysical properties of pentane and R-134a are shown in Tables 4.1-4 (Adopted from National Institute of Standards and Technologies (NIST) thermophysical properties of fluid systems database).

Table 4.1: Thermophysical saturation properties for pentane (liquid phase)

Temperature (C)	Pressure (MPa)	Density (l, kg/m ³)	Enthalpy (l, kJ/kg)	Cp (l, J/g*K)	Viscosity (l, Pa*s) (*10 ⁴)	Therm. Cond. (l, W/m*K) (*10 ¹)	Surf. Tension (l, N/m) (*10 ²)
-100	9.8012E-06	735.19	-289.28	1.9777	12.504	1.6407	2.9642
-80	1.0043 E-04	717.29	-249.53	1.999	7.8523	1.5551	2.7327
-60	6.2586 E-04	699.48	-209.24	2.0327	5.5339	1.4669	2.5022
-40	2.7187 E-03	681.58	-168.14	2.0792	4.1915	1.3791	2.2732
-20	9.0283 E-03	663.44	-125.98	2.1384	3.3262	1.2935	2.0463
0	2.4448 E-02	644.87	-82.497	2.2099	2.7221	1.2111	1.822
20	5.6558 E-02	625.7	-37.459	2.2929	2.2732	1.1325	1.6009

Table 4.2: Thermophysical saturation properties for pentane (vapor phase)

Temperature (°C)	Pressure (MPa)	Density (v, kg/m ³)	Enthalpy (v, kJ/kg)	Cp (v, J/g*K)	Viscosity (v, Pa*s) (*10 ⁶)	Therm. Cond. (v, W/m*K) (*10 ³)
-100	9.8012E-06	4.9117E-04	166.38	1.2073	3.94	5.494
-80	1.0043 E-04	4.5131 E-03	191.18	1.2745	4.39	6.5724
-60	6.2586 E-04	2.5505 E-02	217.25	1.3416	4.86	7.7416
-40	2.7187 E-03	1.0151 E-01	244.51	1.4133	5.33	9.0236
-20	9.0283 E-03	3.119 E-01	272.89	1.4923	5.81	10.44
0	2.4448 E-02	7.8942 E-01	302.31	1.5803	6.31	12.01
20	5.6558 E-02	1.7249	332.65	1.6782	6.79	13.753

Table 4.3: Thermophysical saturation properties for R-134a (liquid phase)

Temperature (°C)	Pressure (MPa)	Density (l, kg/m ³)	Enthalpy (l, kJ/kg)	Cp (l, J/g*K)	Viscosity (l, Pa*s) (*10 ⁴)	Therm. Cond. (l, W/m*K) (*10 ¹)	Surf. Tension (l, N/m) (*10 ²)
-100	5.5914E-04	1582.4	75.362	1.1842	18.824	1.4323	2.7503
-80	3.6719 E-03	1529	99.161	1.1981	10.203	1.3154	2.4101
-60	1.5906 E-02	1474.3	123.36	1.223	6.6051	1.2071	2.0796
-40	5.1209 E-02	1417.7	148.14	1.2546	4.6703	1.1059	1.7597
-20	1.3273 E-01	1358.3	173.64	1.293	3.4758	1.0107	1.4513
0	2.928 E-01	1294.8	200	1.341	2.6653	0.92013	1.156
20	5.7171 E-01	1225.3	227.47	1.4049	2.0737	0.83284	0.87555

Table 4.4: Thermophysical saturation properties for R-134a (vapor phase)

Temperature (°C)	Pressure (MPa)	Density (v, kg/m ³)	Enthalpy (v, kJ/kg)	Cp (v, J/g*K)	Viscosity (v, Pa*s) (*10 ⁶)	Therm. Cond. (v, W/m*K) (*10 ³)
-100	5.5914E-04	0.039694	336.85	0.59322	6.96	3.3445
-80	3.6719 E-03	0.23429	348.83	0.64165	7.75	4.9479
-60	1.5906 E-02	0.92676	361.31	0.69239	8.52	6.5554
-40	5.1209 E-02	2.7695	374	0.749	9.27	8.1736
-20	1.3273 E-01	6.7845	386.55	0.8158	10	9.8164
0	2.928 E-01	14.428	398.6	0.89723	10.7	11.514
20	5.7171 E-01	27.78	409.75	1.0007	11.5	13.335

CHAPTER FIVE: THERMAL SWITCH ASSEMBLY AND OPERATION

The shape memory helical actuators, bias springs, heat pipe, along with other components were integrated to assemble the thermal switch. Additional materials and components were selected and designed to improve the overall switch performance as presented in this chapter. The final assembly and principle of operation are described in this chapter.

5.1 Thermal Switch Components and Final Assembly

The SMA actuators were placed into cylindrical guides directly machined into a high conductivity copper base. These guides helped prevention of springs buckling when in compression, facilitated positioning during installation (by keeping symmetry and balance around the base), and provided better conductive heat transfer due to contact at the sides with the SMA springs. The bias springs were mounted outside the guides appropriately separated to avoid contact with the SMA springs. At the center of the base, the condenser apparatus, discussed in section 4.3, was machined directly into the base to eliminate thermal contact resistance and enhance conductivity. The exterior condenser surface was threaded to easily connect or disconnect the heat pipe. The ends of each spring were fastened to a Teflon plate with similar guides. During actuation, the springs push the moving plate that is connected to the heat pipe using two steel rings welded on the pipe. Finally, four steel rods connected to the base and the moving plate were used to maintain vertical and uniform displacement of the switch during actuation. The complete assembled sketch is shown in Fig. 5.1.

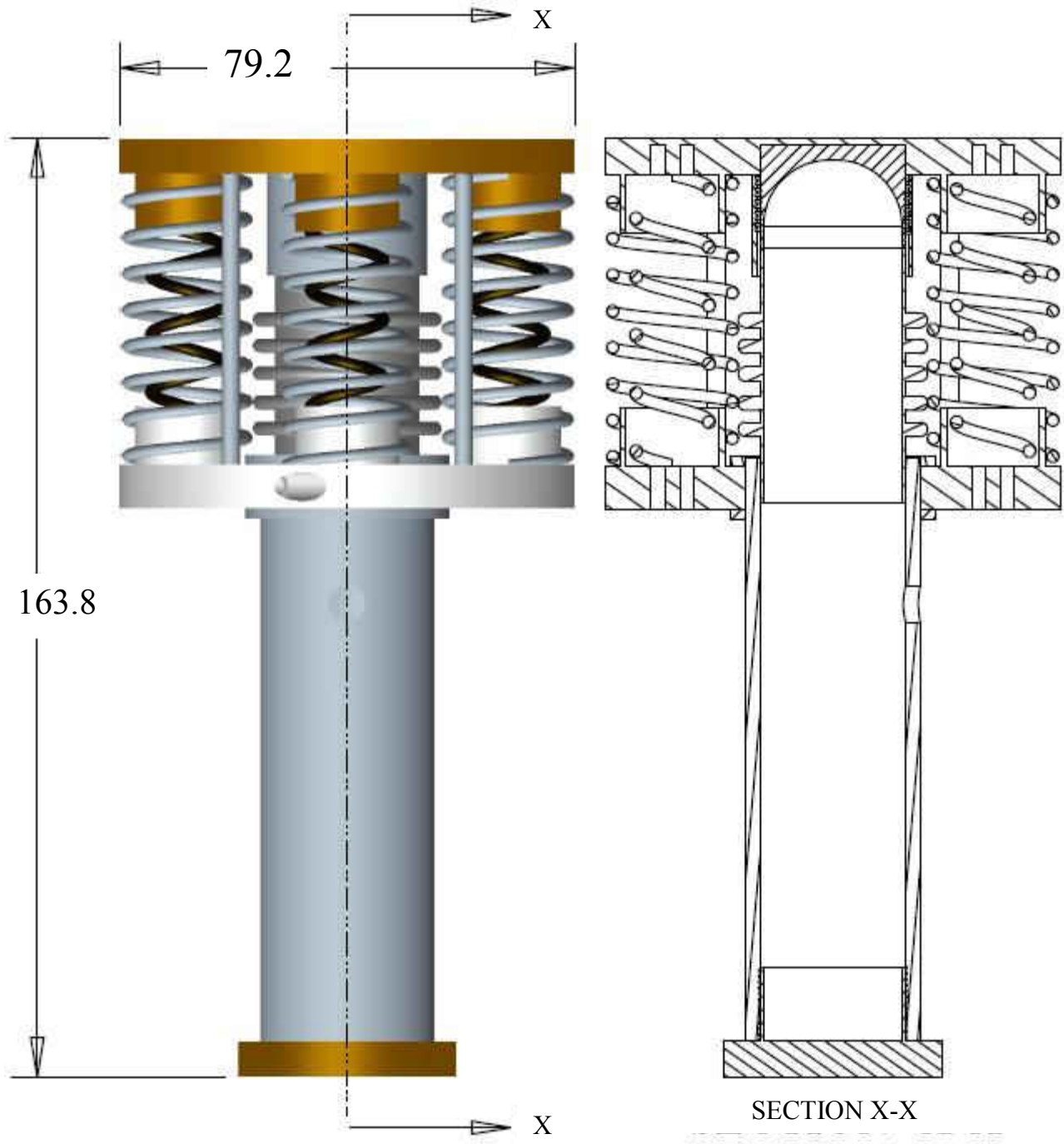


Figure 5.1: Schematic of final thermal switch assembly (dimensions in mm)

The final thermal switch assembly is shown in Fig. 5.2.

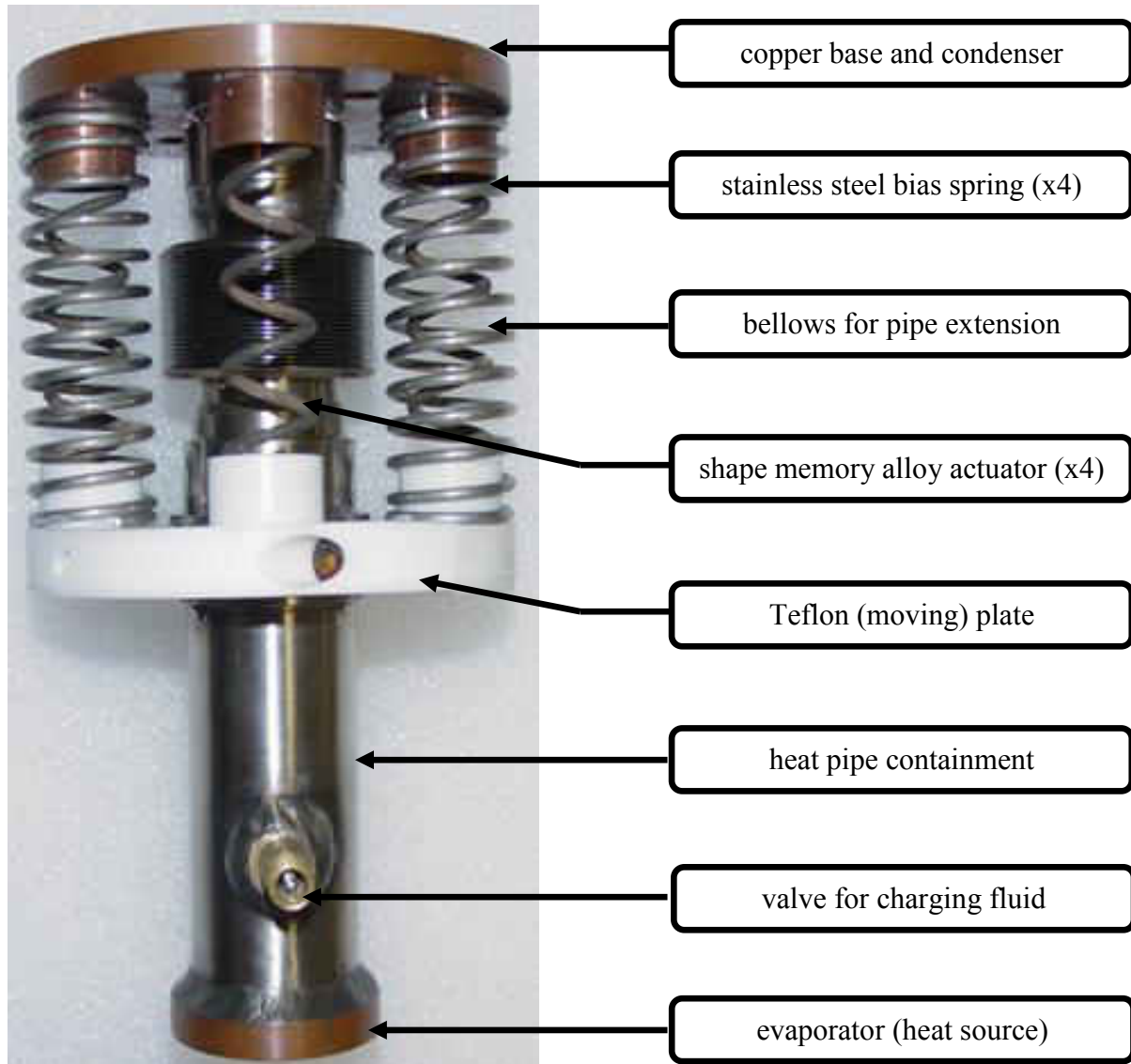


Figure 5.2: Final thermal switch assembly. The bias spring in the front was removed to show the position of the SMA spring.

5.2 Switch Operation

The objective of the thermal switch that was designed, fabricated and tested in this work was to provide on demand heat load rejection from a liquid oxygen (LOX) tank maintained at 92 K as the temperature of the space environment varies from 40 K to 400 K on the lunar surface. During a lunar day cycle (~14 days) when temperatures are near 400 K, the SMA springs are in their open or “off” position and exist in their high temperature phase where they overcome the force from the bias springs (Fig. 5.3a). In this state, the switch provides thermal isolation and no engagement occurs. During a lunar night cycle when temperatures are near 40 K, the temperature of the surrounding space environment drops resulting in a phase transformation in the SMA springs. The phase transformation results in the R-phase that is now less stiffer and is overcome by the bias springs. The resulting actuation (facilitated by bellows in the heat pipe) takes the switch to its closed or “on” position wherein it is in thermal contact with the LOX tank (Fig. 5.3b). In this closed position, heat is rejected via conduction through the walls of the heat pipe and by two-phase heat transfer involving the working fluid in the heat pipe. The working fluid transfers heat in a four step process that involves: (i) fluid pool boiling at the lower (evaporator) end due to heat addition; (ii) fluid bubble evaporation and travel; (iii) condensation of the vapor reaching the upper (condenser) end due to the temperature drop and subsequent heat rejection; (iv) gravity-assisted condensate flow at the condenser end; and continues to do so by repetition of the aforementioned steps. As the temperature of the space environment increases, the SMA actuators retract and pull the switch back to the open or “off” position recovering all the axial displacement.

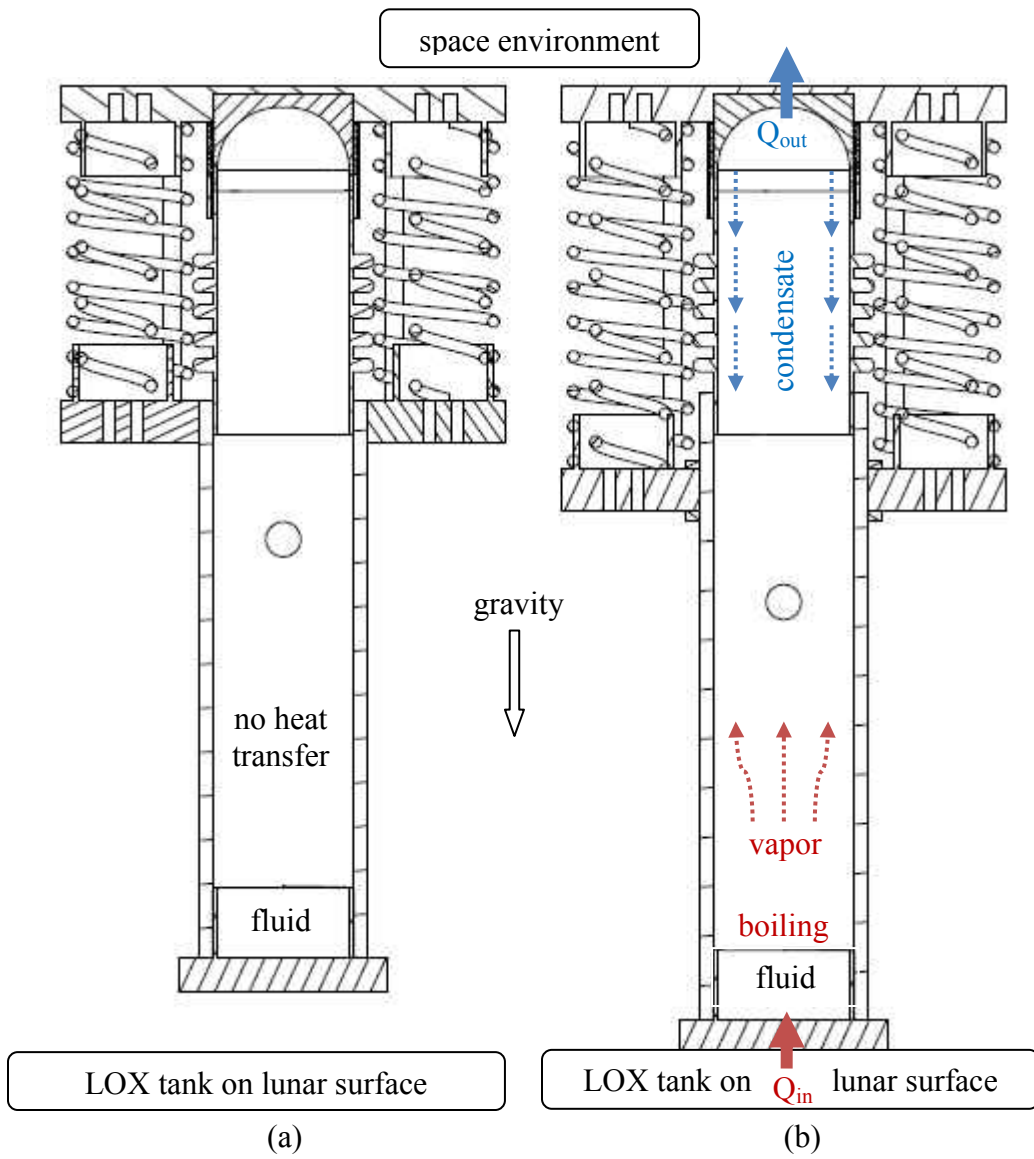


Figure 5.3: Principle of switch operation: (a) The open or “off” position during a lunar day (hot) (b) and the closed or “on” position during a lunar night (cold)

CHAPTER SIX: TEST SETUP AND METHODOLOGY

A setup was built to test the final assembled thermal switch in simulated conditions. First, an adjustable test stand was made to situate the switch in a vertical position to allow for a complete heat transfer cycle inside the heat pipe. To simulate cryogenic conditions, liquid nitrogen inflow and outflow lines were used to control the flow and simulate temperature variation of the space environment that can drop to as low as 40 K. Vacuum conditions were achieved by a glass bell jar connected to a mechanical pump and mounted on a sealed metallic structure with instrumentation feedthroughs and valves. Auxiliary equipment such as power supplies, heat pads, a load cell, an encoder, and thermocouples were also used for testing. Sections of this chapter describe the test setup, methodology, instrumentation and data acquisition using LabVIEW[®] virtual instruments.

6.1 Heat Pipe Evacuation and Charging

The sealed heat pipe was evacuated and charged using a high pressure manifold connected to a mechanical pump, fluid beakers, and the valve on the thermal switch (Fig. 6.1 and Fig. 6.2). Valves, adapters and clear flexible tubing were used to connect the manifold to the heat pipe and charging equipment. The following scheme was used to connect the manifold lines:

- Line #1: to schrader valve on heat pipe
- Line #2: to fluid beaker with tube fully emerged into the liquid
- Line #3: to an empty sealed beaker

- Line #4: to mechanical pump
- All other lines not used (closed valves)

The following procedure was used to charge the heat pipe:

- 1) Heat pipe evacuation: evacuation from one valve with all others closed
- 2) Evacuation of the manifold and line #3
- 3) Line #2 evacuation: with all valves closed, open line #3, then line #2. Due to a change in pressure, the fluid is forced to the empty beaker filling the tubes with liquid; once all of line # 2 is filled with liquid, close all valves.
- 4) Slowly open line # 1 and then line #2. The fluid flows into the pipe.
- 5) Weight the heat pipe before and after charging to determine the amount of fluid transferred.



Figure 6.1: Pressure manifold for heat pipe evacuation and charging

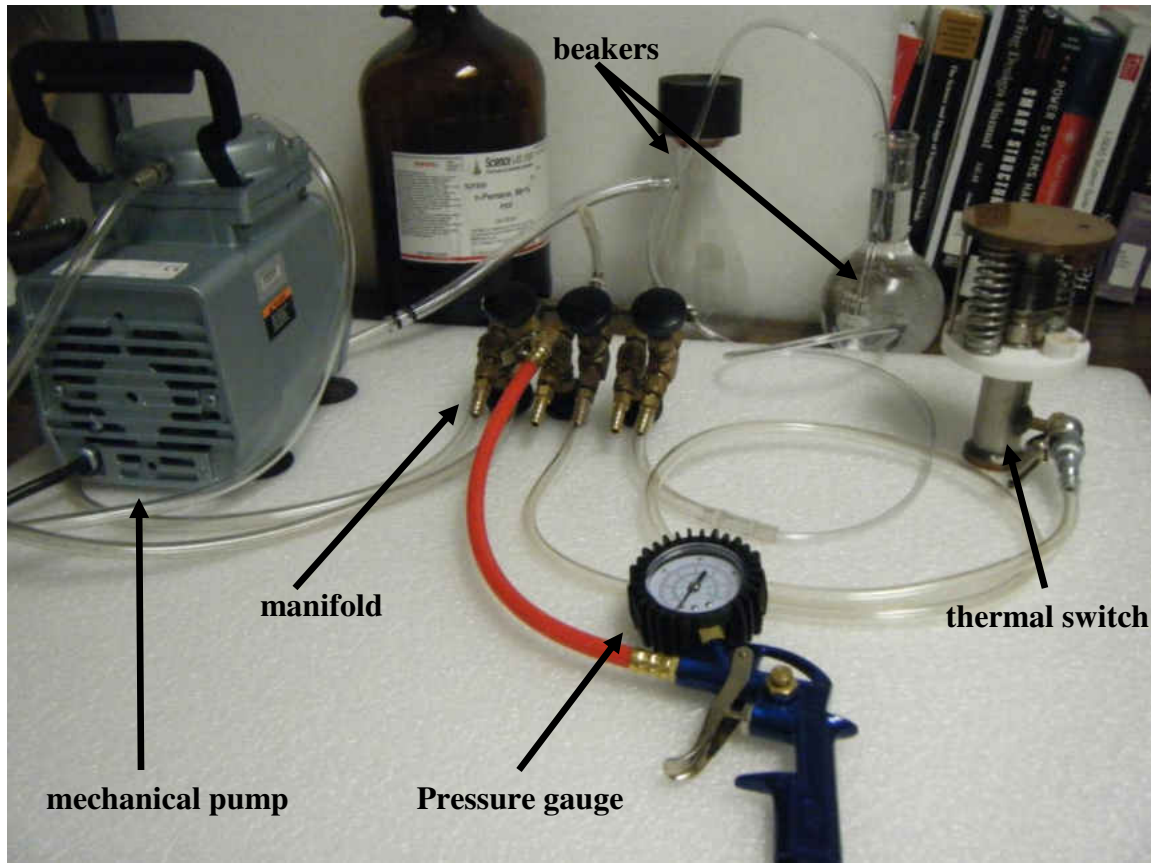


Figure 6.2: Heat pipe evacuation /charging setup

6.2 Thermal Switch Test Setup

As shown in Fig. 6.3, the assembled thermal switch was mounted on an adjustable test stand with copper blocks attached to the switch base on one end and to a load cell at the other end. On the top block, a 6.35 mm hole was drilled at the middle to allow for liquid nitrogen inflow and outflow used to cool the base of the thermal switch. The block was mounted on two lead screws for lowering or raising the switch to adjust the thermal gap. The bottom copper block was directly installed on a 220 N load cell for actuation and thermal contact pressure

measurements. A controllable DC heat pad was placed on the lower block to control the temperature variation during engagement of the switch.

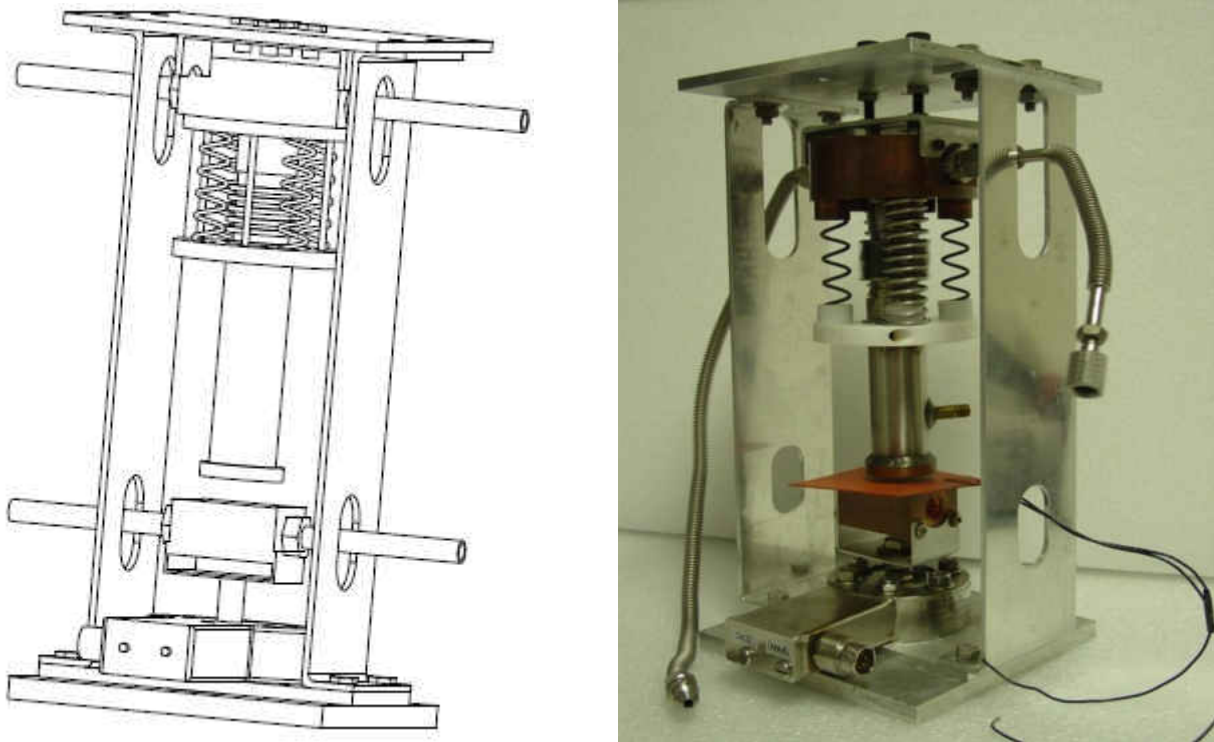


Figure 6.3: Test stand with thermal switch: (a) schematic (b) final setup

To better control the cooling cycles, a single-loop copper tube was wrapped around the actuators as shown in Fig. 6.4. The copper tube inlet was connected to the liquid nitrogen outlet from the top copper block to circulate the fluid around the switch. The copper base of the switch was put in contact with the first two loops to increase conductive cooling. During ambient tests outside the chamber, the copper loop operates as a thermal blanket that provides forced convective cooling for faster test runs that did not require vacuum conditions. This copper loop was made by coiling a straight 6.35 mm copper tube around a PVC pipe with an outside diameter

that corresponds to the base diameter of the switch (Fig. 6.5). To be able to connect the tube to the liquid nitrogen lines, 6.35 mm OD by 6.35 mm flare adapters were connected to both ends.

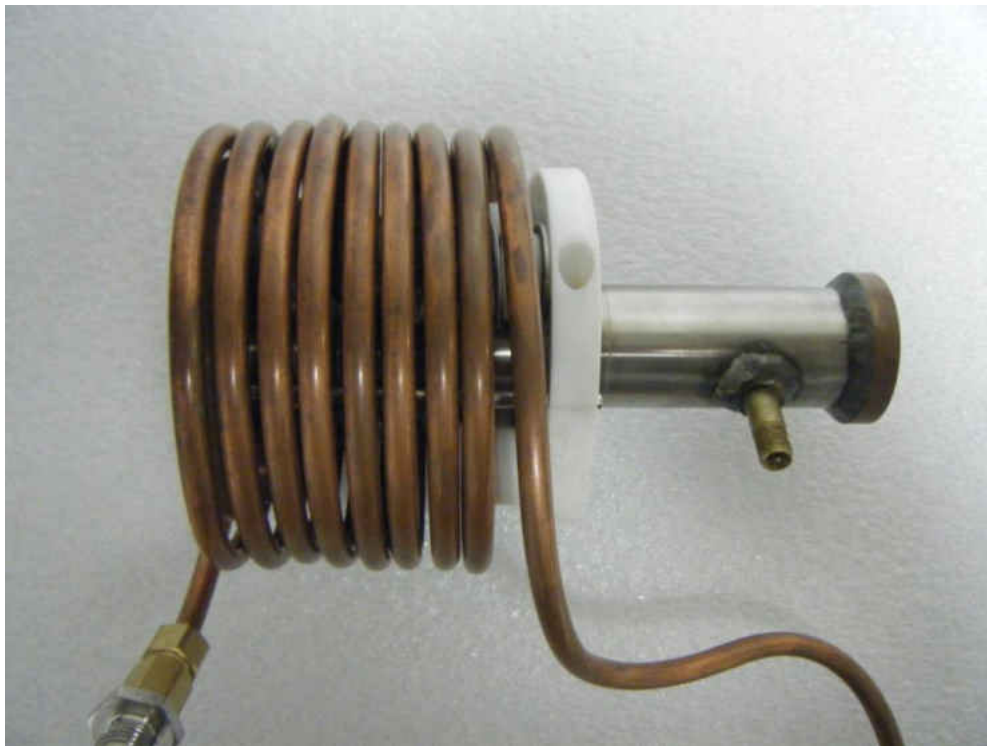


Figure 6.4: Single-loop cooper tube around thermal switch



Figure 6.5: Fabrication of the single-loop cooper tube

To better simulate the actual operation conditions, a vacuum bell jar apparatus was used for testing under vacuum conditions (~20 Micron). The glass housing was mounted on an aluminum base composed of several instrumentation feedthroughs for data acquisition, flow control, and evacuation as shown in Figs. 6.6-9.

- A total of 10 thermocouples were utilized to monitor and control the temperature of the environment, transformation temperatures of the springs, and the temperature gradient across the heat pipe. Thermocouples #1 & #2 were attached to the same SMA actuator, one at the top and the other at the bottom; thermocouples #3-5 were attached to the other SMA actuators to monitor uniformity; thermocouples #6 & #7 were connected to the condenser and evaporator to measure the wall temperatures; thermocouple #8 was attached to the heat pipe mid section (hand-held reader); thermocouple #9 was connected to the heat pad, and finally thermocouple #10 (hand-held reader) was left open to record the chamber temperature.
- A 23 kg Sensotec load cell was used to measure the following: (i) the contact pressure between the lower end of the switch and the heat source (LOX tank in the case of the real application) during the closed or the “on” position, (ii) the net output force of the actuators.
- A low friction probe linear encoder was used to measure the switch displacement as a function of temperature (providing the hysteresis associated with the forward and backward transformation). The encoder was placed directly in contact with the moving Teflon plate and was supported by a stand-clamp fixture.

- A DC power supply was used to control the heat pad temperature so as to vary the temperature at the lower end of the CTPT. Power was controlled outside the chamber by adjusting the input voltage.
- A valve/gauge combination was used with a mechanical pump to monitor and control pressure in the bell jar.
- Fluid feedthroughs were used for inflow and outflow of liquid nitrogen that was used to cool the actuators. The flow was controlled by a low pressure regulator connected to a cylinder of liquid nitrogen.
- A viewing port was provided for a video camera.
- A port was fitted with a safety valve.

Additional components were used such as a rubber gasket that was placed between the glass bell jar and aluminum base to avoid leakage during evacuation, a protection cage that was placed over the bell jar in case of accidental implosion, and insulation was provided around the flow lines to minimize cryogen loss.



Figure 6.6: Glass bell jar with instrumentation feedthroughs

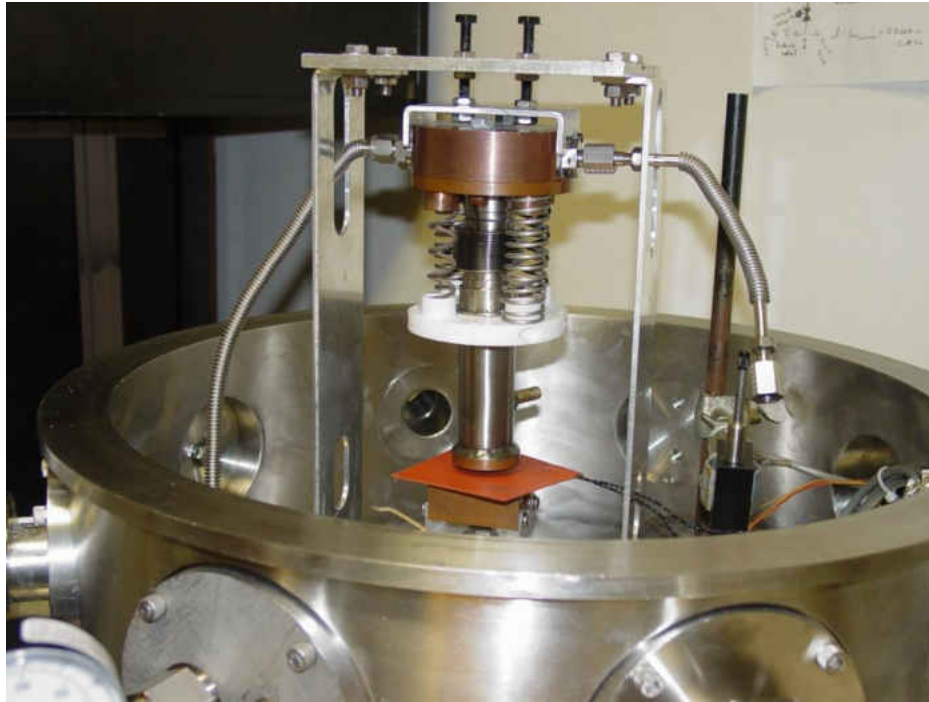


Figure 6.7: Thermal switch inside the bell jar fixture



Figure 6.8: Thermal switch and single-loop cooling coils connected to liquid nitrogen lines

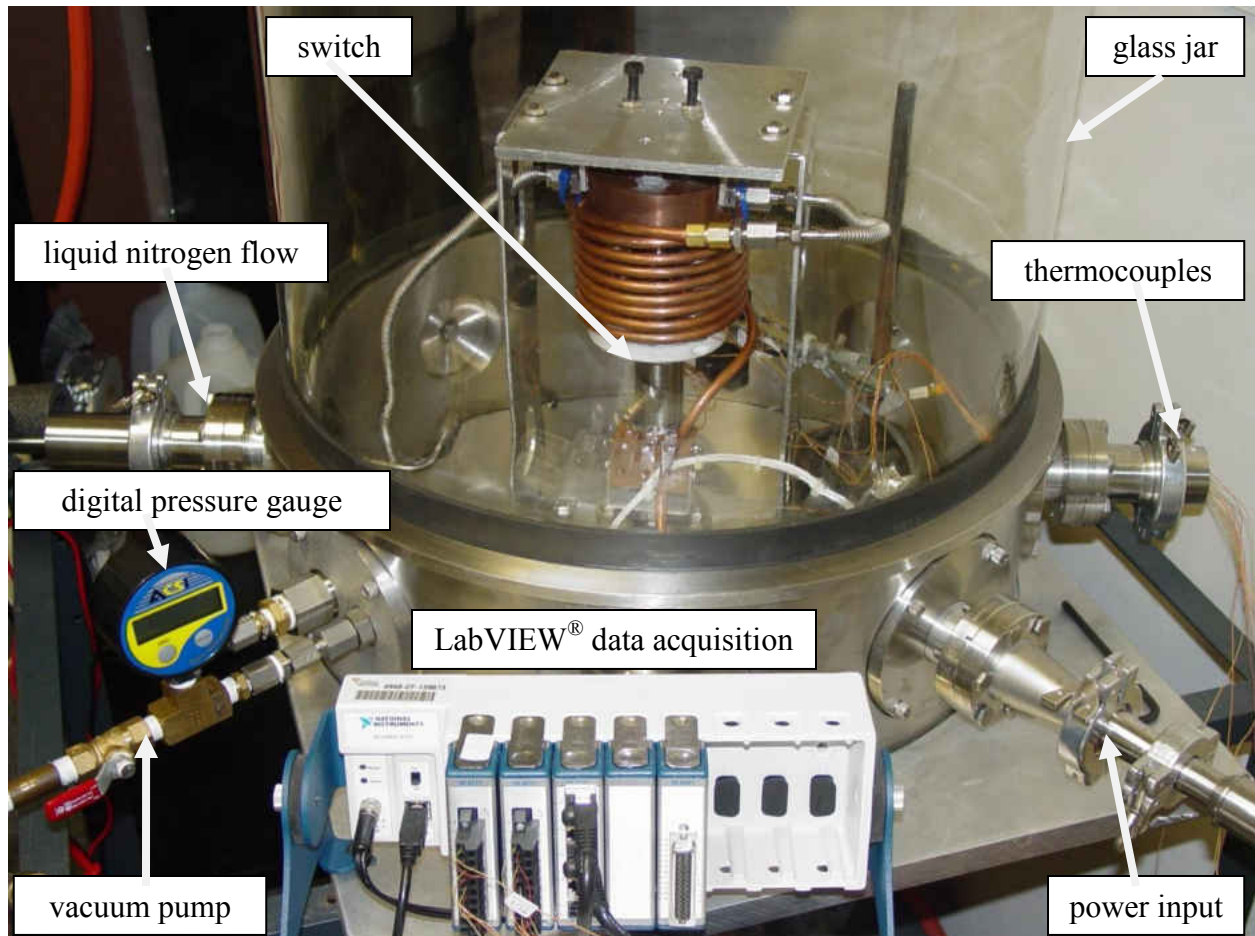


Figure 6.9: Switch in instrumented vacuum bell jar setup for testing. LabVIEW[®] software was used for data acquisition and control of the test temperature conditions (heater and flowing liquid nitrogen through coils).

6.3 Testing Methodology

The cooling and heating rates of the SMA actuators were determined from the temperature-time measurements obtained from the thermocouples on the springs. These measurements ensured that there were constant and uniform heating and cooling rates for each spring. By adjusting the gap between the switch and the bottom block, loads and their corresponding displacements were measured and load-stroke data thus obtained. Additionally,

temperature-stroke results were obtained by recording the displacements from the encoder with temperature. The heat transfer through the heat pipe was quantified by controlling the heat pad temperature and adjusting the power input as the switch made and broke contact. The tests were run with and without the working fluid. The power required to maintain constant pad temperature when the switch was engaged was a measure of the heat transferred through the heat pipe.

6.4 Instrumentation and LabVIEW[®] Data Acquisition

Data was collected simultaneously by a compact data acquisition system with multiple C-series modules with direct signal connectivity for each transducer (Fig. 6.10). Command Scripts were developed and executed using LabVIEW[®]. The following sections describe the virtual instruments used to collect data.

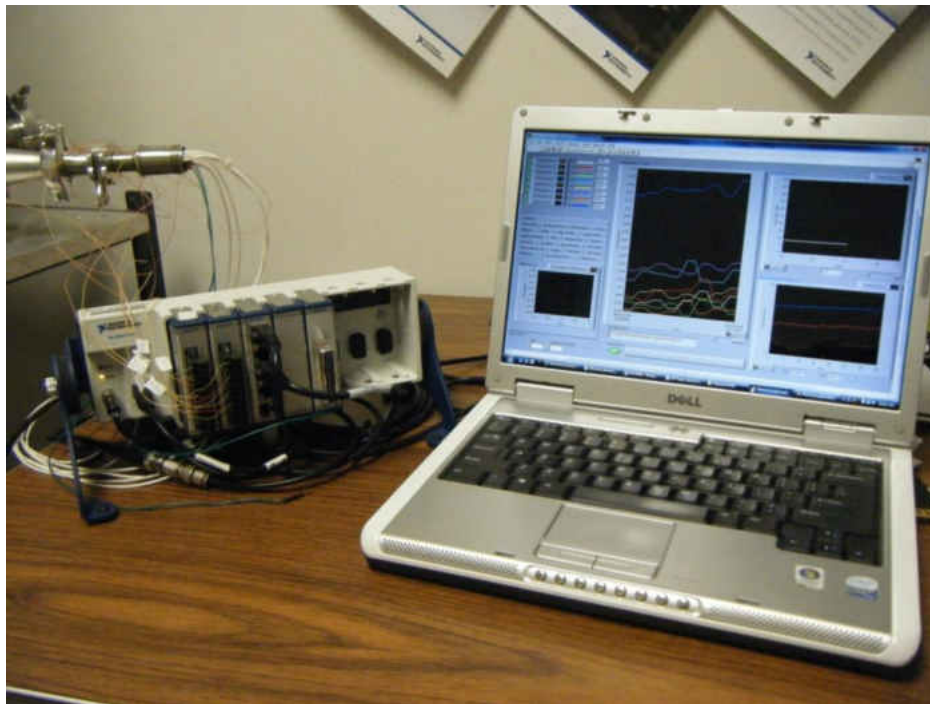


Figure 6.10: LabVIEW[®] data acquisition system

6.4.1 Temperature Virtual Instrument

The virtual instrument block diagram used to measure temperature is shown in Fig. 6.11a. A while loop was used to continuously collect data at a specified sampling rate. A 100 ms interval was used between measurements. Data was acquired from a total of 8 thermocouples (denoted by TC1-8).

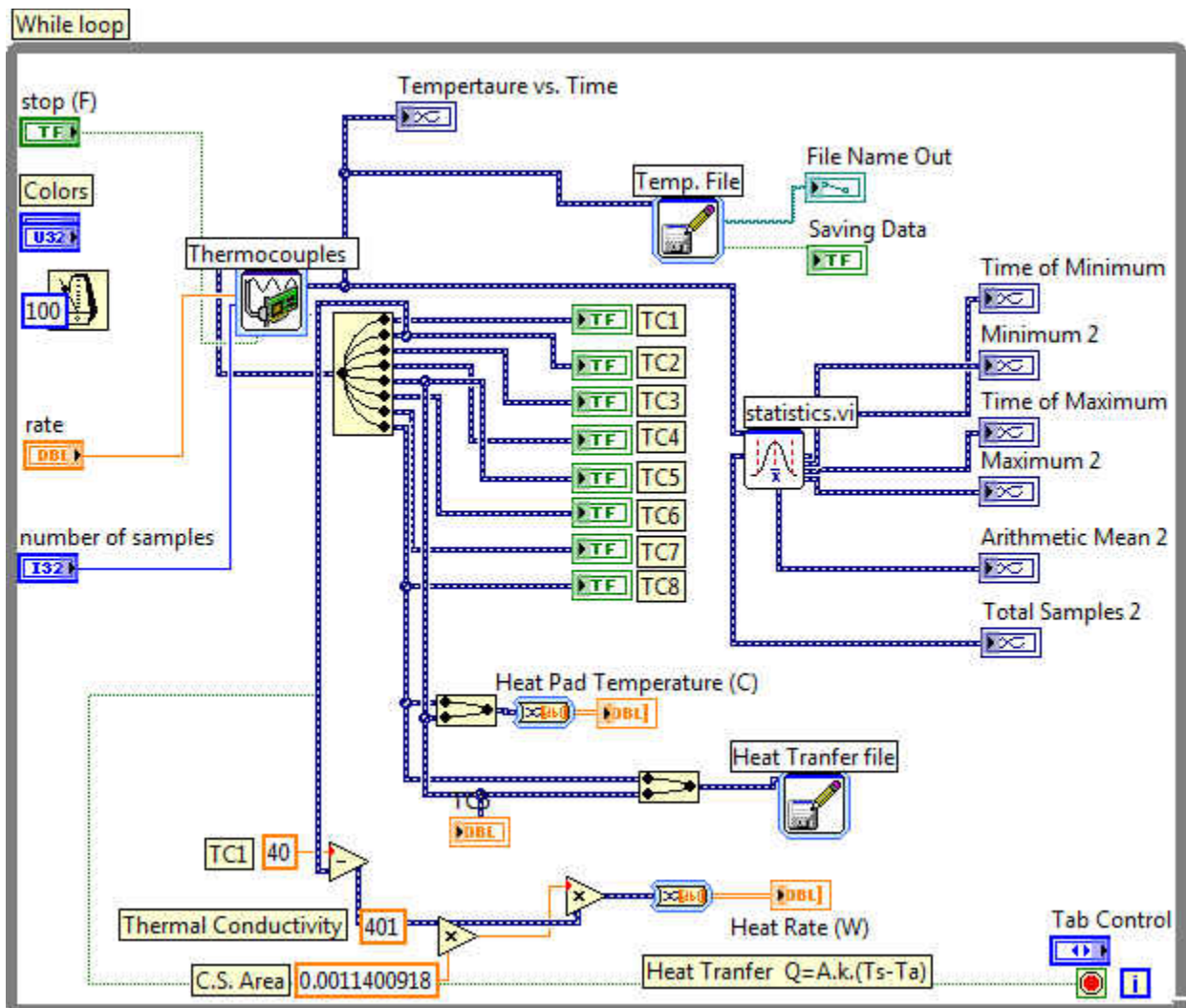


Figure 6.11a: Virtual instrument block diagram for temperature measurement

By wiring every block correctly, a front panel was constructed to run a script and monitor the data (Fig 6.11b). The front panel was built with graphical representations, numerical indicators, knobs and buttons. Boolean indicators (green buttons) were used to indicate proper functioning of all thermocouples.

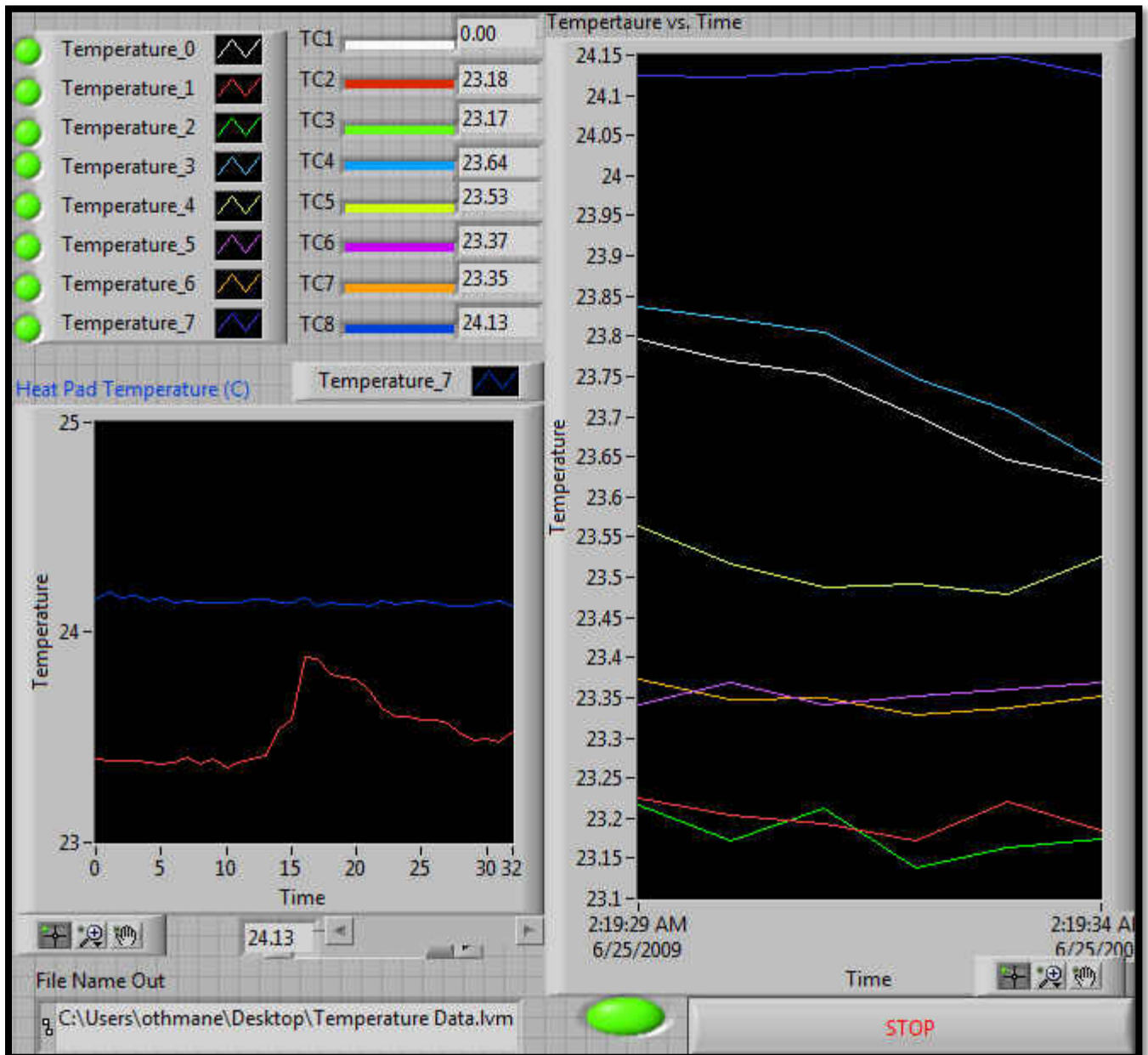


Figure 6.11b: Virtual instrument front panel for temperature measurement

6.4.2 Displacement Virtual Instrument

Similar to the previous case, a while loop was used with shift registers for record keeping. This VI recorded displacement data of the springs in both phases (Fig.6.12a).

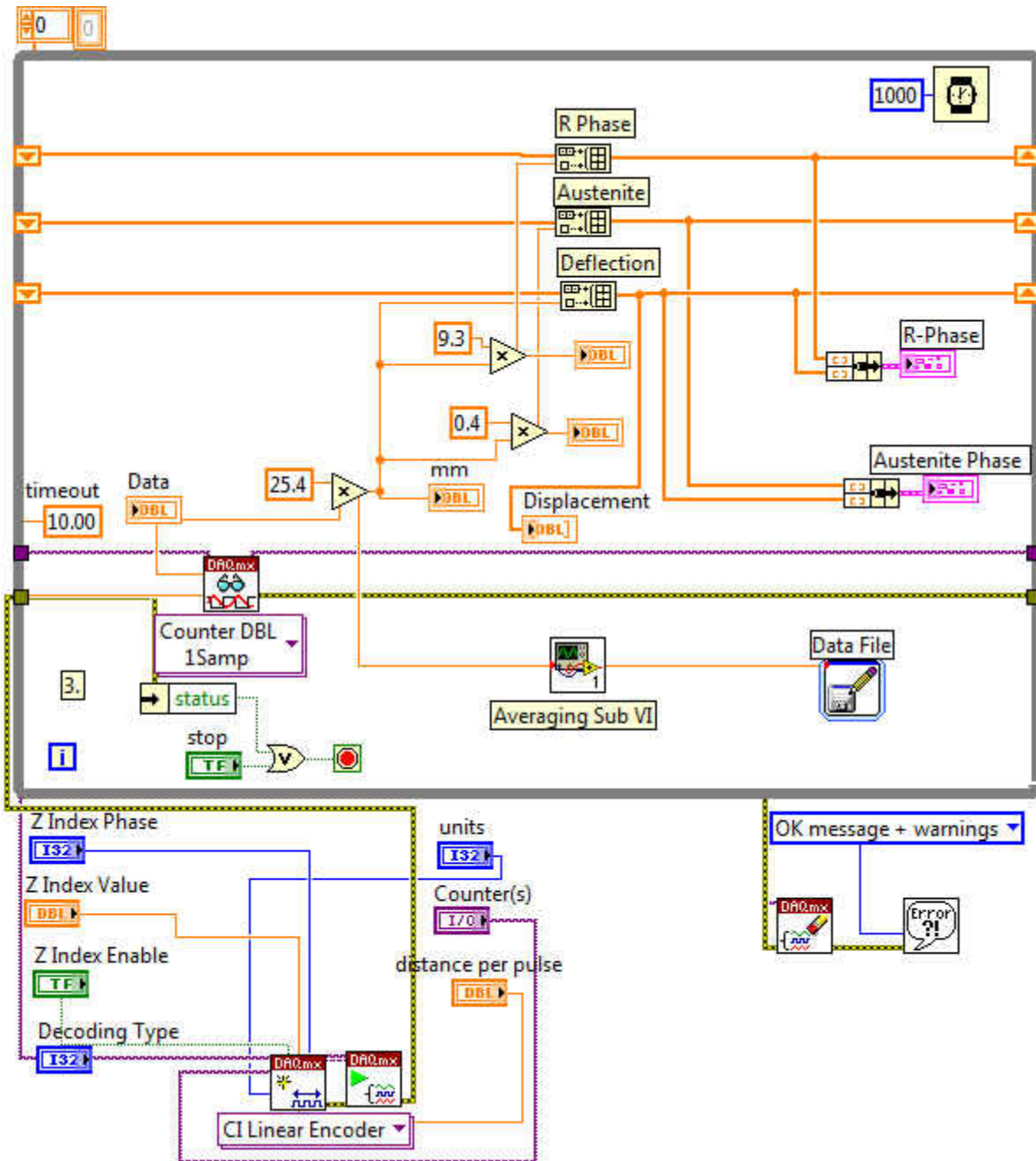


Figure 6.12a: Virtual instrument block diagram for displacement measurement

The corresponding front panel is shown in Figure 6.11b.

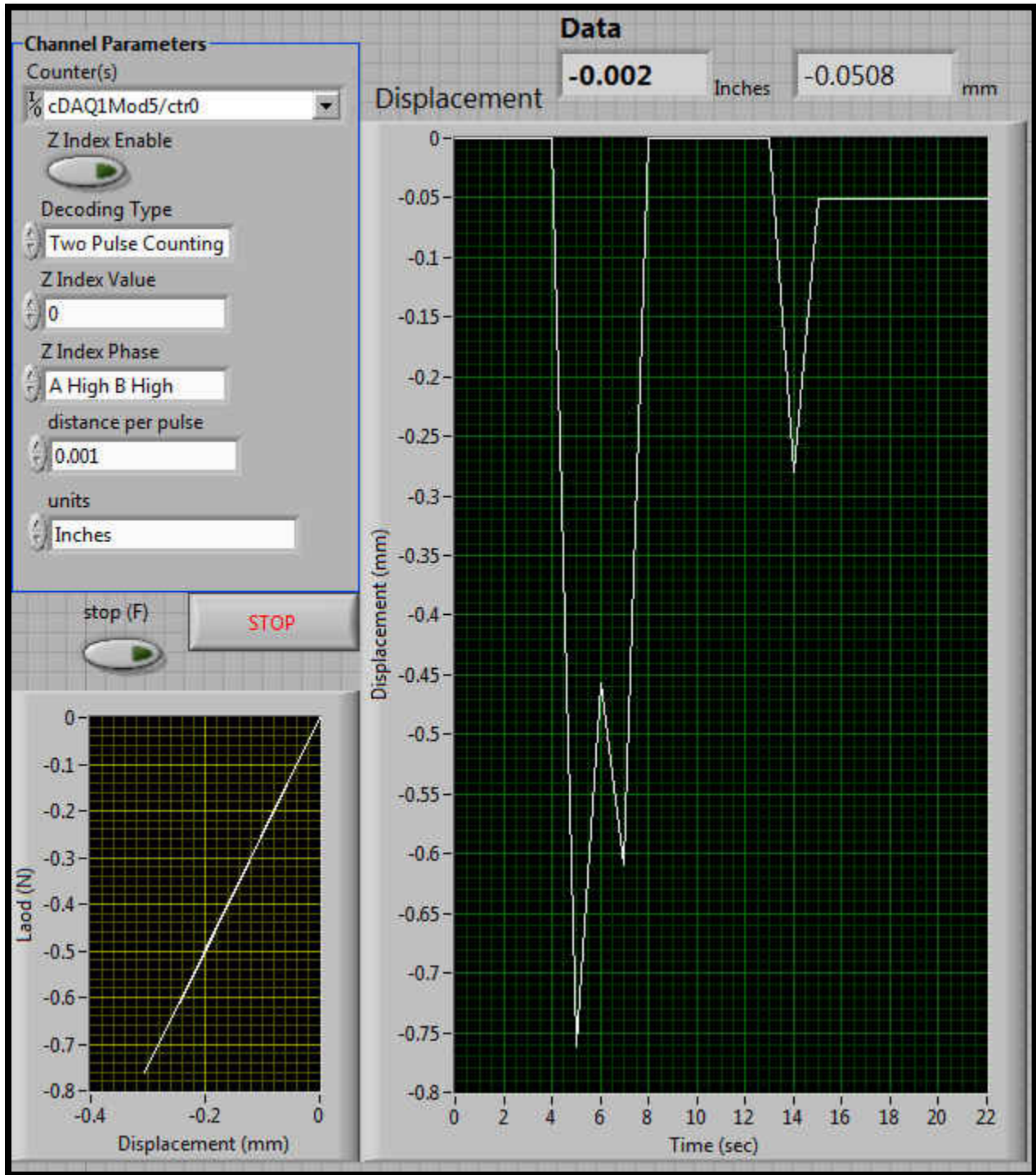


Figure 6.12b: Virtual instrument front panel for displacement measurement.

6.4.3 Load Virtual Instrument

In this block diagram, a while loop and a case structure were used to collect load data from the load cell. Various parameters such as physical channels, excitation voltages and rates were appropriately selected.

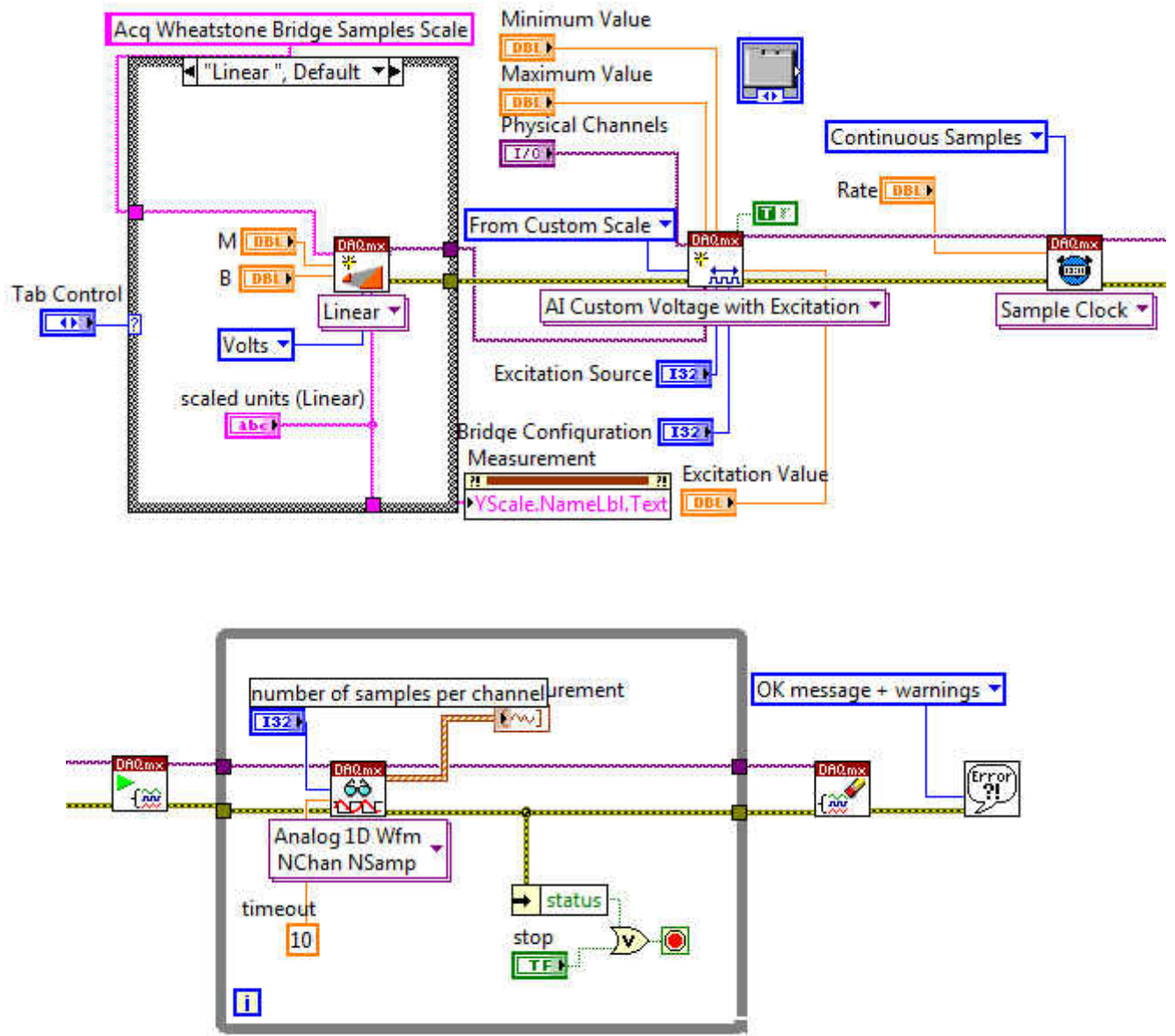


Figure 6.13a: Virtual instrument block diagram for acquiring load cell data (NI code)

The corresponding front panel had the option to choose channel parameters, timing parameters, and scaling parameters (Fig. 6.13b). The results were plotted in order to monitor the data during data collection.

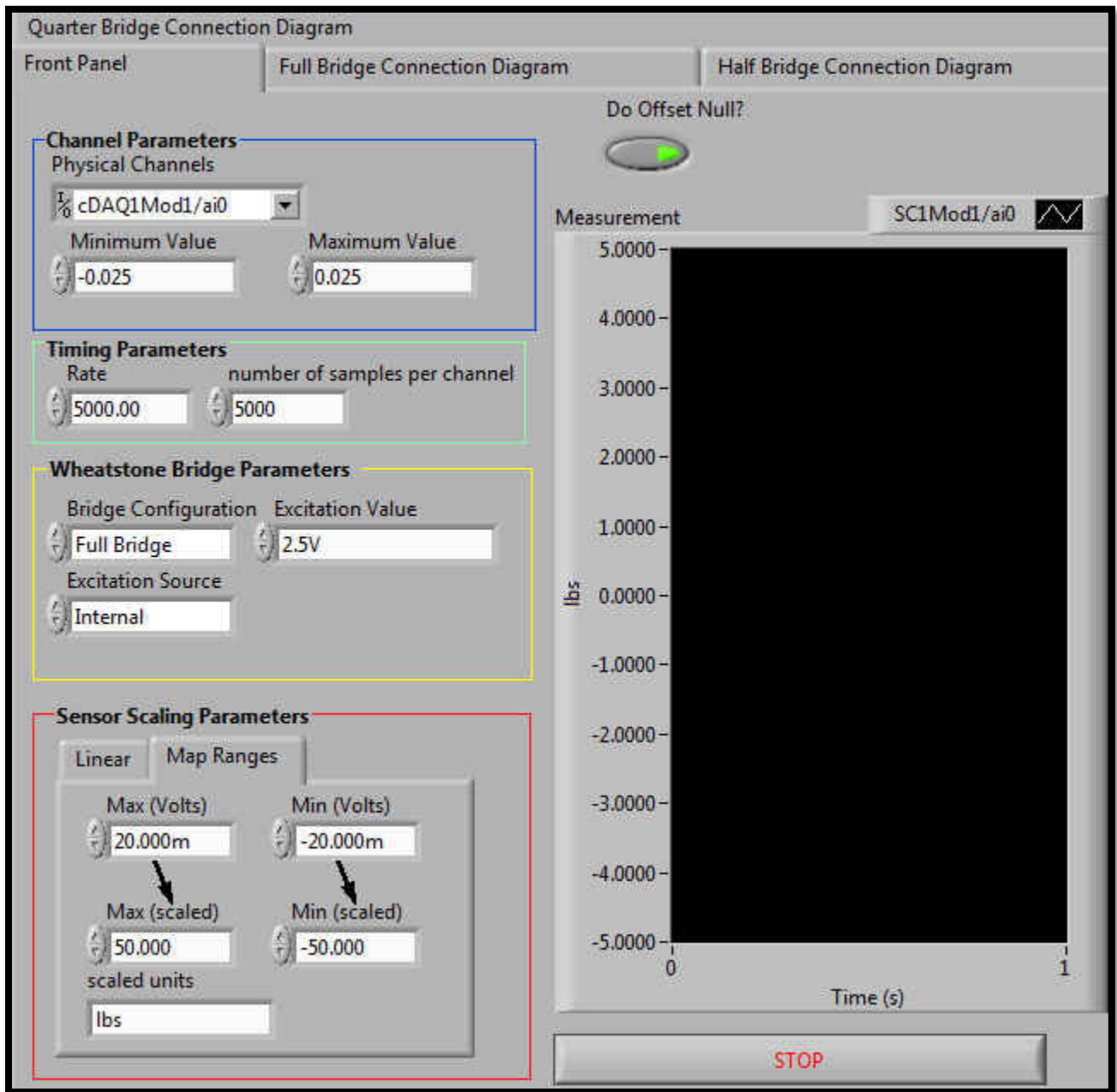


Figure 6.13b: Virtual instrument front panel for acquiring load cell data (NI code)

CHAPTER SEVEN: RESULTS AND DISCUSSION

This chapter presents and discusses results related to various aspects of the performance of the shape memory actuators and the overall thermal switch.

7.1 Differential Scanning Calorimetry

The forward and reverse phase transformation temperatures for the $\text{Ni}_{47.1}\text{Ti}_{49.6}\text{Fe}_{3.3}$ wire used to make the springs were characterized using a Perkin Elmer Diamond differential scanning calorimeter before and after shape setting. Samples were cut using a low speed cutting saw. The first test was carried out to determine the transformation temperatures of the shape set wire. The DSC curves are shown in Fig. 7.1 and reflect both the exothermic and endothermic processes resulting from the cooling and heating cycles between 35 °C and -80 °C at a rate of 20 °C/min. The peaks identify the start and finish of the phase transformation (R-phase start (R_s), R-phase finish (R_f), austenite start (A_s), and austenite finish (A_f), respectively) during cooling followed by heating. As mentioned previously, the R-phase exhibits a narrow transformation hysteresis as shown by the difference in the peak temperatures (approx. 5 °C).

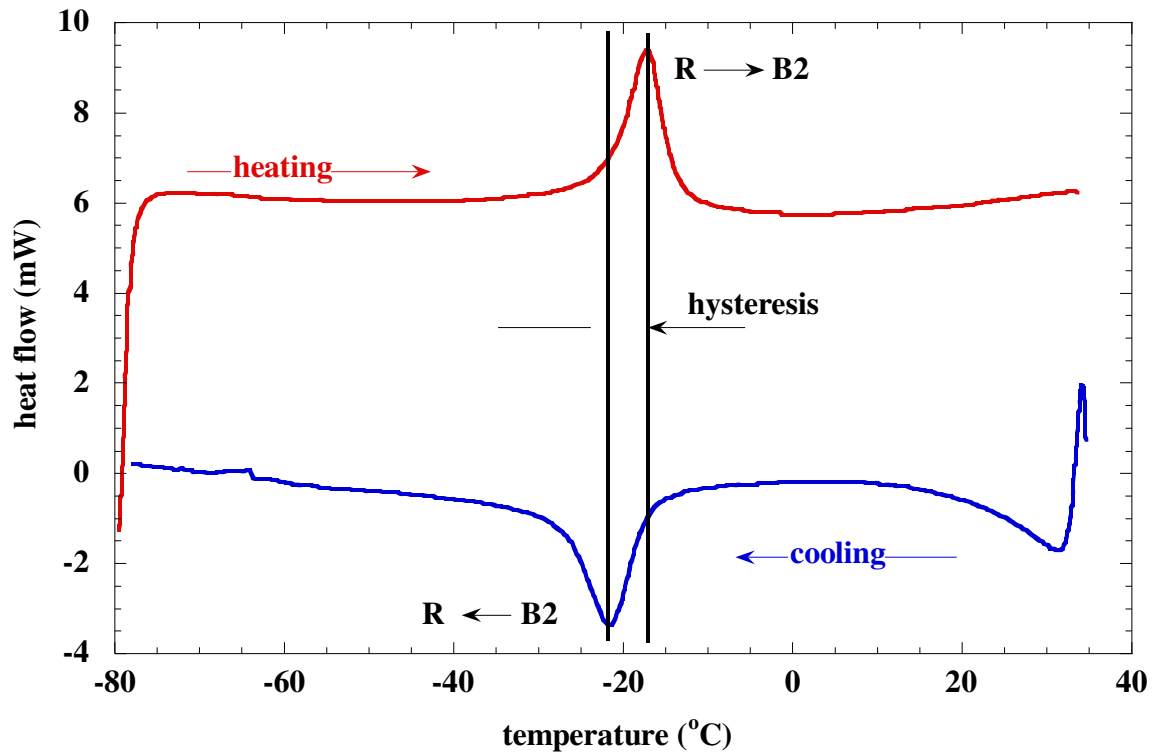


Figure 7.1: Differential Scanning Calorimetry curves of the shape set NiTiFe wire

Two additional samples were prepared and tested between 50 °C and -80 °C at a rate of 20 °C/min. A second sample was cut from as-received wire without heat treatment. The third sample was cut from a spring that was thermally and mechanically cycled (60 times). Heat treatment of the first sample lowered the transformation temperatures by a few degrees with the same hysteresis observed as in the second sample without heat treatment. The transformation temperatures of the third sample shifted to higher temperatures with a narrower hysteresis. The combined DSC curves are shown in Fig. 7.2 and the results summarized in Table 7.1.

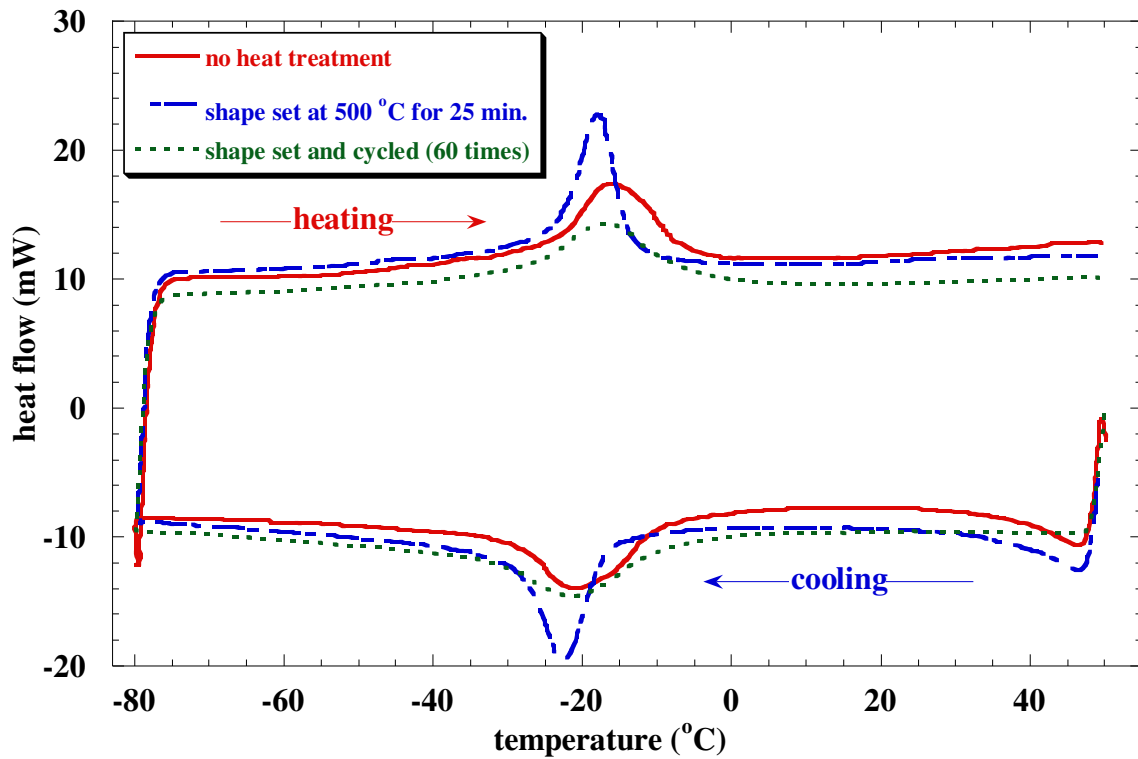


Figure 7.2: DSC response of NiTiFe in the as-received, shape set and tested conditions

Table 7.1: Transformation temperatures of NiTiFe in the as-received, shape set and tested conditions.

Sample condition	R_s (°C)	R_r (°C)	A_s (°C)	A_r (°C)	Hysteresis from peaks (°C)
No heat treatment (As received)	-10.70	-27.76	-25.15	-6.14	4.38
Shape set at 500 °C for 25 min	-16.75	-28.99	-23.01	-13.44	4.71
Shape set and cycled (60 times)	-9.78	-33.73	-27.74	-5.66	4.01

7.2 SMA Actuators Temperature Distribution

To ensure efficient thermal contact between the bottom of the switch (the evaporator) and the heat sink, the switch was vertically aligned in order to actuate without inclination. This was accomplished by heating and cooling all four SMA springs at the same rate. Cooling was controlled by liquid nitrogen flow through the switch base and the loop coil. The heating cycle was controlled by free convection in air. Thermocouples were attached to each spring at the same height to verify that the springs exhibited the same temperature at all times (Fig. 7.3).

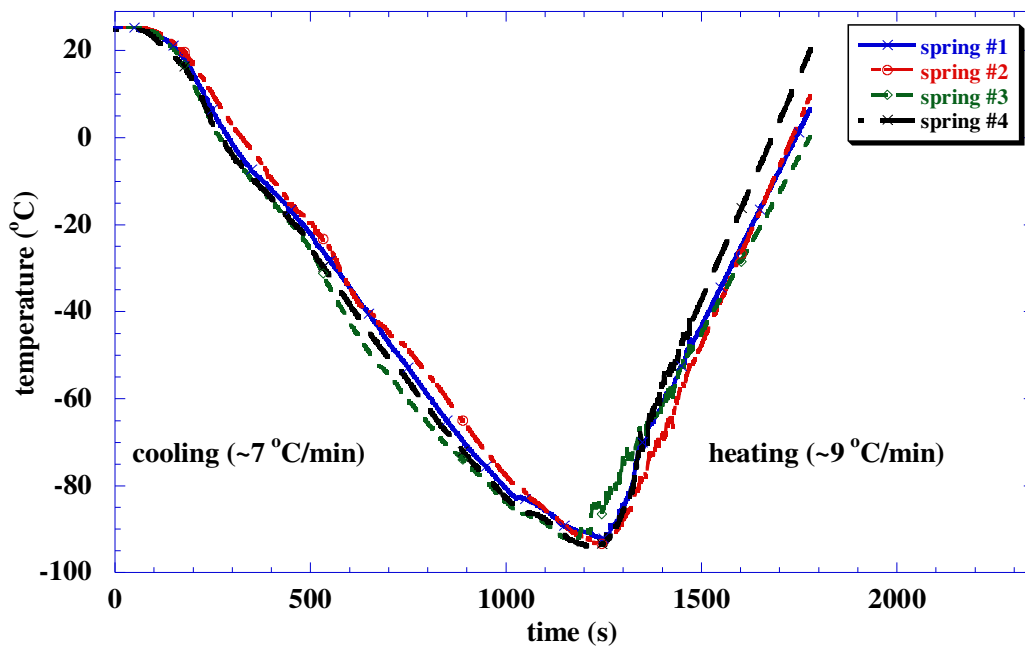


Figure 7.3: Cooling and heating rates of the four SMA helical springs

Since all springs were cooled by conduction through the switch base, a constant cooling rate of 7 °C/min was obtained by maintaining constant liquid nitrogen flow during the cooling

cycle. During the convective heating cycle, a uniform heating rate of 9 °C/min was obtained. All the springs were shown to exhibit the same temperature during a complete thermal cycle. However, each SMA spring did not exhibit the same temperature along its length due to conductive cooling at the upper end. To quantify the thermal gradient along the spring, three thermocouples were attached on the same spring at different locations (points 1, 2 and 3 in Fig. 7.4). As expected, the upper section of the spring cools faster than the lower coils resulting in a temperature gradient along the spring (Fig. 7.4). This gradient can cause an heterogeneous phase transformation that widens the range of the transformation and the hysteresis.

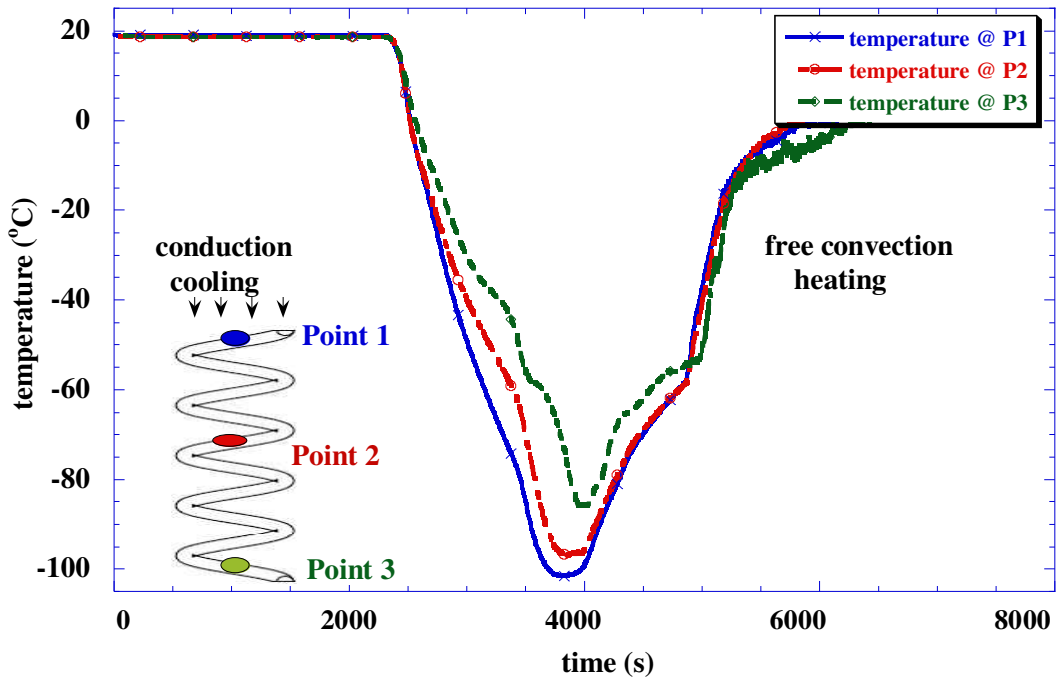


Figure 7.4: Temperature distribution along the length of the SMA spring

Temperatures used to analyze and quantify the performance of the switch were reported from the middle of the spring (Point 2).

7.3 Performance of the Shape Memory Alloy Helical Actuators

The experimental load-extension results associated with the actuators in the austenite and R-phase with the bias springs are shown in Fig. 7.5 and compared with the theory (Eq. (3.6b)). This was done in order to determine the required bias force as the SMA springs transform between their high temperature, stiffer phase and their low temperature, more compliant phase. The response of the high temperature phase was obtained by loading the helical actuators at room temperature in a servo-hydraulic load frame; on the other hand, the low temperature response was obtained while testing the switch by controlling position and measuring load. The experimental SMA spring constants were found to be 3.72 and 0.51 N/mm for the two phases and compared well with the theory (4.22 and 0.99 N/mm, respectively).

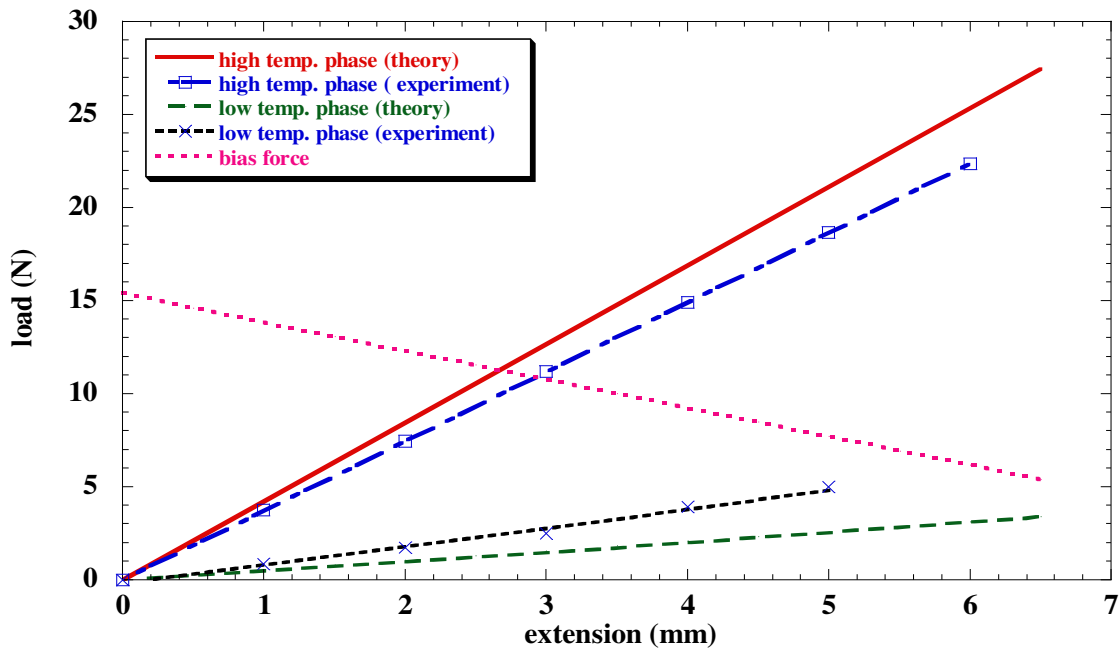


Figure 7.5: Experimental and theoretical load-extension response of the springs in the austenite and R-phase and the bias springs

The results corresponding to the displacement of the switch as a function of temperature are plotted in Fig. 7.6. Initially when in the austenite phase, the switch is maintained in the open or “off” position providing thermal isolation. The SMA helical actuators are in their stiffer phase and are pre-loaded with a bias force generated from the 5 mm primary compression of the bias springs that yield a 29 N force, 4 mm pre-compression of the bellows that yield a 7.7 N force, and from the force due to gravity of the components that exert 2.3 N. As the actuators cool and reach the temperature for transformation from austenite to R-phase ($-15.2\text{ }^{\circ}\text{C}$ or R_s), the switch starts to expand until $-75.5\text{ }^{\circ}\text{C}$ (R_f) following 5 mm stroke. Conversely, as the switch heats back to room temperature, the actuators transform to the parent phase (A_s at $-61.3\text{ }^{\circ}\text{C}$ and A_f at $3.1\text{ }^{\circ}\text{C}$) concomitantly recovering all the axial deformation imposed by the bias load. The hysteresis observed in the response is attributed to the temperature gradient along the length of the SMA actuators. Evolution and full recovery of the phase transformation from the parent phase to R-phase are shown in Fig. 7.6 along with the associated hysteresis. The first 3 cycles not shown here were mainly responsible for stabilizing the material response and relieving the tensile and compressive residual stresses at the inner and outer radii of the coil. Subsequent cycles show consistent repeatability of the phase transformation with minimal to no open loop axial deformation as shown in Fig. 7.7.

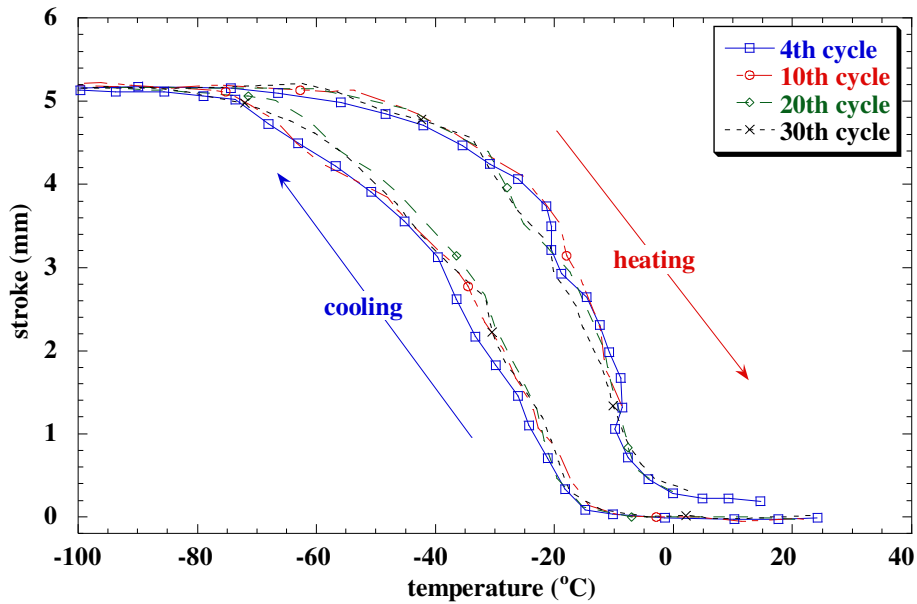


Figure 7.6: Stroke-temperature response of the shape memory helical actuators. The transformation temperatures R_f , R_s , A_s , and A_f under the bias load are -15.2 , -75.5 , -61.3 and $3.1 \pm 2^\circ\text{C}$ respectively.

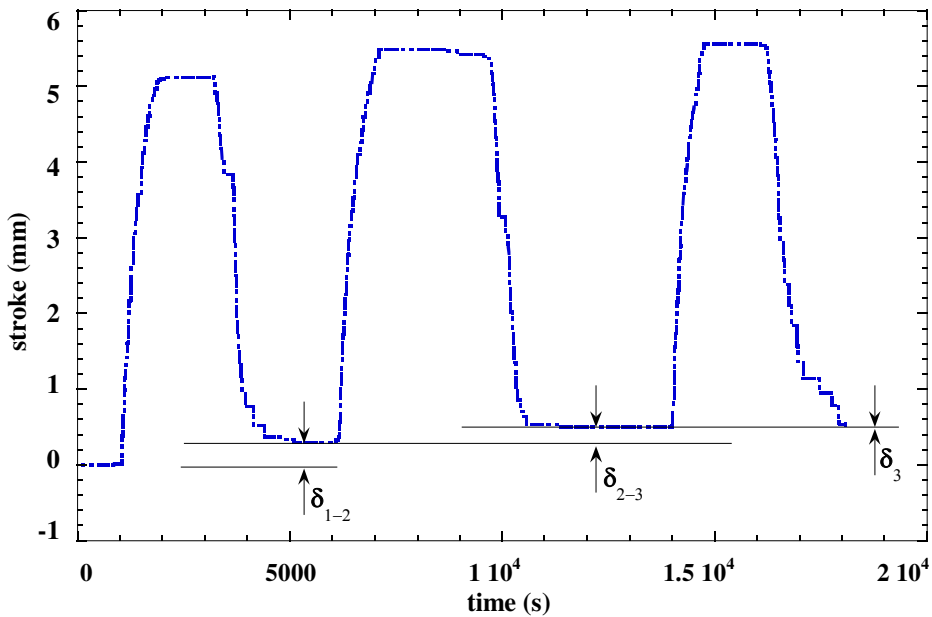


Figure 7.7: Stroke-time response of the shape memory helical actuators to assess open-loop strains. After the third cycle from room temperature to -100°C at $10^\circ\text{C}/\text{min}$, the open loop axial deformation is negligible as shown by δ_3 for an overall switch extension of 5 mm.

Figures 7.8a-d show the resulting thermal switch deflection under different bias loads (by altering the stainless steel springs). These plots demonstrate the flexibility in tailoring the gap between the heat source and the thermal switch.

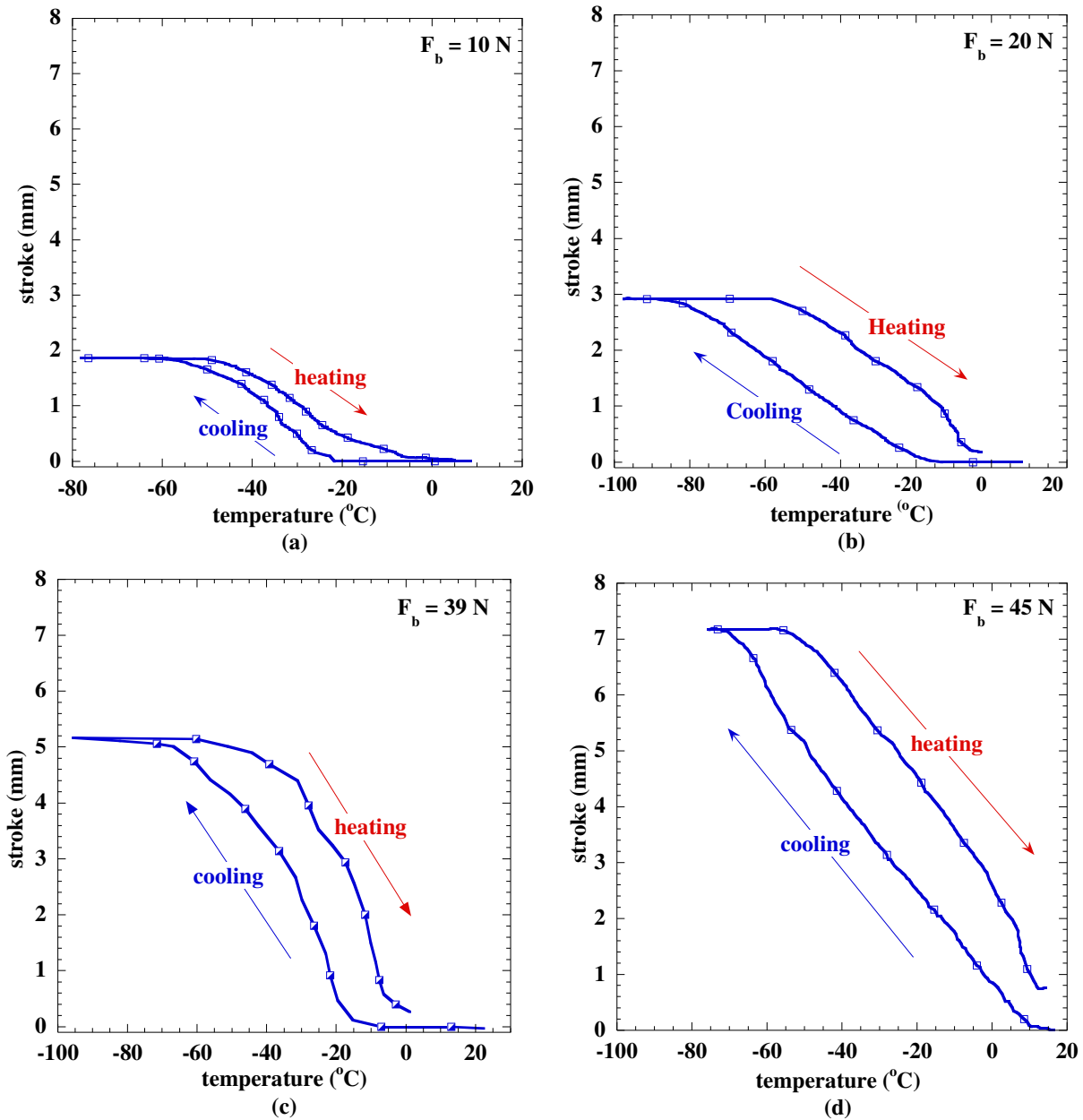


Figure 7.8: Stroke-temperature response of the shape memory helical actuators under varying bias loads. F_b denotes the total bias force from stainless steel springs, bellows and weight of the heat pipe. The maximum stroke for (a), (b), (c), and (d) are 1.85, 2.94, 5.0, and 7.13 mm, respectively. The graphs y-axes are scaled identically.

The results presented in Fig. 7.8 are plotted against time in Fig. 7.9.

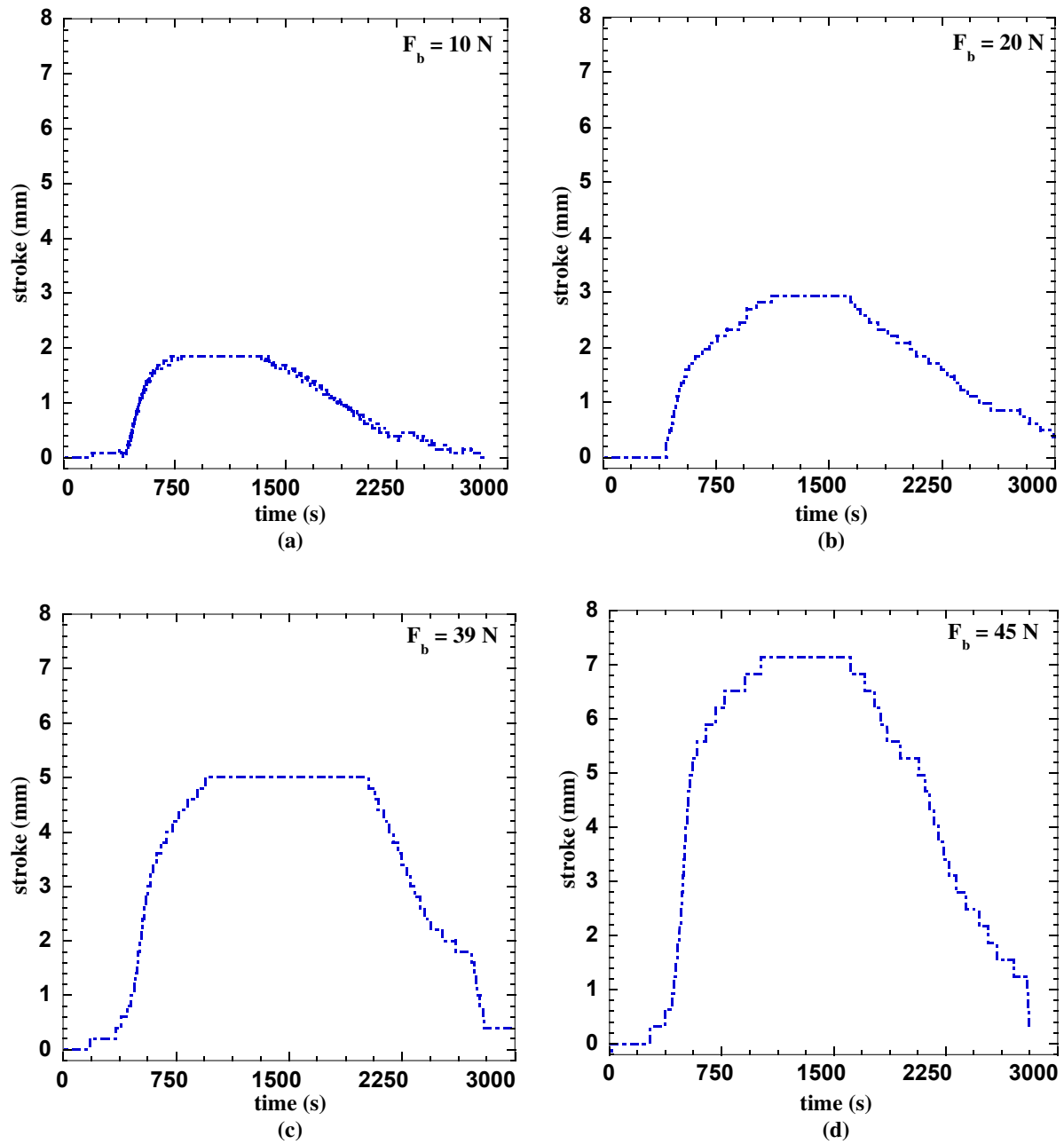


Figure 7.9: Stroke-time response of the shape memory helical actuators under varying bias loads. F_b denotes the total bias force from stainless steels springs, bellows and weight of the heat pipe. The graphs y-axes are scaled identically.

Using the load-stroke data acquired, the corresponding shear stresses in the springs were back calculated from Eq.3.8b and shown in Fig 10. Initially when in the austenite phase, the NiTiFe springs were pre-stressed to 9 MPa due to the bias load. As the actuators cool to below the transformation temperature, the shear stresses increase up to 38 MPa in each actuator and 99 % is recovered during the reverse transformation (for 5 mm stroke against a total force of 39 N). The results plotted in Fig. 7.10 consider the pre-stressed state as the zero point of reference.

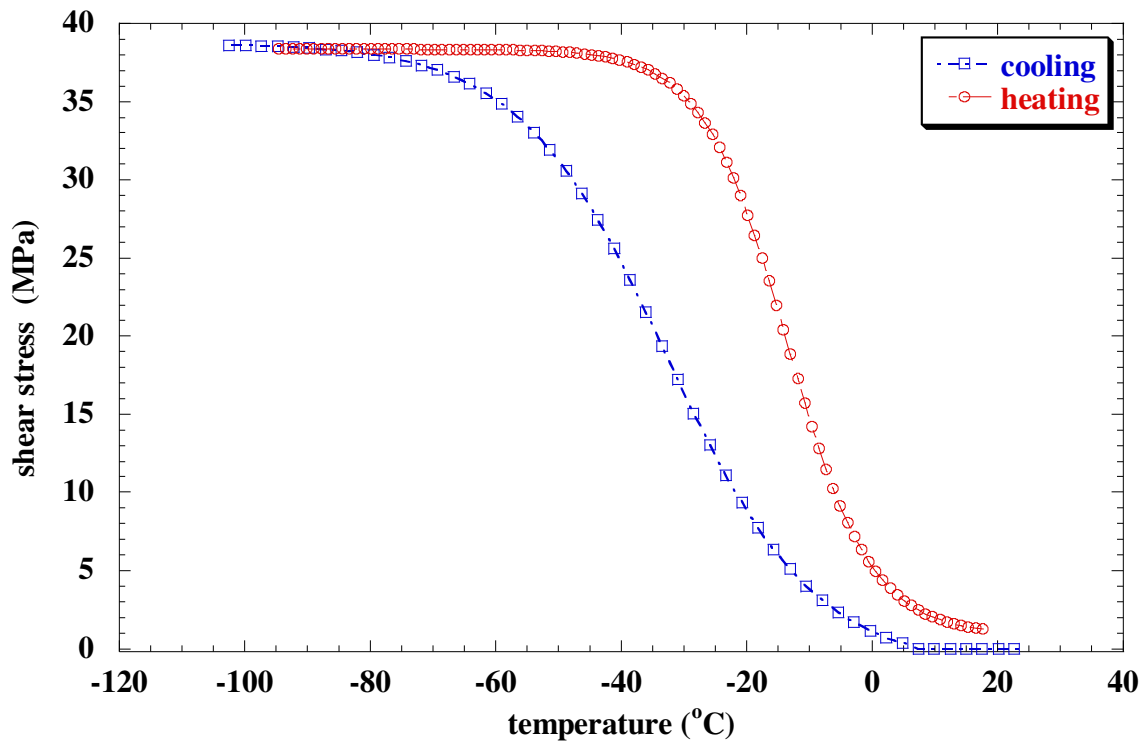


Figure 7.10: Shear stress evolution with temperature in a SMA spring during 5 mm extension against a total bias load of 39 N (temperature measured at mid-section of SMA spring)

The effect of load on the transformation temperatures was also assessed. As described by the Clausius-Clapeyron equation (Equation 7.1), an increase in stress, σ , causes an increase in temperature, dT , above the equilibrium temperature, T_o , for the phase transformation to occur.

$$V \cdot \frac{d\sigma}{dT} = -\frac{\Delta H_{M \rightarrow A}}{T_0 \cdot \varepsilon} \quad (7.1)$$

In the above equation V is the volume associate with the phase transformation and H is the enthalpy change between martensite and austenite. The stress-temperature dependence was determined experimentally as shown in Fig. 7.11. The transformation temperatures (R_f , A_s , R_s , and A_f) increase as the load increases as a result of changing the bias springs.

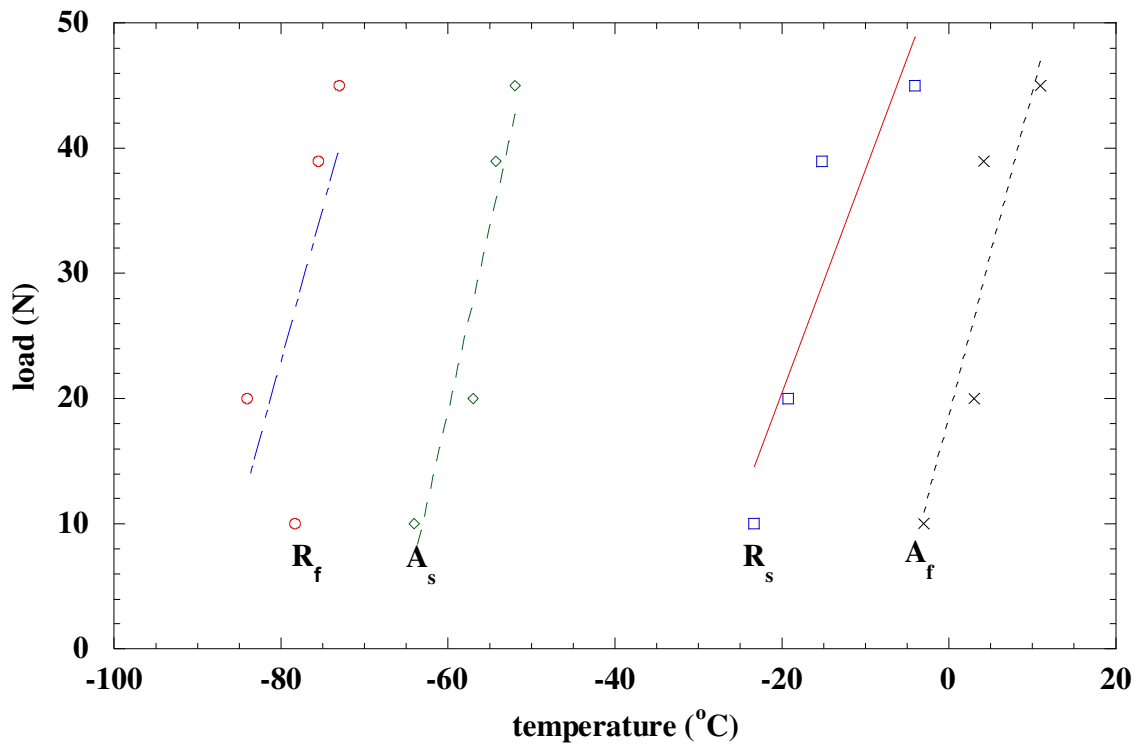


Figure 7.11: Effect of load on transformation temperatures

7.4 Performance of the Thermal Switch

To better quantify the heat transfer at the lower end of the heat pipe, an effort was made to measure the contact pressure at the interface of the evaporator and the heat source. Experiments were performed for both bare contact with the heat pad and also with using grease to measure the minimum required contact force that yielded maximum heat flux. A gradual increase in the heat rate was observed up to a contact pressure of 1.7 kPa, (corresponding to 1.75 N), following which the heat rate became generally constant as shown in Fig. 7.12. As previously described, the contact force was determined with stroke as shown in Fig. 7.13. For an extension of 5mm, which was the objective of the initial design, the force was measured to be 1.93 N which was adequate for obtaining good heat transfer as see in Fig. 7.12.

The measured contact pressures for adequate heat transfer are low due to the 3.175 mm thick silicone rubber layer surrounding the heating elements. In all the measurements reported, the heat pad was placed on top of the lower copper block to directly heat the evaporator section during thermal contact. An attempt was made to heat the copper block itself, but the measurements yielded erroneous results due to unsteady conduction through the block and considerable heat losses to other components in direct contact such as the load cell bracket.

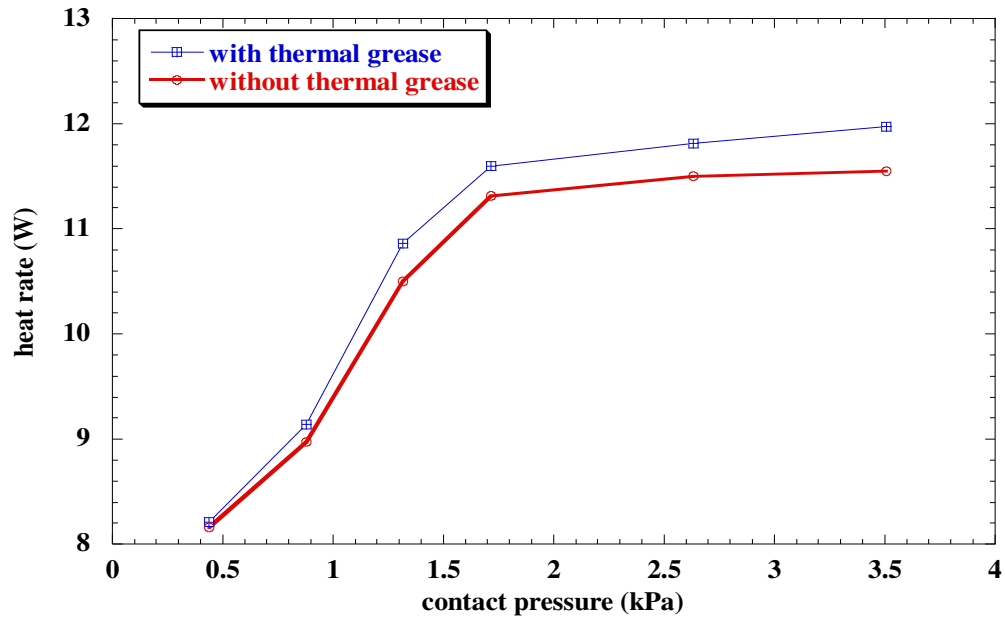


Figure 7.12: Heat transfer rate as a function of contact pressure

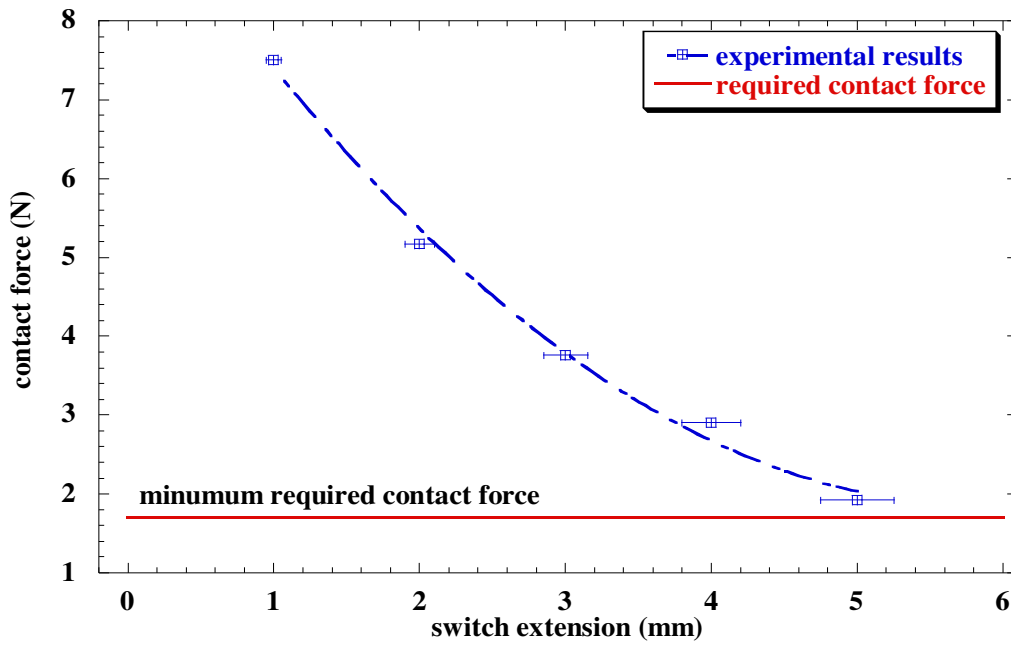


Figure 7.13: Contact force with switch extension. The minimum required contact force is from Fig. 7.12.

Having defined the required contact pressure, quantification of the heat transfer due to conduction along the walls of the heat pipe and two-phase heat transfer involving the working fluids were examined in Figs. 7.14, 7.15a-d, and 7.16a-d. Initially, the switch was tested without any working fluid to determine the conductive heat transfer along the walls of the pipe. This was done mainly to obtain a reference or baseline measurement in order to quantify the heat transport through the heat pipe. This is shown in Fig. 7.14 by heating and cooling the switch (through points A- D) and quantifying the heat transfer by measuring the power input to the heaters. Starting from room temperature with no thermal contact, the heat pad is heated to a constant temperature while cooling the switch (point A on the plot). As soon as the switch engages, the temperature of the heat pad drops and reaches quasi-thermal equilibrium after some time (point B). Once in equilibrium, the cycle was followed by a gradual increase in power to go back to the initial temperature at A (point C). As a result of heating the actuators, the switch moves to the open or “off” position and the heat pad temperature increases due to break in contact. Finally the input power is reduced to reach the initial starting point to close the thermal cycle. As a consequence of energy conservation, the heat rate is considered constant assuming steady state and no heat generation. However, at some time after engaging the switch, there is a decrease in heat flux due to a decrease in the temperature gradient, or due to overheating of the fluid causing film boiling and eventually dry out. The amount of power input required to raise the temperature from point B to point C in Fig. 7.14 is the amount of heat throughput that was transferred through the heat pipe due to conduction and radiation. Since radiation did not contribute significantly to the total amount of heat transfer, which was estimated to be 0.1 to 0.2 W, the baseline heat transfer measurement due to conduction was determined to be 3.6 watts.

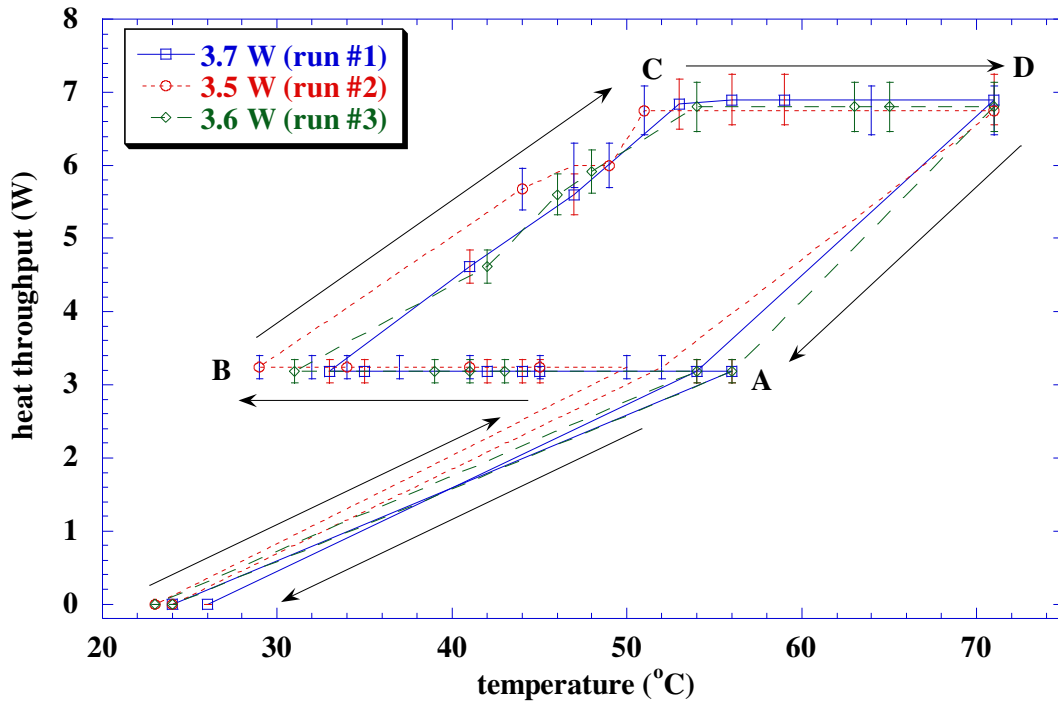


Figure 7.14: Baseline test with no working fluid (conduction only). An average heat transfer rate of 3.6 W was obtained.

The next step was to measure the heat transfer through the heat pipe using the selected working fluids. In this work, the fill ratio, F.R., is defined as the ratio of liquid pool length to the evaporator length. Using pentane with 0 fill ratio, (only conduction), an average of 3.6 W of heat transfer was achieved with the evaporator temperature at 15 °C (Fig. 7.14). Increasing the ratio to 0.5 resulted in an increase of 5.0 watts giving a total of 8.6 W. Further increasing the ratio to 0.7 and 0.9 again showed improved performance to a total of 11.3 and 12.9 W, respectively. However, an increase to a fill ratio of 1.5 reduced the heat transferred to 7.1 W due to flooding. A summary of the results are plotted in Fig. 7.15a-d for pentane and in Fig. 7.16a-d for R-134a.

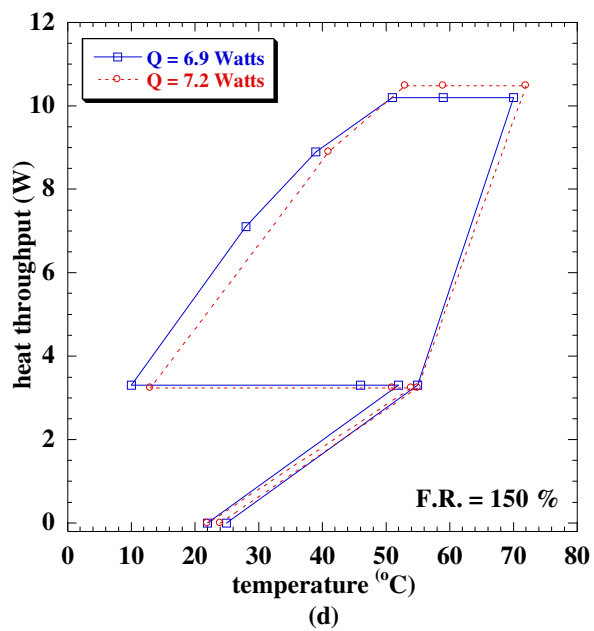
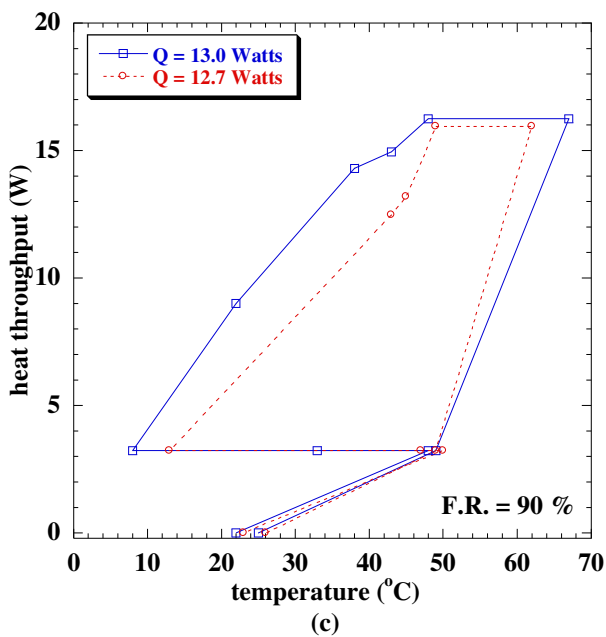
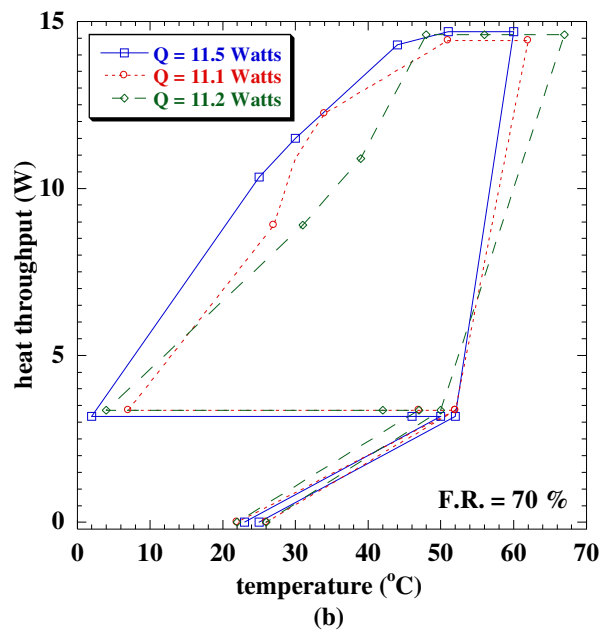
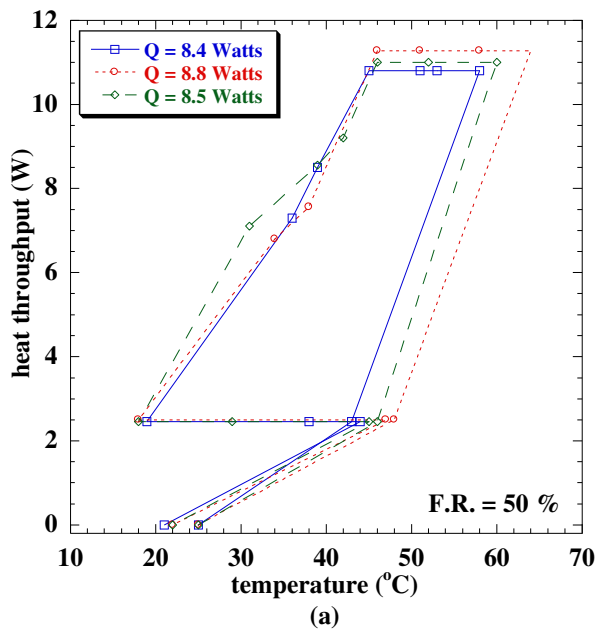


Figure 7.15: Heat throughput using pentane: (a) F.R. = 0.5, $Q = 8.6$ W (b) F.R. = 0.7, $Q = 11.3$ W (c) F.R. = 0.9, $Q = 12.9$ W (d) F.R. = 1.5, $Q = 7.1$ W

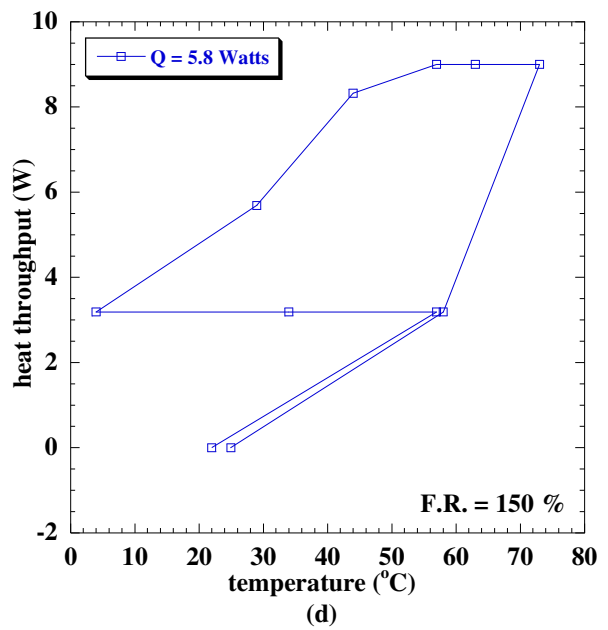
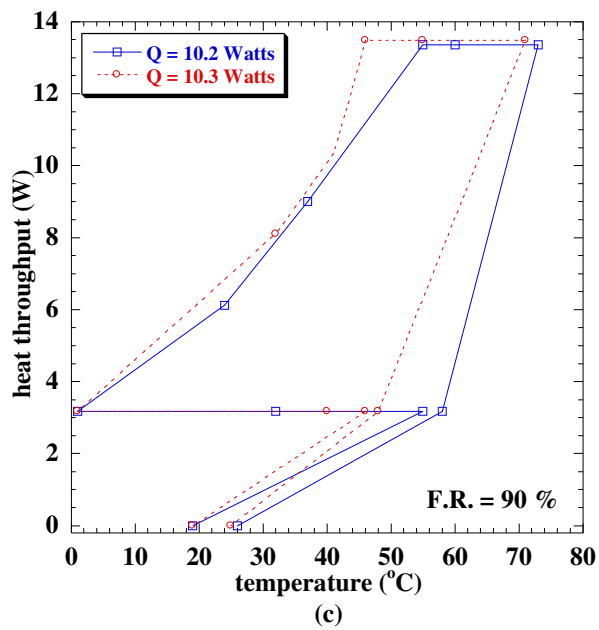
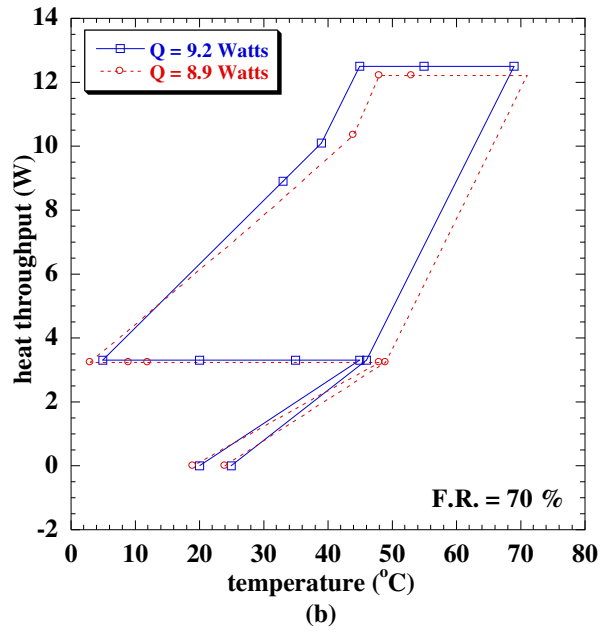
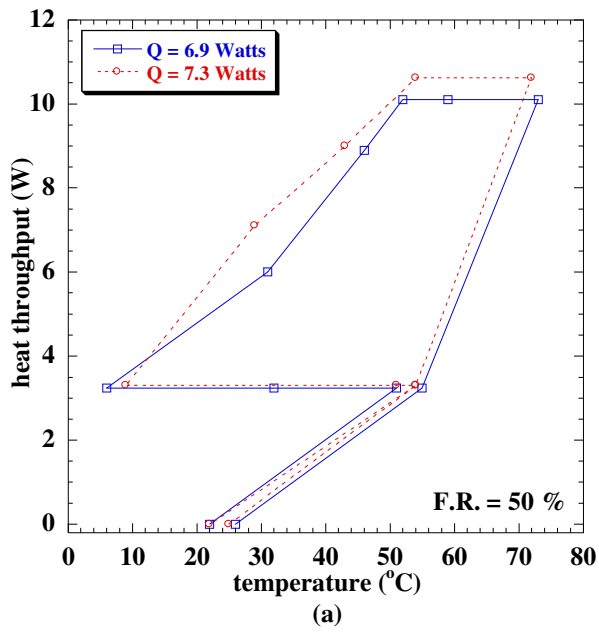


Figure 7.16: Heat throughput using R-134a: (a) F.R. = 0.5, $Q = 7.1$ W (b) F.R. = 0.7, $Q = 9.1$ W
(c) F.R. = 0.9, $Q = 10.2$ W (d) F.R. = 1.5, $Q = 5.8$ W

Using R-134a with 0.5 fill ratio, the average heat throughput was found to be 7.1 W. Increasing the fill ratio to 0.7 and 0.9 increased the heat pipe performance to 9.1 and 10.2 W, respectively. As observed in the results with pentane, increasing the fill ratio to 1.5 decreases the heat throughput to 5.8 W. The results for R-134a are shown in Fig. 7.16. To better compare the aforementioned heat transfer results, the heat throughputs are plotted as a function of fill ratio for both working fluids in Fig. 7.17. Increasing the fill ratio to 1.0 increased the heat transfer for both fluids. However, a further increase to a ratio of 1.5 showed a decrease in heat transfer due to flooding and pressure reduction. Flooding occurs due to a large fill ratio that increases the relative velocity between the vapor and liquid causing high interfacial viscous shear stresses that entrain the condensate form returning back to the evaporator section.

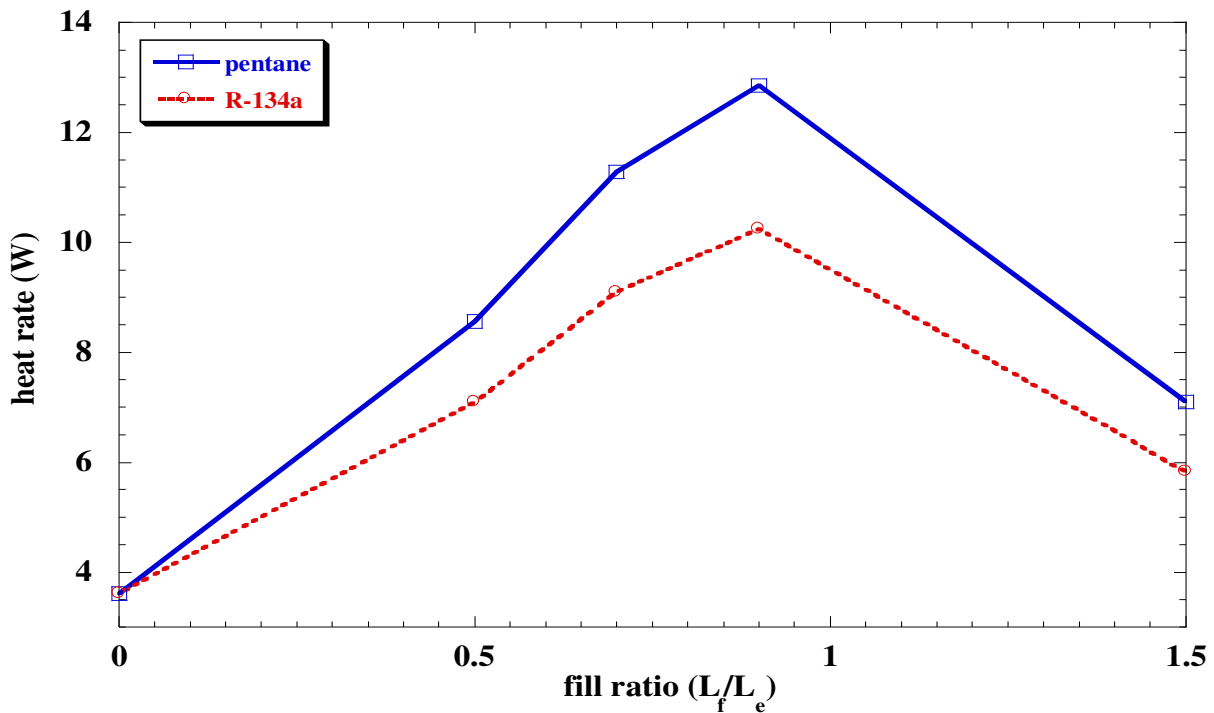


Figure 7.17: Heat transfer rate with fill ratio, with pentane and R-134a as working fluids in the heat pipe. L_f is the liquid pool length and L_e is the length of the evaporator

The average heat transfer rates as a function of the evaporator temperature for both pentane and R-134a are shown in Figs. 7.18 and 7.19. As the evaporator temperature increases, the heat rate increases due to an increase in the temperature gradient.

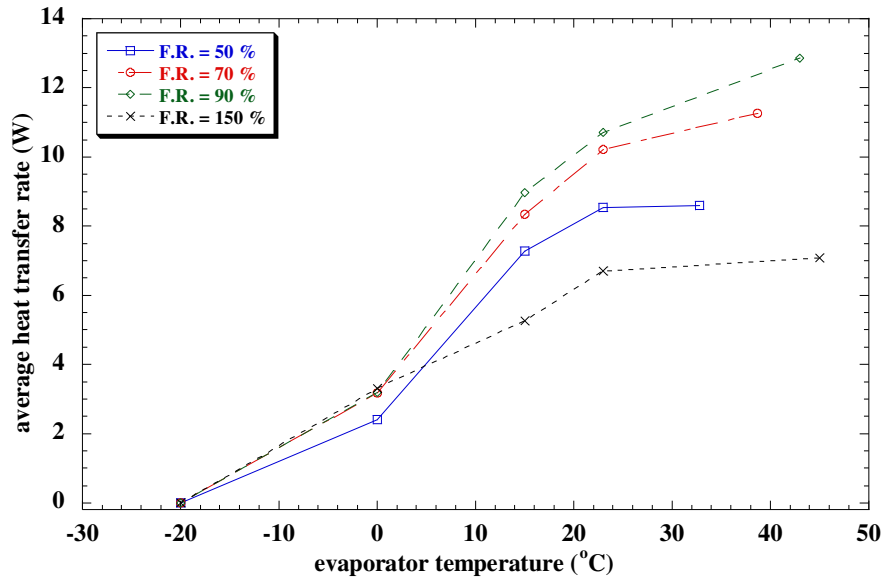


Figure 7.18: Average heat transfer rate using pentane

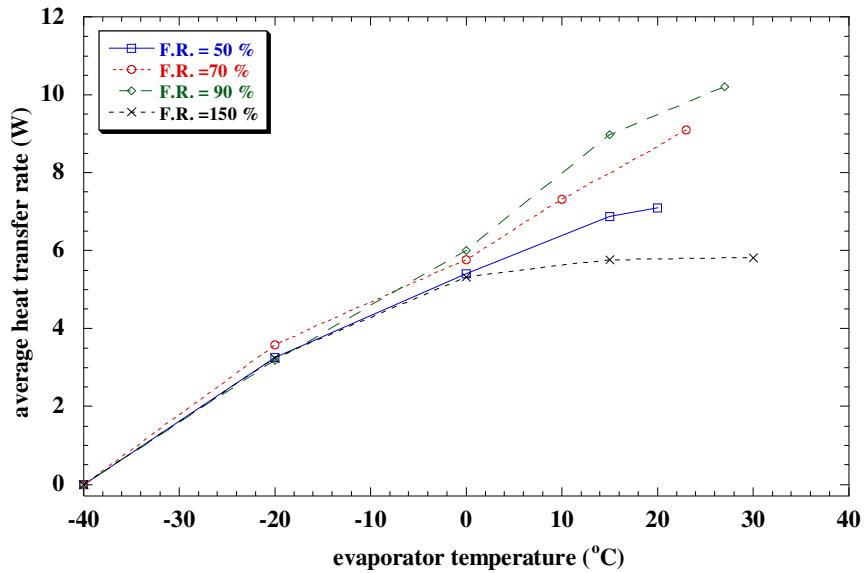


Figure 7.19: Average heat transfer rate using R-134a

CHAPTER EIGHT: CONCLUSIONS AND FUTURE WORK

8.1 Conclusions

For the first time, the working of a variable length, closed two-phase heat pipe based thermal switch incorporating low temperature helical shape memory actuators has been presented to meet NASA's thermal management needs on the surface of the moon and other advanced spaceport applications. Relevant aspects of the design, fabrication and testing methodology for this thermal switch have been presented in detail. Such a switch integrates sensor and actuator functions by using SMAs and does not require external sensors or actuators. The switch can be used to: (i) enhance cryogenic handling methods for liquid and densified cryogenics and zero boil-off systems, (ii) minimize parasitic heat loads for standby cryocoolers, (iii) control heat flow to radiators that have periodic day/night cycles (e.g., moon), and (iv) to control heat transfer between two cryogenic storage tanks with varying heat loads (e.g., oxygen and methane on Mars). A specific objective of this work was to assemble a switch that could passively reject heat loads from a liquid oxygen tank at 92 K while the surrounding space environment varies from 40 K to 400 K during the day and night cycles of the moon. The switch was cycled between the 'on' and 'off' position 70 times without failure which corresponds to a design life of 3 years in the surface of the moon. The desired life of this design is 10 years without any downtime which can easily be met using this switch.

In terms of material selection, addition of Fe to the binary NiTi system suppressed the martensitic transformation below room temperature and narrowed the hysteresis due to the

formation of a stable intermediate R-phase. This new phase offers a new temperature window for applications that require actuation below room temperature. The NiTiFe SMA helical actuators used in this work exhibited favorable and consistent thermo-mechanical properties while providing a reliable passive actuation mechanism. Large stroke during transformation (up to 7 mm) against bias forces (up to 39 N) with minimal open loop axial deformation were obtained. The actuators themselves experienced shear stresses of up to 38 MPa and recovered upwards of 99% of these stresses while cycling between low and high temperatures. Integrating these actuators with a closed variable length two-phase heat pipe produced a thermal switch capable of transferring up to 13 W. The valve for charging the heat pipe facilitated easy introduction of the working fluids and two working fluids were used - pentane and R-134a.

8.2 Future Work and Recommendations

- 1) The NiTiFe helical actuators used in this work transform below room temperature with transformation temperatures ranging between -15 °C and -75 °C. Applications at cryogenic regimes cannot benefit from this alloy; hence the alloy composition has to be modified to even lower temperatures by e.g., adding more iron in the NiTi system. Furthermore, the thermo-mechanical properties of the SMA material can be optimized by heat treatments and hot/cold work.
- 2) A large hysteresis was observed due to the temperature gradient along the length of the spring. This can be avoided by cooling or heating the spring uniformly and not from one end only as it is done in the current design.

- 3) The finite element analysis (FEA) performed in this work used linear elastic isotropic properties for the alloys. It did not consider detwinning in the deformation response. An improved model needs to be developed to capture these contributions during analyses.
- 4) Heat transfer analysis was based on conduction and two-phase flow heat transfer through the heat pipe. For optimum operation, improvement is needed to better control the pipe internal pressure and seal the pipe completely. Leakages were observed at the threaded coupling that connected the base to the pipe. Some other mechanism could be used for rigid connection without welding.
- 5) During the fluid phase change from vapor to condensate, the liquid film is returned to the lower end assisted by gravity. For low gravity environments, a capillary wick structure should be considered to aid the return of the liquid film to the evaporator liquid pool.

Overall, this work has laid the groundwork by demonstrating this unique thermal switch that combines SMA actuators with a variable length heat pipe and functions without complex external sensors or actuators. The novelty stems from the use of a low temperature, low hysteresis NiTiFe alloy as the SMA actuator as well as successfully demonstrating its function in a passive thermal switch by correctly accomplishing the force balance between the bellows, the bias spring and the SMA springs. Aforementioned aspects related to optimizing material behavior (e.g., for use at lower temperatures), heat transfer (by tailoring the mass and pressure of the working fluid inside the heat pipe and introducing a wick if necessary) and minimizing the gradient along the actuators can make this technology ready for practical use.

APPENDIX A: DESIGN CALCULATIONS

A-1 Spring Design Equations and Calculations

Spring design equations:

Spring constant: $k = \frac{d^4 \cdot G}{8 \cdot D^3 \cdot N_a}$

Load: $F = k \cdot y$

Spring index: $C = \frac{D}{d}$

Pitch: $p = \frac{L_f}{N_a + 1}$

Helix angle: $\alpha = \text{atan}\left(\frac{p}{\pi D}\right)$

Spring mass: $M = \rho \cdot L_w \cdot \frac{\pi \cdot d^2}{4}$

Wire length: $L_w = \pi \cdot D \cdot \left(\frac{N_a}{\cos(\alpha)} + N_{ia} \right)$

SMA material properties and spring parameters:

$G_A := 19430\text{MPa}$ shear modulus (austenite phase)

$G_R := 8000\text{MPa}$ shear modulus (R- phase)

$d_{\text{SMA}} := 2.159\text{mm}$ wire diameter

$D_{\text{SMA}} := 15.24\text{mm}$ mean coil diameter

$L_f := 63.5\text{mm}$ free length $N_t := 5$

$y_{\text{SMA}} := 5\text{mm}$ maximum spring deflection $N_{ia} := 1$

Calculations:

Spring index (C) $C := \frac{D_{\text{SMA}}}{d_{\text{SMA}}}$ $C = 6.596$

Number of active coils $N_a := N_t - 1$ $N_a = 3$

Pitch (p) $p := \frac{L_f}{N_a + 1}$ $p = 0.016\text{m}$

Pitch angle (α) $\alpha := \text{atan}\left(\frac{p}{\pi \cdot D_{\text{SMA}}}\right)$ $\alpha = 0.34$

Wire length (L_w) $L_w := \pi \cdot D_{\text{SMA}} \cdot \left(\frac{N_a \cdot \pi}{\cos(\alpha) \cdot 180} + N_{ia}\right)$ $L_w = 0.047\text{m}$

Spring mass (M) $M := \rho \cdot L_w \cdot \frac{\pi \cdot d_{\text{SMA}}^3}{4}$ $M = 1.115 \times 10^{-3}\text{kg}$

Spring constant (K_A and K_R)

$$k_A := 4 \frac{\left(\frac{\cos(\alpha)^2}{G_A \cdot J} + \frac{\sin(\alpha)^2}{E_A \cdot I}\right)^{-1}}{\pi N_a \cdot D_{\text{SMA}}^3 \cdot \sec(\alpha)}$$

$k_A = 4.898 \times 10^3 \frac{\text{kg}}{\text{s}^2}$

$$k_R := 4 \frac{\left(\frac{\cos(\alpha)^2}{G_R \cdot J} + \frac{\sin(\alpha)^2}{E_R \cdot I}\right)^{-1}}{\pi N_a \cdot D_{\text{SMA}}^3 \cdot \sec(\alpha)}$$

$k_R = 1.517 \times 10^3 \frac{\text{kg}}{\text{s}^2}$

Actuation loads (F_A and F_R)

$$F_A := k_A \cdot y_{SMA}$$

$$F_R := k_R \cdot y_{SMA}$$

	0		0		0
	0.0005		3.046		0.785
	0.001		6.092		1.57
	0.0015		9.138		2.356
	0.002		12.184		3.141
	0.0025		15.229		3.926
	0.003		18.275		4.711
	0.0035		21.321		5.497
	0.004		24.367		6.282
	0.0045		27.413		7.067
$y =$	0.005	m	$F_A =$	30.459	N
	0.0055			33.505	
	0.006			36.551	
	0.0065			39.596	
	0.007			42.642	
	0.0075			45.688	
	0.008			48.734	
	0.0085			51.78	
	0.009			54.826	
	0.0095			57.872	
	0.01			60.918	
Deflection increments			Austenite load		R-phase Load

Bias spring material properties and parameters:

$G_b := 68.95\text{GPa}$	shear modulus (bias spring)
$d_b := 2.053\text{mm}$	wire diameter
$D_b := 20.84832\text{mm}$	mean coil diameter
$D_i := 17.399\text{mm}$	inside diameter
$D_o := 21.5036\text{mm}$	outside diameter
$L_{fb} := 69.85\text{mm}$	free length
$y_b := 5\text{mm}$	spring deflection
$N_{tb} := 10$	total coils

Calculations:

Spring index (C)	$C := \frac{D_b}{d_b}$	$C = 10.155$
------------------	------------------------	--------------

Number of active coils	$N_{ab} := N_{tb} - 1$	$N_{ab} = 9$
------------------------	------------------------	--------------

Pitch (p)	$p_b := \frac{L_{fb}}{N_{ab} + 1}$	$p_b = 6.985 \times 10^{-3}\text{m}$
-----------	------------------------------------	--------------------------------------

Spring constant (K_b)	$k_b := \frac{d_b^4 \cdot G_b}{8 \cdot D_b^3 \cdot N_{ab}}$	$k_b = 1.877 \times 10^3 \frac{\text{kg}}{\text{s}^2}$
---------------------------	---	--

Forces (F_A and F_R)	$F_b := k_b \cdot y_b$	$F_b = 9.387\text{N}$
----------------------------	------------------------	-----------------------

SMA shear stress and shear strain:

$$\tau_A = \begin{pmatrix} 0 \\ 9.152 \times 10^6 \\ 1.83 \times 10^7 \\ 2.746 \times 10^7 \\ 3.661 \times 10^7 \\ 4.576 \times 10^7 \\ 5.491 \times 10^7 \\ 6.407 \times 10^7 \\ 7.322 \times 10^7 \\ 8.237 \times 10^7 \\ 9.152 \times 10^7 \\ 1.007 \times 10^8 \\ 1.098 \times 10^8 \\ 1.19 \times 10^8 \\ 1.281 \times 10^8 \\ 1.373 \times 10^8 \\ 1.464 \times 10^8 \\ 1.556 \times 10^8 \\ 1.647 \times 10^8 \\ 1.739 \times 10^8 \\ 1.83 \times 10^8 \end{pmatrix} \text{ Pa} \quad \tau_R = \begin{pmatrix} 0 \\ 3.768 \times 10^6 \\ 7.535 \times 10^6 \\ 1.13 \times 10^7 \\ 1.507 \times 10^7 \\ 1.884 \times 10^7 \\ 2.261 \times 10^7 \\ 2.637 \times 10^7 \\ 3.014 \times 10^7 \\ 3.391 \times 10^7 \\ 3.768 \times 10^7 \\ 4.144 \times 10^7 \\ 4.521 \times 10^7 \\ 4.898 \times 10^7 \\ 5.275 \times 10^7 \\ 5.651 \times 10^7 \\ 6.028 \times 10^7 \\ 6.405 \times 10^7 \\ 6.782 \times 10^7 \\ 7.158 \times 10^7 \\ 7.535 \times 10^7 \end{pmatrix} \text{ Pa} \quad \gamma = \begin{pmatrix} 0 \\ 3.792 \times 10^{-4} \\ 7.584 \times 10^{-4} \\ 1.138 \times 10^{-3} \\ 1.517 \times 10^{-3} \\ 1.896 \times 10^{-3} \\ 2.275 \times 10^{-3} \\ 2.654 \times 10^{-3} \\ 3.034 \times 10^{-3} \\ 3.413 \times 10^{-3} \\ 3.792 \times 10^{-3} \\ 4.171 \times 10^{-3} \\ 4.551 \times 10^{-3} \\ 4.93 \times 10^{-3} \\ 5.309 \times 10^{-3} \\ 5.688 \times 10^{-3} \\ 6.067 \times 10^{-3} \\ 6.447 \times 10^{-3} \\ 6.826 \times 10^{-3} \\ 7.205 \times 10^{-3} \\ 7.584 \times 10^{-3} \end{pmatrix}$$

Austenite shear stress

R-phase shear stress

Total shear strain

A-2 Comparison of SMA Spring Design Equations

Material properties:

Elastic Modulus	Poisson's ratio	Shear Modulus
$E_A := 53\text{GPa}$	$\nu_A := 0.33$	$G_A := 20\text{GPa}$
$E_R := 21\text{GPa}$	$\nu_R := 0.31$	$G_R := 8\text{GPa}$

Geometry:

wire diameter:	$d := 0.085\text{in}$	second polar moment of area: $J := \frac{\pi d^4}{32}$
coil diameter	$D := 0.6\text{in}$	
# of active coils	$N_a := 7$	moment of area: $I := \frac{\pi d^4}{64}$
helix angle	$\alpha := 20\text{deg}$	
		spring index $C := \frac{D}{d}$

Reduced form:

$$\delta_{\text{red}} := \frac{8N_a \cdot D^3}{G_R \cdot d^4}$$

$$\delta_2 := \frac{1}{4} \pi N_a \cdot D^3 \cdot F \cdot \sec(\alpha) \cdot \left(\frac{\cos(\alpha)^2}{G_R \cdot J} + \frac{\sin(\alpha)^2}{E_R \cdot I} \right)$$

Complete form:

$$\delta_3 := \frac{8F \cdot D^3 \cdot N_a}{G_R \cdot d^4} \cdot \left[1 - \frac{3}{16C^2} + \frac{3 + \nu_R}{2(1 + \nu_R)} \cdot \tan(\alpha)^2 \right]$$

1	
1	0
2	1.14·10 ⁻³
3	2.281·10 ⁻³
4	3.421·10 ⁻³
5	4.561·10 ⁻³
6	5.702·10 ⁻³
7	6.842·10 ⁻³
8	7.983·10 ⁻³
9	9.123·10 ⁻³
10	0.01
11	0.011
12	0.013
13	0.014
14	0.015
15	0.016
16	0.017
17	0.018
18	0.019
19	0.021
20	0.022
21	0.023

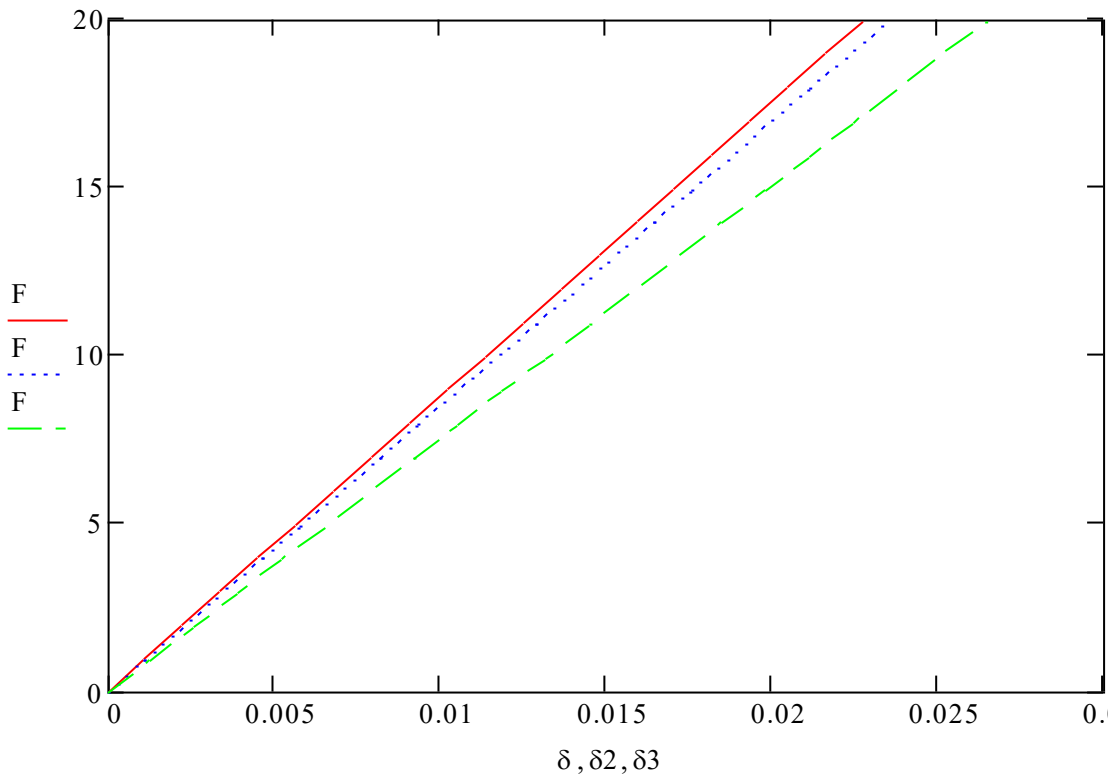
$\delta =$ m

1	
1	0
2	1.18·10 ⁻³
3	2.359·10 ⁻³
4	3.539·10 ⁻³
5	4.719·10 ⁻³
6	5.899·10 ⁻³
7	7.078·10 ⁻³
8	8.258·10 ⁻³
9	9.438·10 ⁻³
10	0.011
11	0.012
12	0.013
13	0.014
14	0.015
15	0.017
16	0.018
17	0.019
18	0.02
19	0.021
20	0.022
21	0.024

$\delta 2 =$ m

1	
1	0
2	1.327·10 ⁻³
3	2.654·10 ⁻³
4	3.981·10 ⁻³
5	5.308·10 ⁻³
6	6.635·10 ⁻³
7	7.962·10 ⁻³
8	9.288·10 ⁻³
9	0.011
10	0.012
11	0.013
12	0.015
13	0.016
14	0.017
15	0.019
16	0.02
17	0.021
18	0.023
19	0.024
20	0.025
21	0.027

$\delta 3 =$ m



A-3 Heat Pipe Internal Stress Analysis Equations

Axial stress

$$\sigma_1 = \frac{P_i \cdot r_i^2 - P_o \cdot r_o^2}{r_o^2 - r_i^2}$$

Hoop stress

$$\sigma_2(r) = \frac{P_i \cdot r_i^2 - P_o \cdot r_o^2}{r_o^2 - r_i^2} - \frac{r_i^2 \cdot r_o^2 \cdot (P_o - P_i)}{r^2 \cdot (r_o^2 - r_i^2)}$$

Radial stress

$$\sigma_3(r) = \frac{P_i \cdot r_i^2 - P_o \cdot r_o^2}{r_o^2 - r_i^2} + \frac{r_i^2 \cdot r_o^2 \cdot (P_o - P_i)}{r^2 \cdot (r_o^2 - r_i^2)}$$

Radial deflection

$$u(r) = \frac{r}{E} \cdot (\sigma_2(r) - \nu \cdot \sigma_3(r) - \nu \cdot \sigma_1)$$

A-4 Heat Transfer Design Equations and Calculations (for R-134a)

R-134a properties

$$T_{\text{sat}} := 256\text{K} \quad \text{saturation temperature}$$

$$P_{\text{sat}} := 0.14989\text{MPa} \quad \text{saturation pressure}$$

Liquid Phase

Vapor Phase:

$$k_l := 0.099753 \frac{\text{W}}{\text{m}\cdot\text{K}}$$

$$k_v := 0.010054 \frac{\text{W}}{\text{m}\cdot\text{K}}$$

thermal conductivity

$$\mu_l := 3.342 \times 10^{-4} \text{Pa}\cdot\text{s}$$

$$\mu_v := 1.0103 \times 10^{-5} \text{Pa}\cdot\text{s}$$

liquid Viscosity

$$\rho_l := 1349.5 \frac{\text{kg}}{\text{m}^3}$$

$$\rho_v := 7.6118 \frac{\text{kg}}{\text{m}^3}$$

liquid Density

$$h_f := 177.3310^3 \frac{\text{J}}{\text{kg}}$$

$$h_g := 388.3110^3 \frac{\text{J}}{\text{kg}}$$

enthalpy

$$C_{p,l} := 1.299210^3 \frac{\text{J}}{\text{kg}\cdot\text{K}}$$

$$C_{p,v} := 0.8263910^3 \frac{\text{J}}{\text{kg}\cdot\text{K}}$$

specific Heat /p

$$C_{v,l} := 0.8584210^3 \frac{\text{J}}{\text{kg}\cdot\text{K}}$$

$$C_{v,v} := 0.7123910^3 \frac{\text{J}}{\text{kg}\cdot\text{K}}$$

specific Heat /v

$$\sigma := 0.014084 \frac{\text{N}}{\text{m}}$$

surface tension

Heat pipe dimensions:

$$d := 25.4\text{mm}$$

heat pipe inner diameter

$$L_c := 25.4\text{mm}$$

condenser length (optimized)

$$L_e := 50.8\text{mm}$$

evaporator length (optimized)

$$A_c := \pi \cdot d \cdot L_c \quad A_c = 2.027 \times 10^{-3} \text{m}^2$$

condenser surface area

$$A_e := \pi \cdot d \cdot L_e \quad A_e = 4.054 \times 10^{-3} \text{m}^2$$

evaporator surface area

Boundary conditions:

$T_e := 260\text{K}$ evaporator temperature (actuators transformation temperature)

$T_c := 250\text{K}$ condenser temperature (average temperature during contact)

Assumptions:

Steady state operation

Minimum fill volume is only that required to maintain the liquid on the walls of the pipe

Saturation temperature:

$$T_{\text{satt}} := \frac{T_e \cdot L_e + T_c \cdot L_c}{L_c + L_e} \quad T_{\text{satt}} = 256.667\text{K}$$

Average heat transfer coefficient:

$$h_e := \frac{4}{3} \cdot \left[\frac{\rho_l^2 \cdot k_l^3 \cdot g \cdot h_{fg}}{4 \cdot \mu_l \cdot (T_e - T_{\text{satt}}) \cdot L_e} \right]^{\frac{1}{4}} \quad h_c := \frac{4}{3} \cdot \left[\frac{\rho_l^2 \cdot k_l^3 \cdot g \cdot h_{fg}}{4 \cdot \mu_l \cdot (T_{\text{satt}} - T_c) \cdot L_c} \right]^{\frac{1}{4}}$$

Under steady state conditions:

$$Q_c = Q_e$$

$$h_e \cdot L_e \cdot (T_e - T_{\text{satt}}) = 455.198 \frac{\text{m} \cdot \text{kg}}{\text{s}^3}$$

$$h_c \cdot L_c \cdot (T_{\text{satt}} - T_c) = 455.198 \frac{\text{m} \cdot \text{kg}}{\text{s}^3}$$

$$Q := \pi \cdot d \cdot L_c \cdot h_c \cdot (T_{\text{satt}} - T_c)$$

$$Q = 13.1\text{W}$$

$$Q := \frac{4 \cdot \pi}{3} \cdot d \cdot \left[\left(\frac{\rho_l^2 \cdot g \cdot h_{fg} \cdot k_l^3}{4 \cdot \mu_l} \right) \cdot \left(\frac{L_c \cdot L_e}{L_c + L_e} \right)^3 \right] \cdot (T_e - T_c)$$

$$Q = 12.19\text{W}$$

Second approach using mass flow rate:

$$\delta_c := \left[\frac{4 \cdot k_l \cdot \mu_l \cdot (T_{\text{sat}} - T_c) \cdot L_c}{\rho_l^2 \cdot g \cdot h_{\text{fg}}} \right]^{\frac{1}{4}}$$

liquid film at condenser

$$m_{\text{dot}} := \frac{\pi \cdot d \cdot \rho_l^2 \cdot g \cdot \delta_c^3}{3 \cdot \mu_l}$$

$$m_{\text{dot}} = 1.591 \times 10^{-4} \frac{\text{kg}}{\text{s}} \quad \text{mass flow rate}$$

$$Q_c := m_{\text{dot}} \cdot h_{\text{fg}}$$

$$Q_c = 13.29 \quad \text{condenser heat rate}$$

Third approach using Equations 4.5 and 4.10:

• **Evaporator side:**

Heat rate and heat flux

$$Q := 8\text{W} \quad \text{starting heat rate}$$

$$q_e := \frac{Q}{A_e}$$

Evaluating heat transfer coefficient

$$h_{\text{fg}} := h_g - h_f \quad P_a := 101.325\text{kPa}$$

$$\text{Heat transfer coefficient} \quad h_e := 0.32 \left(\frac{\rho_l^{0.65} \cdot k_l^{0.3} \cdot c_{p,l}^{0.7} \cdot g^{0.2} \cdot q_e^{0.4}}{\rho_v^{0.25} \cdot h_{\text{fg}}^{0.4} \cdot \mu_l^{0.1}} \right) \cdot \left(\frac{P_e}{P_a} \right)^{0.3}$$

$$\Delta T_e := \frac{q_e}{h_e} \quad \Delta T_e = 2.019 \text{ K}$$

$$T_{\text{sat}} := T_e - \Delta T_e \quad T_{\text{sat}} = 257.981 \text{ K}$$

$$Q_e := \left[0.32 \cdot \left(\frac{\rho_l^{0.65} \cdot k_l^{0.3} \cdot c_{p,l}^{0.7} \cdot g^{0.2}}{\rho_v^{0.25} \cdot h_{fg}^{0.4} \cdot \mu_l^{0.1}} \right) \cdot \left(\frac{P_e}{P_a} \right)^{0.23} \cdot A_e \cdot (T_e - T_{\text{sat}}) \right]^{\frac{5}{3}} \quad Q_e = 7.497 \text{ W}$$

- **Condenser side:**

$$T_c := 208 \text{ K}$$

$$P_c := 0.011263 \text{ MPa}$$

Liquid and vapor phase properties:

$$\begin{aligned} \rho_{lc} &:= 1488.6 \frac{\text{kg}}{\text{m}^3} & h_{fc} &:= 117.08 \cdot 10^3 \frac{\text{J}}{\text{kg}} \\ \rho_{vc} &:= 0.67075 \frac{\text{kg}}{\text{m}^3} & h_{gc} &:= 358.06 \cdot 10^3 \frac{\text{J}}{\text{kg}} \\ \mu_{lc} &:= 0.00073101 \text{ Pa} \cdot \text{s} & h_{fg,c} &:= h_{gc} - h_{fc} \\ k_{lc} &:= 0.12343 \frac{\text{W}}{\text{m} \cdot \text{K}} \end{aligned}$$

Heat transfer coefficient

$$\begin{aligned} \text{Re}_l &:= \frac{Q}{\pi \cdot d \cdot \mu_{lc} \cdot h_{fg,c}} & v_{lc} &:= \frac{\mu_{lc}}{\rho_{lc}} & q_c &:= \frac{Q}{A_c} \\ \text{Nu} &:= 0.925 \cdot \text{Re}_l \end{aligned}$$

$$h_c := \text{Nu} \cdot k_{lc} \cdot \left[\frac{v_{lc}^2}{g} \cdot \left(\frac{\rho_{lc}}{\rho_{lc} - \rho_{vc}} \right) \right]^{\frac{-1}{3}}$$

$$\Delta T_c := \frac{q_l}{h_c} \quad \Delta T_c = 1.767 \text{ K}$$

$$T_{\text{satt}} := T_c + \Delta T_c \quad T_{\text{satt}} = 209.767 \text{ K}$$

$$Q_c := h_c \cdot A_c \cdot (T_{\text{satt}} - T_c)$$

$$Q_{\text{ev}} := 0.943 \cdot \left[\frac{g \cdot \rho_{lc} \cdot (\rho_{lc} - \rho_{vc}) \cdot k_l^3 \cdot h_{fg,c}}{\mu_{lc} \cdot L_c} \right]^{\frac{1}{4}} \cdot A_c \cdot (T_{\text{satt}} - T_c)^{\frac{3}{4}}$$

$$Q_c = 7.709 \text{ W}$$

Heat losses

$$Q_{\text{loss}} := Q_c - Q_e$$

$$Q_{\text{loss}} = 0.212 \text{ W}$$

A-5 Heat Transfer Design Equations and Calculations (for Pentane)

- **Evaporator end:**

Boundary conditions

$$T_e := 260\text{K} \quad \dots\dots\dots\text{Evaporator Temperature}$$

$$P_e := 0.012960\text{MPa} \quad \dots\dots\dots\text{Evaporator Pressure}$$

Liquid and vapor phase properties

$$\rho_l := 657.14 \frac{\text{kg}}{\text{m}^3} \quad \text{liquid density}$$

$$\rho_v := 0.43699 \frac{\text{kg}}{\text{m}^3} \quad \text{vapor density}$$

$$\mu_l := 0.00030967\text{Pa}\cdot\text{s} \quad \text{viscosity}$$

$$h_f := -111.24 \cdot 10^3 \frac{\text{J}}{\text{kg}} \quad \text{enthalpy liquid}$$

$$h_g := 282.86 \cdot 10^3 \frac{\text{J}}{\text{kg}} \quad \text{enthalpy vapor}$$

$$k_l := 0.12649 \frac{\text{W}}{\text{m}\cdot\text{K}} \quad \text{thermal conductivity}$$

$$c_{p,l} := 2.1616 \cdot 10^3 \frac{\text{J}}{\text{kg}\cdot\text{K}} \quad \text{specific Heat at constant pressure}$$

Heat pipe dimensions

$$d := 25.4\text{mm} \quad \text{pipe inner diameter}$$

$$L_c := 25.4\text{mm} \quad \text{condenser length}$$

$$L_e := 50.80\text{mm} \quad \text{evaporator length}$$

$$A_c := \pi \cdot d \cdot L_c \quad A_c = 2.027 \times 10^{-3} \text{m}^2 \quad \text{condenser area}$$

$$A_e := \pi \cdot d \cdot L_e \quad A_e = 4.054 \times 10^{-3} \text{m}^2 \quad \text{evaporator area}$$

Heat rate and heat flux

$$Q := 8\text{W}$$

$$q_e := \frac{Q}{A_e}$$

Heat transfer coefficient

$$h_{fg} := h_g - h_f \quad P_a := 101.325\text{kPa}$$

$$\text{Heat transfer coefficient} \quad h_e := 0.32 \left(\frac{\rho_l^{0.65} \cdot k_l^{0.3} \cdot c_{p,l}^{0.7} \cdot g^{0.2} \cdot q_e^{0.4}}{\rho_v^{0.25} \cdot h_{fg}^{0.4} \cdot \mu_l^{0.1}} \right) \cdot \left(\frac{P_e}{P_a} \right)^{0.3}$$

$$\Delta T_e := \frac{q_e}{h_e} \quad \Delta T_e = 2.771\text{K}$$

$$T_{\text{sat}} := T_e - \Delta T_e \quad T_{\text{sat}} = 257.229\text{K}$$

$$Q_e := \left[0.32 \cdot \left(\frac{\rho_l^{0.65} \cdot k_l^{0.3} \cdot c_{p,l}^{0.7} \cdot g^{0.2}}{\rho_v^{0.25} \cdot h_{fg}^{0.4} \cdot \mu_l^{0.1}} \right) \cdot \left(\frac{P_e}{P_a} \right)^{0.23} \cdot A_e^{\frac{5}{3}} \cdot (T_e - T_{\text{sat}}) \right]^{\frac{3}{5}}$$

$$Q_e = 10.169\text{W}$$

- **Condenser end:**

Boundary condition

$$T_c := 208\text{K}$$

$$P_c := 0.011263\text{MPa}$$

Liquid and vapor phase properties:

$$\rho_{lc} := 1488.6 \frac{\text{kg}}{\text{m}^3} \quad h_{fc} := 117.08 \cdot 10^3 \frac{\text{J}}{\text{kg}}$$

$$\rho_{vc} := 0.67075 \frac{\text{kg}}{\text{m}^3} \quad h_{gc} := 358.06 \cdot 10^3 \frac{\text{J}}{\text{kg}}$$

$$\mu_{lc} := 0.00073101\text{Pa}\cdot\text{s} \quad h_{fg,c} := h_{gc} - h_{fc}$$

$$k_{lc} := 0.12343 \frac{\text{W}}{\text{m}\cdot\text{K}}$$

Evaluating the heat transfer coefficient

$$Re_l := \frac{Q}{\pi \cdot d \cdot \mu_{lc} \cdot h_{fg,c}} \quad v_{lc} := \frac{\mu_{lc}}{\rho_{lc}} \quad q_c := \frac{Q}{A_c}$$

$$Nu := 0.925 \cdot Re_l \quad \text{Nusselt number}$$

$$h_c := Nu \cdot k_{lc} \cdot \left[\frac{v_{lc}^2}{g} \cdot \left(\frac{\rho_{lc}}{\rho_{lc} - \rho_{vc}} \right) \right]^{\frac{-1}{3}}$$

$$\Delta T_c := \frac{q_c}{h_c} \quad \Delta T_c = 1.767 \text{ K}$$

$$T_{\text{satt}} := T_c + \Delta T_c \quad T_{\text{satt}} = 209.767 \text{ K}$$

$$Q_c := h_c \cdot A_c \cdot (T_{\text{satt}} - T_c)$$

$$Q_{\text{conv}} := 0.943 \cdot \left[\frac{g \cdot \rho_{\text{lc}} \cdot (\rho_{\text{lc}} - \rho_{\text{vc}}) \cdot k_{\text{l}}^3 \cdot h_{\text{fg,c}}}{\mu_{\text{lc}} \cdot L_c} \right]^{\frac{1}{4}} \cdot A_c \cdot (T_{\text{satt}} - T_c)^{\frac{3}{4}}$$

$$Q_c = 14.314 \text{ W}$$

Heat losses

$$Q_{\text{loss}} := Q_c - Q_e$$

$$Q_{\text{loss}} = 4.145 \text{ W}$$

A-6 Liquid Pool Calculations (with pentane): Film Thickness Calculation

Pentane properties

$T_{\text{sat}} := 256\text{K}$	saturation temperature
$P_{\text{sat}} := 0.010523\text{MPa}$	saturation pressure
$P_a := 101.325\text{kPa}$	atmospheric pressure

Liquid phase at 256 K

$$k_l := 0.12815 \frac{\text{W}}{\text{m}\cdot\text{K}}$$

$$\mu_l := 0.00032274\text{Pa}\cdot\text{s}$$

$$\rho_l := 660.82 \frac{\text{kg}}{\text{m}^3}$$

$$h_f := -119.87 \cdot 10^3 \frac{\text{J}}{\text{kg}}$$

$$C_{p,l} := 2.1479 \cdot 10^3 \frac{\text{J}}{\text{kg}\cdot\text{K}}$$

$$C_{v,l} := 1.602 \cdot 10^3 \frac{\text{J}}{\text{kg}\cdot\text{K}}$$

$$\sigma := 0.020141 \frac{\text{N}}{\text{m}} \quad \text{surface Tension}$$

Vapor phase at 256 K

$$k_v := 0.010654 \frac{\text{W}}{\text{m}\cdot\text{K}} \quad \text{thermal conductivity}$$

$$\mu_v := 5.88 \times 10^{-6} \frac{\text{Pa}}{\text{s}} \quad \text{viscosity}$$

$$\rho_v := 0.35982 \frac{\text{kg}}{\text{m}^3} \quad \text{density}$$

$$h_g := 277.02 \cdot 10^3 \frac{\text{J}}{\text{kg}} \quad \text{enthalpy}$$

$$C_{p,v} := 1.5043 \cdot 10^3 \frac{\text{J}}{\text{kg}\cdot\text{K}} \quad \text{specific heat/p}$$

$$C_{v,v} := 1.3835 \cdot 10^3 \frac{\text{J}}{\text{kg}\cdot\text{K}} \quad \text{specific heat/v}$$

Boundary conditions:

$$T_e := 260\text{K} \quad \text{evaporator Temperature}$$

$$T_c := 250\text{K} \quad \text{condenser Temperature}$$

$$T_{\text{sat}} := 257.229\text{K} \quad P_e := 0.11644\text{MPa}$$

$$\delta_x = \left[\frac{4 \cdot k \cdot \mu_l \cdot x \cdot (T_{\text{sat}} - T_x)}{h_{\text{fg}} \cdot \rho_l \cdot (\rho_l - \rho_v) \cdot g} \right]^{0.25}$$

liquid film thickness at any section

$$\delta_c = \left[\frac{4 \cdot k \cdot \mu_l \cdot L_c \cdot (T_{\text{sat}} - T_c)}{h_{\text{fg}} \cdot \rho_l \cdot (\rho_l - \rho_v) \cdot g} \right]^{0.25}$$

liquid film thickness at condenser section

$$\delta_e = \left[\frac{4 \cdot k \cdot \mu_l \cdot L_f \cdot (T_f - T_{\text{sat}})}{h_{\text{fg}} \cdot \rho_l \cdot (\rho_l - \rho_v) \cdot g} \right]^{0.25}$$

liquid film thickness at evaporator section

Film thickness at the condenser

$$\delta_c := \left[\frac{4 \cdot k_l \cdot \mu_l \cdot L_c \cdot (T_{\text{sat}} - T_c)}{h_{\text{fg}} \cdot \rho_l \cdot (\rho_l - \rho_v) \cdot g} \right]^{0.25}$$

$\delta_c = 7.733 \times 10^{-5} \text{ m}$

Film length at the evaporator section (T_f is the average temperature)

$$T_f := \frac{T_e + T_{\text{sat}}}{2} \quad T_f = 258.615 \text{ K}$$

$$L_f := \left(\frac{3 \cdot Q_e}{\pi d} \right)^{\frac{4}{3}} \cdot \left(\frac{\mu_l}{\rho_l^2 \cdot h_{\text{fg}} \cdot g} \right)^{\frac{1}{3}} \cdot \left[\frac{1}{4 \cdot k_l \cdot (T_f - T_{\text{sat}})} \right]$$

$L_f = 0.016 \text{ m}$

Film thickness at the evaporator

$$\delta_e := \left[\frac{4 \cdot k_l \cdot \mu_l \cdot L_f \cdot (T_f - T_{\text{sat}})}{h_{\text{fg}} \cdot \rho_l \cdot (\rho_l - \rho_v) \cdot g} \right]^{0.25}$$

$\delta_e = 3.852 \times 10^{-5} \text{ m}$

Mass flow rate

$$\dot{m}_{\text{dot}} := \frac{\pi \cdot d \cdot \rho_l (\rho_l - \rho_v) \cdot g \cdot \delta_x^3}{3 \cdot \mu_l}$$

$$\dot{m}_{\text{dot_Lc}} := \frac{\pi \cdot d \cdot \rho_l (\rho_l - \rho_v) \cdot g \cdot \delta_c^3}{3 \cdot \mu_l}$$

$$\dot{m}_{\text{dot_Lc}} = 1.631 \times 10^{-4} \frac{\text{kg}}{\text{s}}$$

$$\dot{m}_{\text{dot_Lf}} := \frac{\pi \cdot d \cdot \rho_l (\rho_l - \rho_v) \cdot g \cdot \delta_e^3}{3 \cdot \mu_l}$$

$$\dot{m}_{\text{dot_Lf}} = 1.806 \times 10^{-4} \frac{\text{kg}}{\text{s}}$$

In terms of heat transfer rate with $Q_c = Q_e$

$$\dot{m}_{\text{dot_Lc}} = \dot{m}_{\text{dot_Lf}} \quad \text{within 8\% error}$$

$$\dot{m}_{\text{dot_Lc}}(Q_c) := \frac{Q_c}{h_{fg}} \quad \dot{m}_{\text{dot_Lf}}(Q_e) := \frac{Q_e}{h_{fg}}$$

Knowing the heat transfer rate at both section, the mass flow rate can also be found

Fin Effect:

Fin effect conduction (evaporator)

$$k_{\text{copper}} := 406 \frac{\text{W}}{\text{m}\cdot\text{K}}$$

$$T_{\text{e.s_measured}} := 259\text{K}$$

$$\Delta T_{\text{e}} := \sqrt{(T_{\text{e}} - T_{\text{e.s_measured}})^2}$$

$$Q_{\text{f.e}} := \frac{A_{\text{e}}}{L_{\text{e}}} \cdot k_{\text{copper}} \cdot (\Delta T_{\text{e}})$$

$$Q_{\text{f.e}} = 1.62 \text{ W}$$

Fin effect conduction (condenser)

$$T_{\text{c.s_measured}} := 251.2\text{K}$$

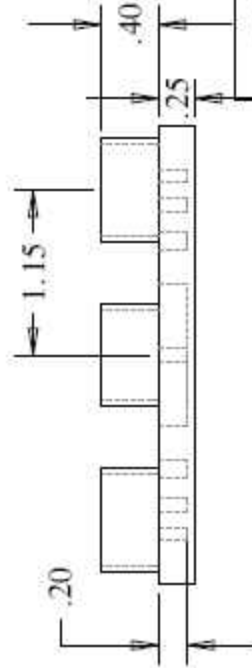
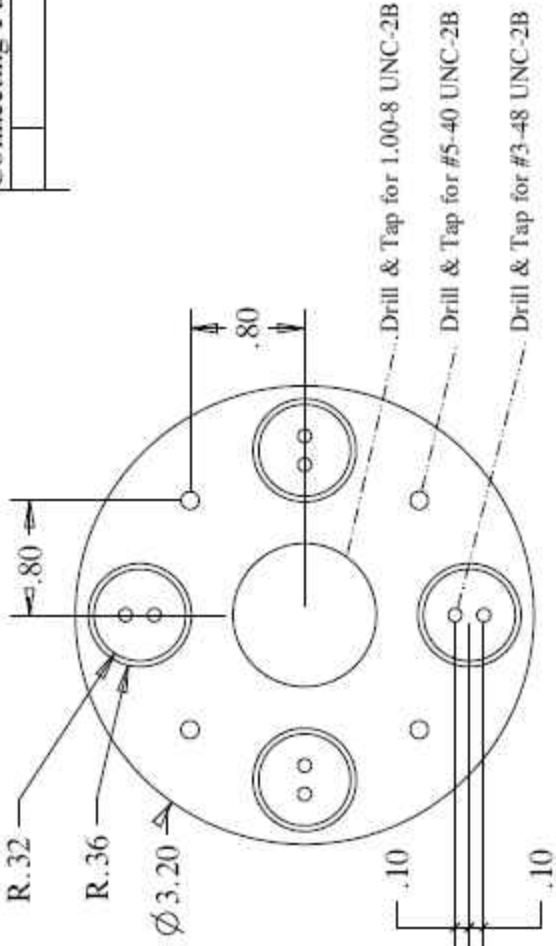
$$\Delta T_{\text{c}} := \sqrt{(T_{\text{c}} - T_{\text{c.s_measured}})^2}$$

$$Q_{\text{f.c}} := \frac{A_{\text{e}}}{L_{\text{e}}} \cdot k_{\text{copper}} \cdot (\Delta T_{\text{c}})$$

$$Q_{\text{f.c}} = 2.981 \text{ W}$$

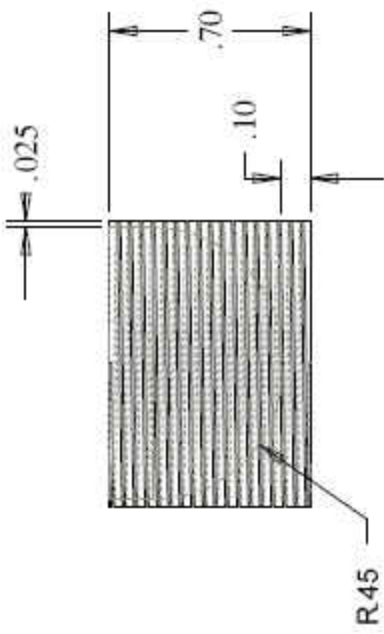
APPENDIX B: DESIGN DRAWINGS

Connecting Parts: Springs, Rods, Coupler & Condenser

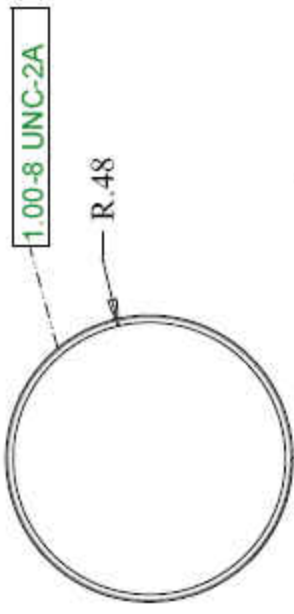


Copper Base Plate		Material: Copper	
Scale 1:1		Count: 1	
Tolerances +/- 0.005		Units: inches	Sheet 1 of 1
		Prepared by: O.B.	

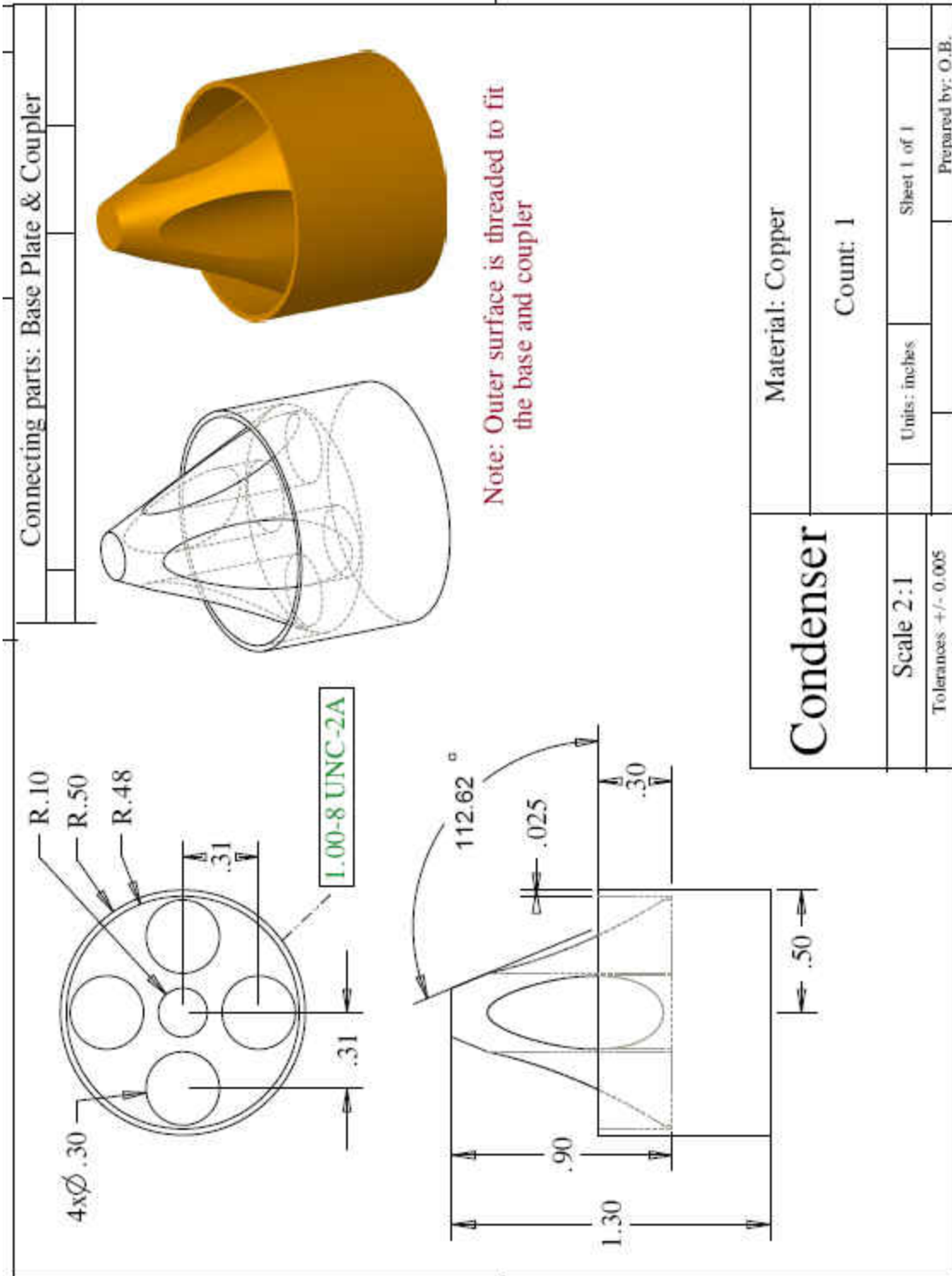
Connecting Parts: Base plate & Coupler

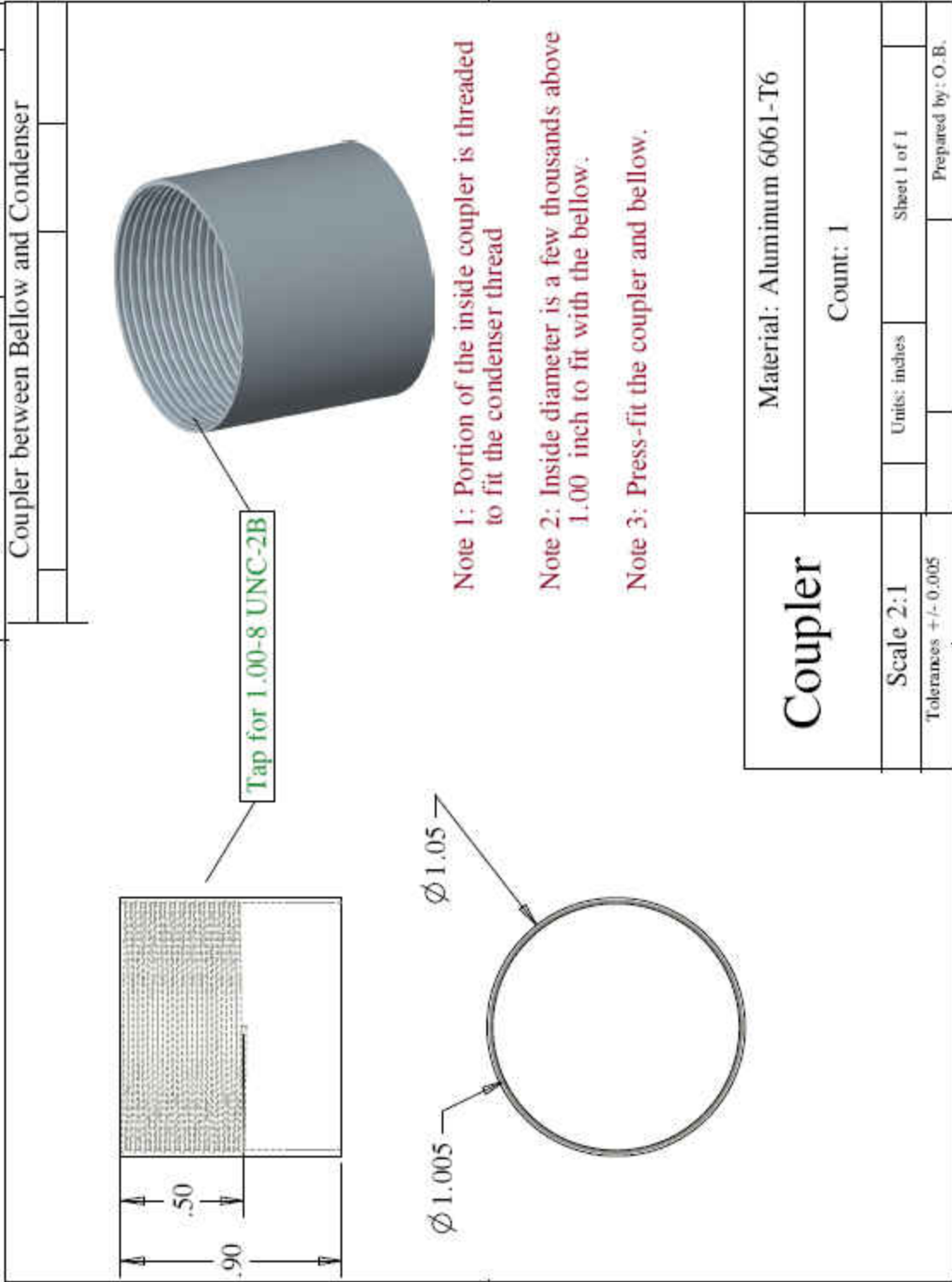


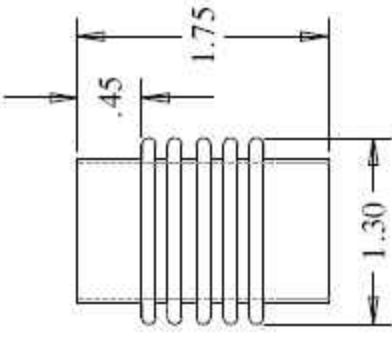


Note: The outer surface is threaded to fit the base plate and coupler.
: the inside has a spherical shape.

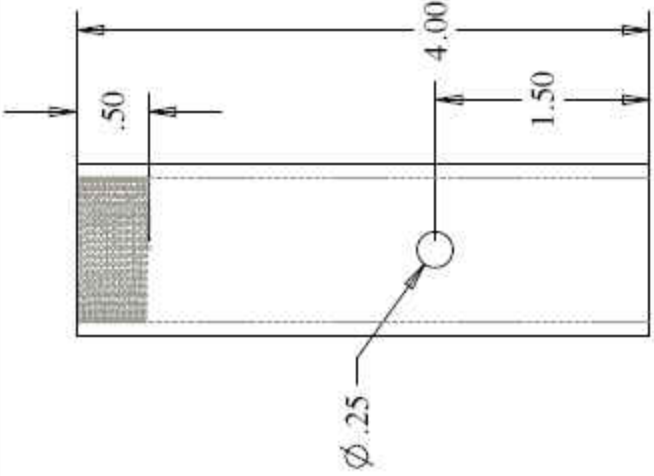
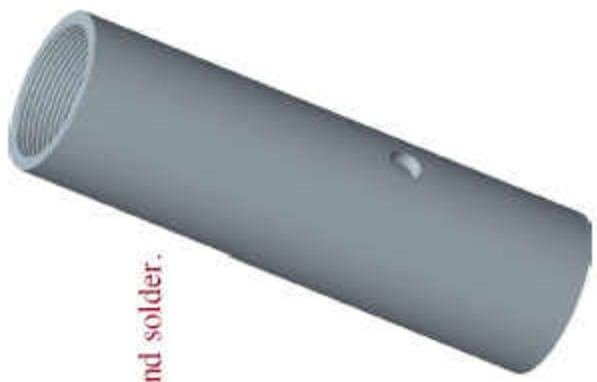


Condenser		Material: Copper	
Scale 2:1		Count: 1	
Tolerances +/- 0.005		Units: inches	Sheet 1 of 1
		Prepared by: O.B.	

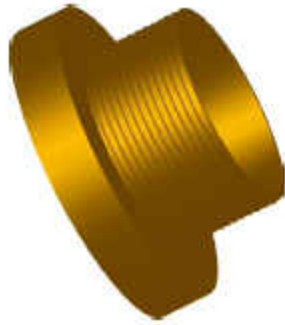
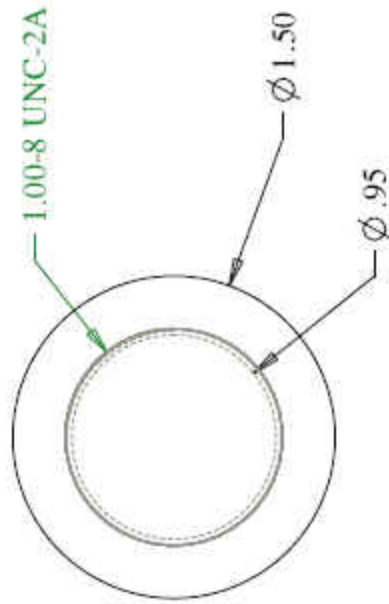




Bellow goes between pipe and coupler.				
		<p>Bellow specs.: Stiffness: $k = 16000 \text{ N/m}$ $k = 9.12 \text{ lbf/in}$</p> <p>Cuff Length: $L = 0.45 \text{ in}$ OD = 1.30 in ID = 1.00 in</p>		
	<p>Bellow</p> <p>Material: Aluminum 6061</p> <p>Count: 1</p>			
<p>Scale 1:1</p> <p>Tolerances ± 0.005</p>	<p>Units: inches</p>	<p>Sheet 1 of 1</p>		<p>Prepared by: O.B.</p>

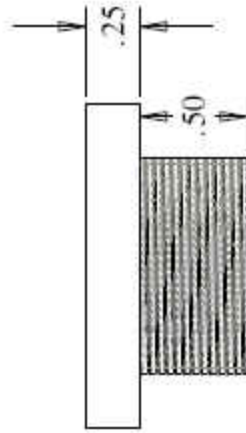
Heat Pipe: Smooth interior finish	
 <p style="text-align: center; margin-top: 20px;"> Drill & Tap for 1.00-8 UNC-2B </p>	 <p style="margin-top: 20px;"> Option 1: thread per code to go with the evaporator. Option 2: No threads, press-fit and solder. </p>
<h1 style="margin: 0;">Pipe</h1>	
Material: Aluminum 6061	
Count: 1	
Scale 1:1	Units: inches
Sheet 1 of 1	
Tolerances +/- 0.005	
Prepared by: O.B.	

Evaporator to fit on top of the heat pipe



Option 1: Thread to fit the end of heat pipe with the specified code.

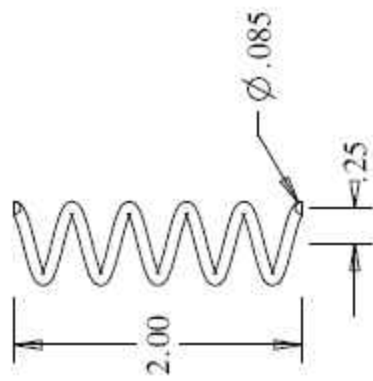
Option 2: No threading, press-fit and solder.



Evaporator		Material: Copper	
Scale 1.5:1		Count: 1	
Tolerances +/- 0.005		Units: inches	Sheet 1 of 1
		Prepared by: O.B.	



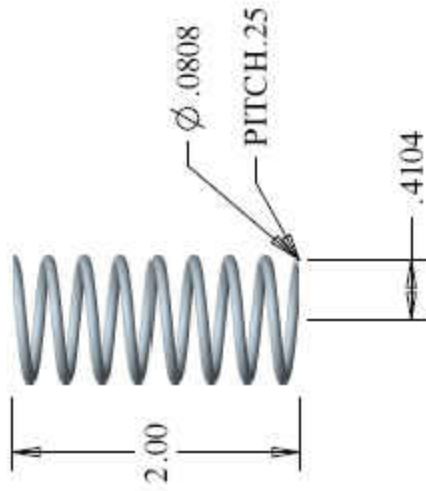
Spring Info:
 Plain Ground Ends
 Wire Diameter: 0.085 in
 Mean Diameter: 0.50 in
 Pitch: 0.5 in
 Active coils: 3
 total coils: 4



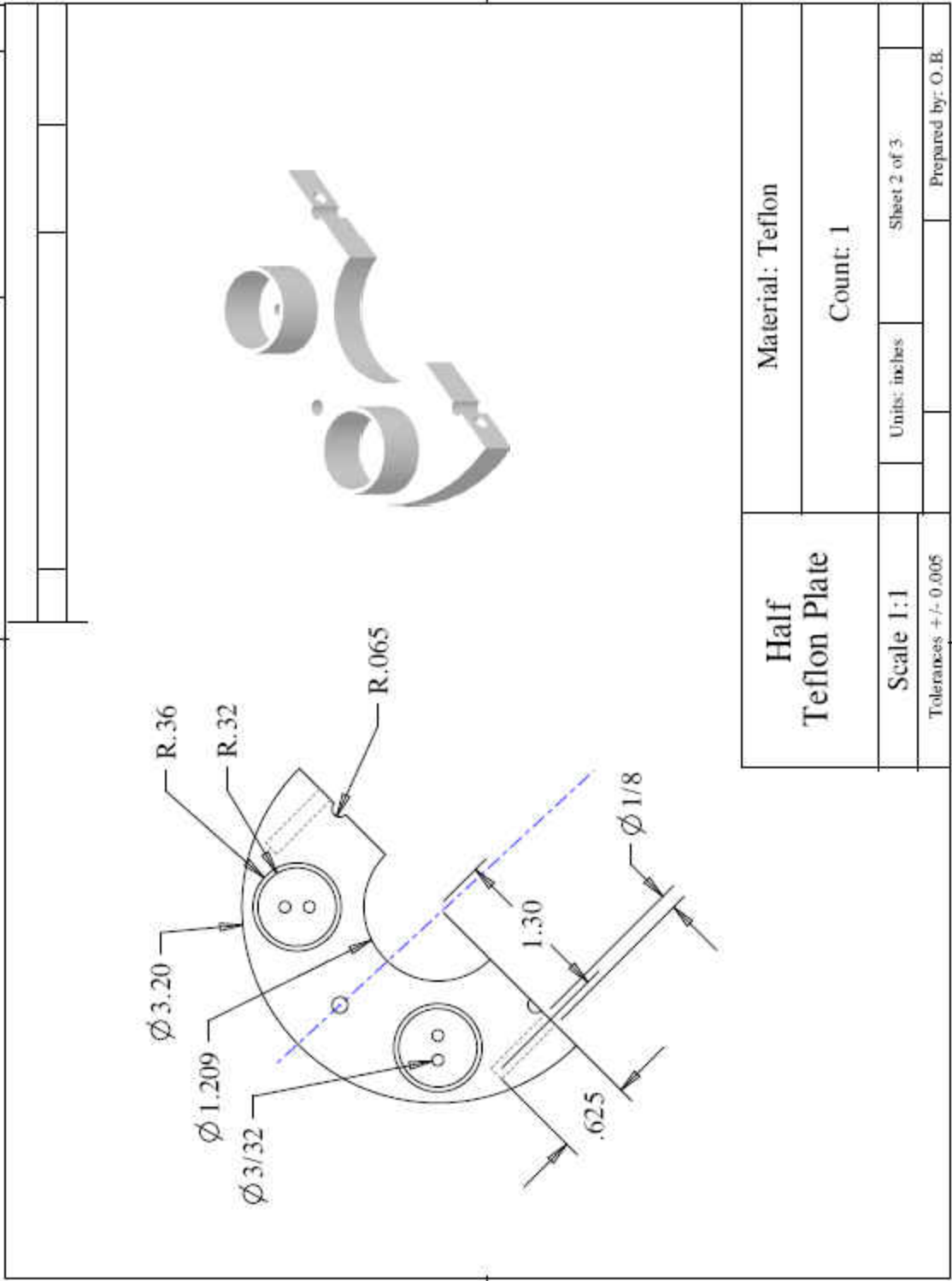
<h1>SMA Spring</h1>	Material: NiTiFe	
	Count: 4	
Scale: 1:1	Units: inches	Sheet 1 of 1
Tolerances: +/- 0.005		Prepared by: O.B.



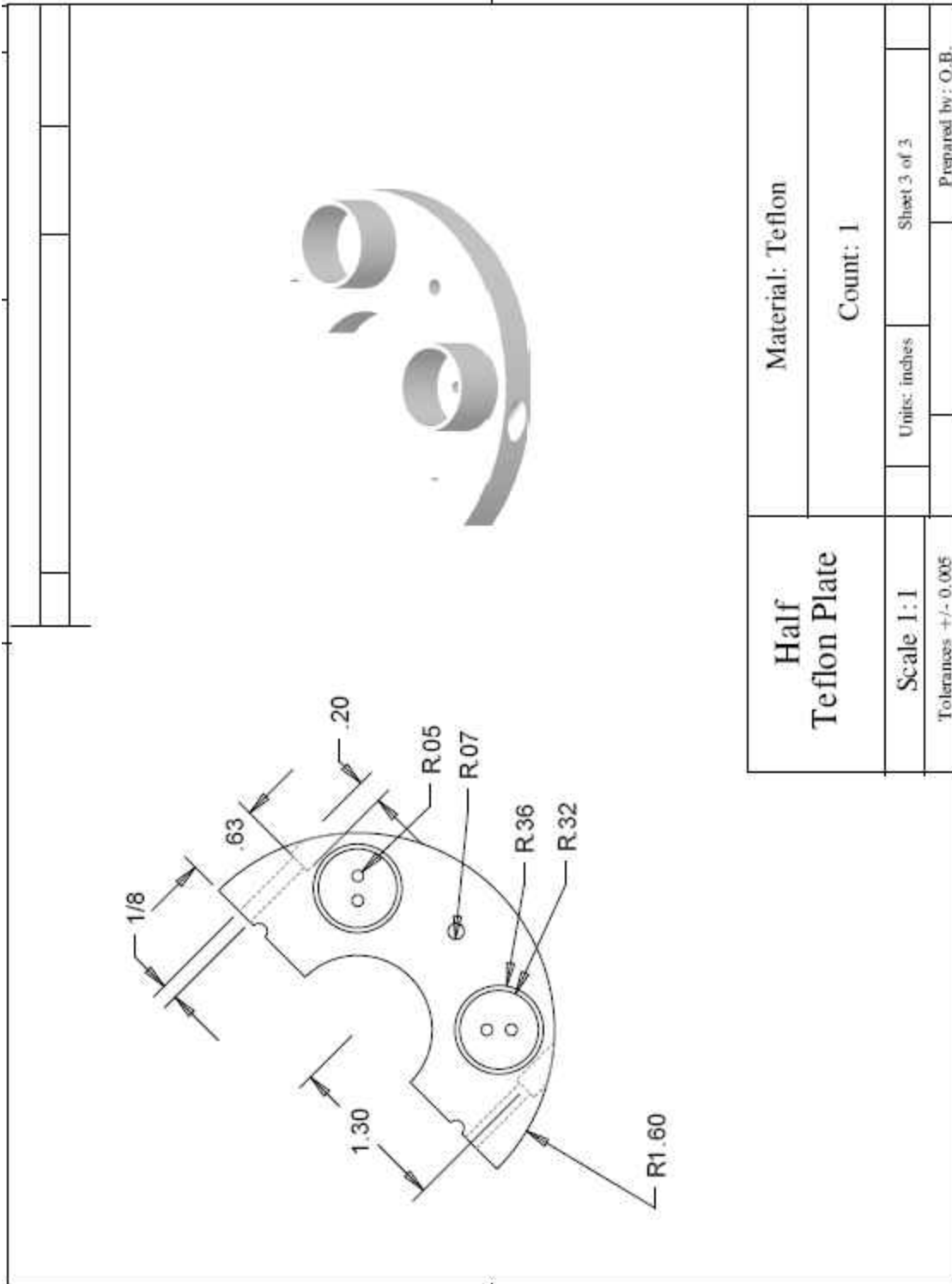
Spring Info:
 Plain Ground Ends
 Wire Diameter: AWG 12 (0.0808 in)
 Mean Diameter: 0.8208 in
 Pitch: 0.222 in
 Active coils: 8
 total coils: 9
 Stiffness: $k = 14.829 \text{ lbf/in}$

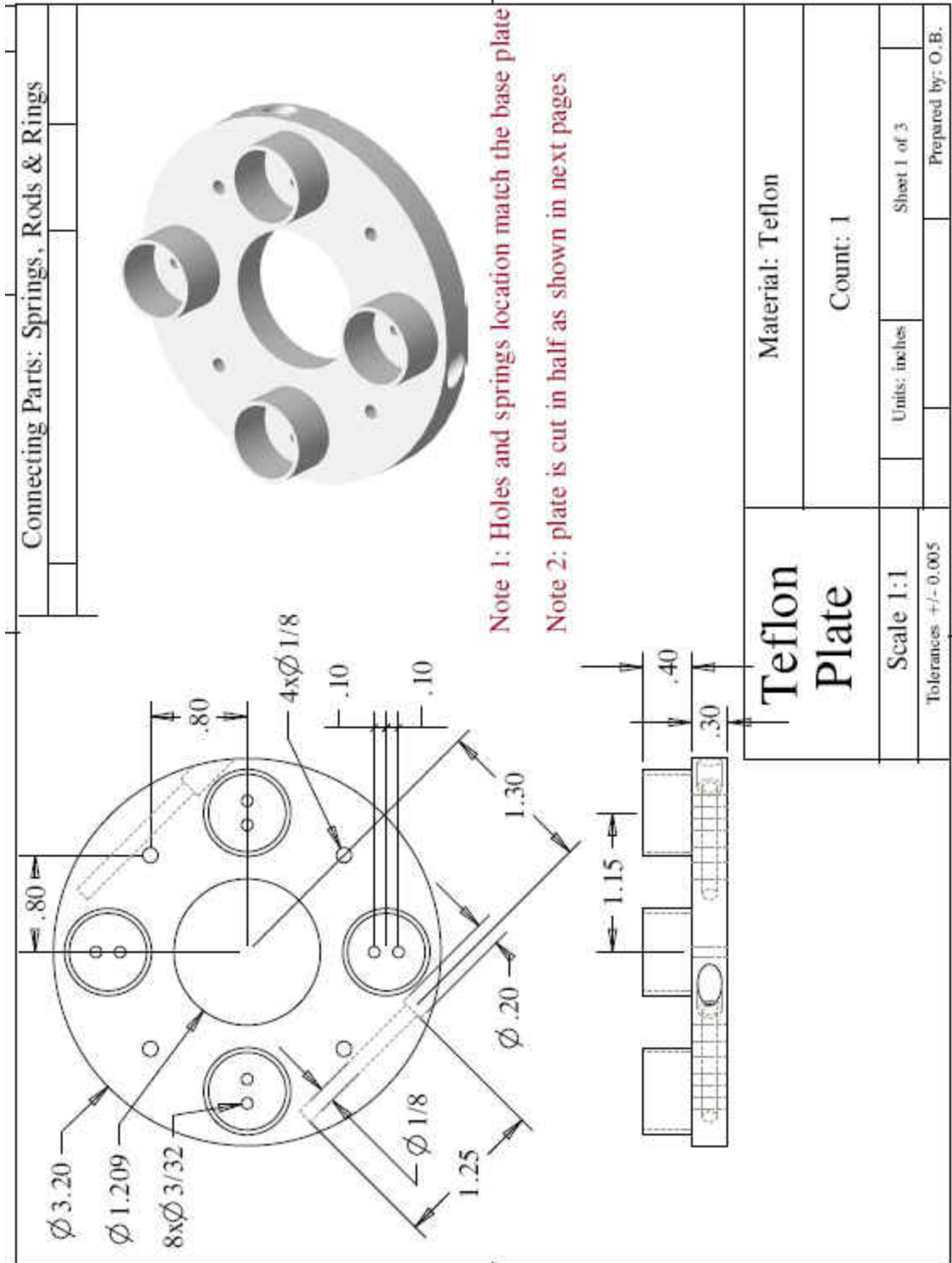


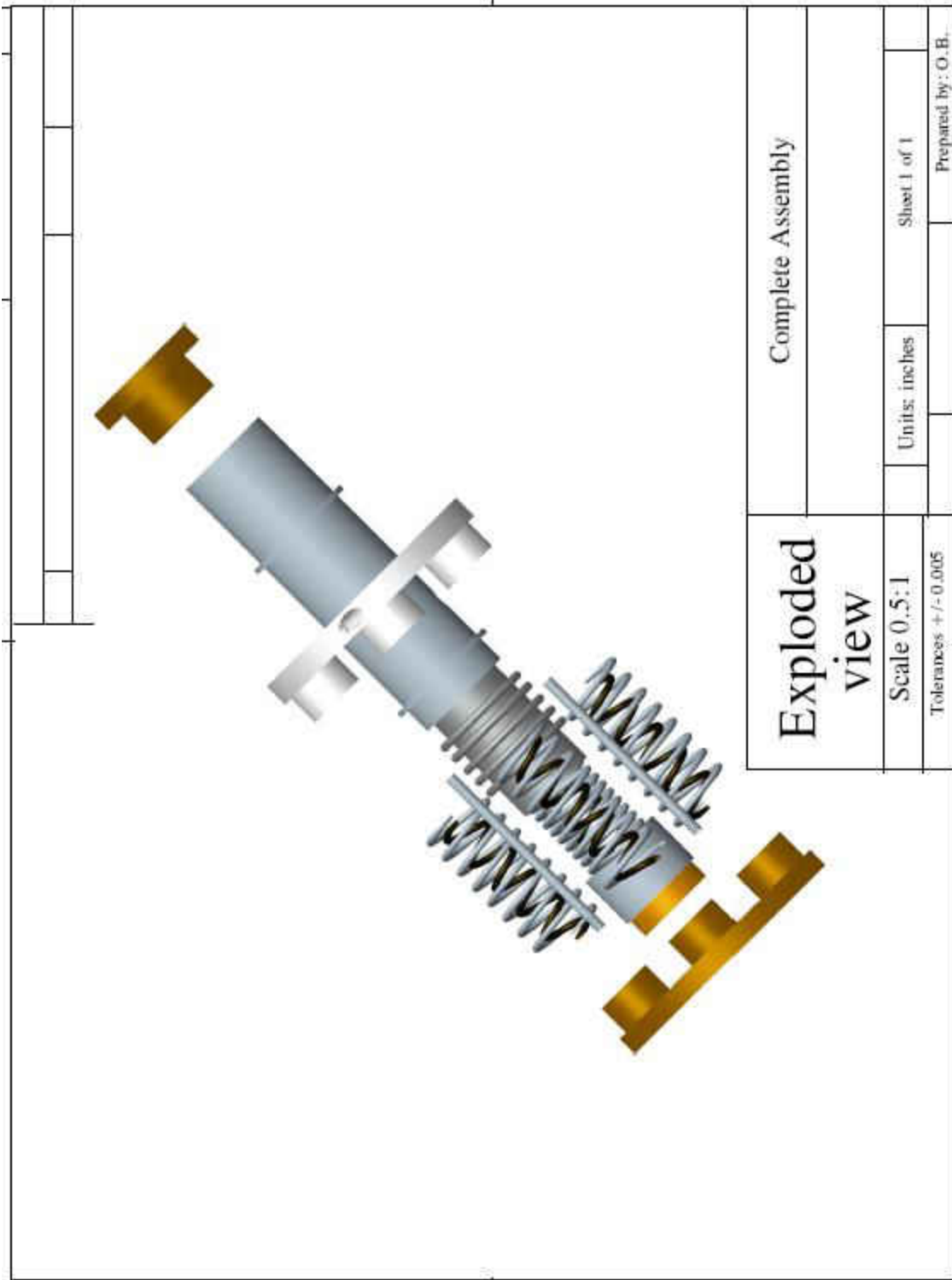
Bias Spring		Material: Stainless Steel	
		Count: 4	
Scale 1:1	Units: inches	Sheet 1 of 1	
Tolerances +/- 0.005		Prepared by: O.B.	

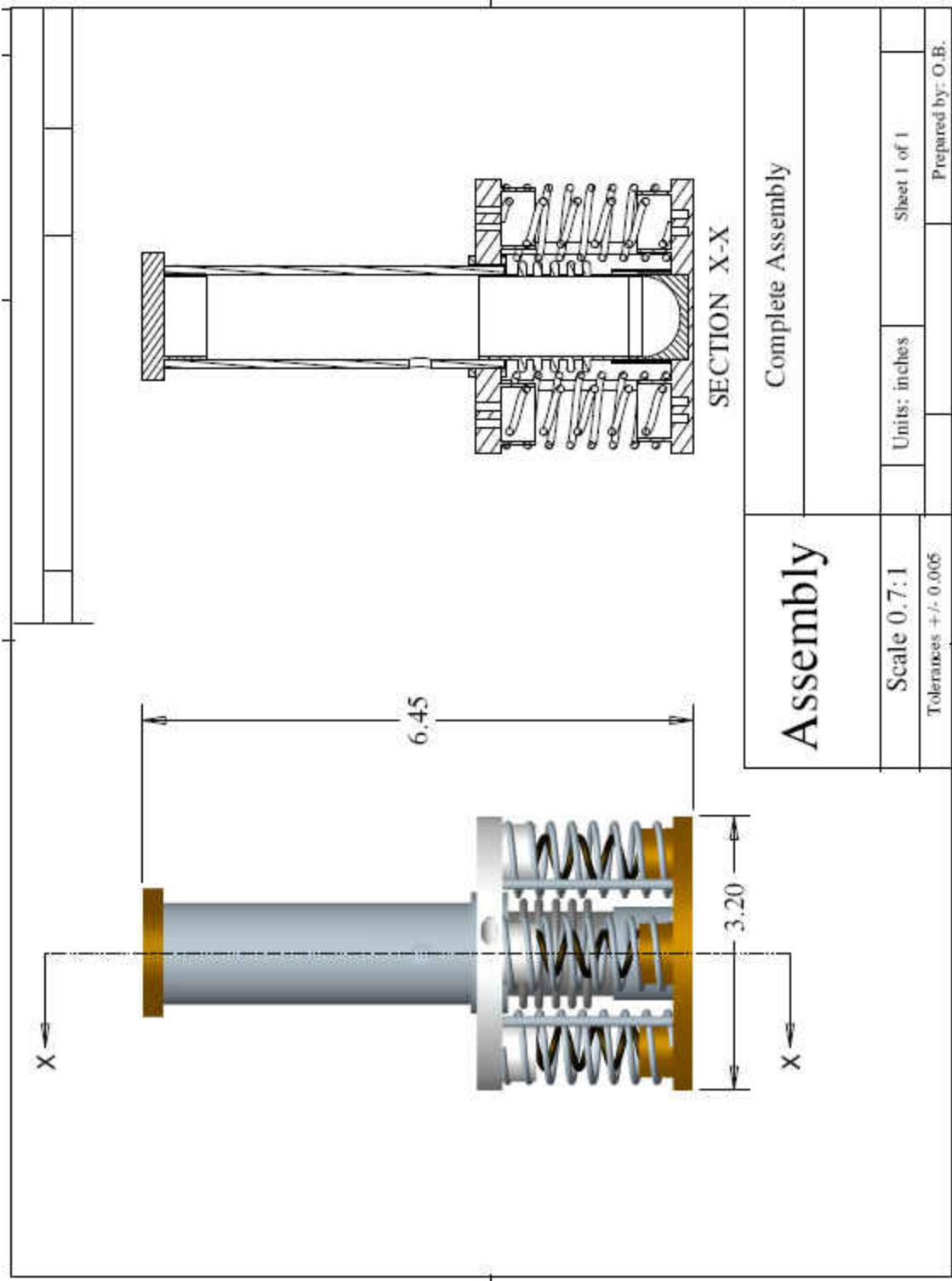


Half Teflon Plate	Material: Teflon		
Scale 1:1	Count: 1		
Tolerances ± 0.005	Units: inches	Sheet 2 of 3	Prepared by: O.B.



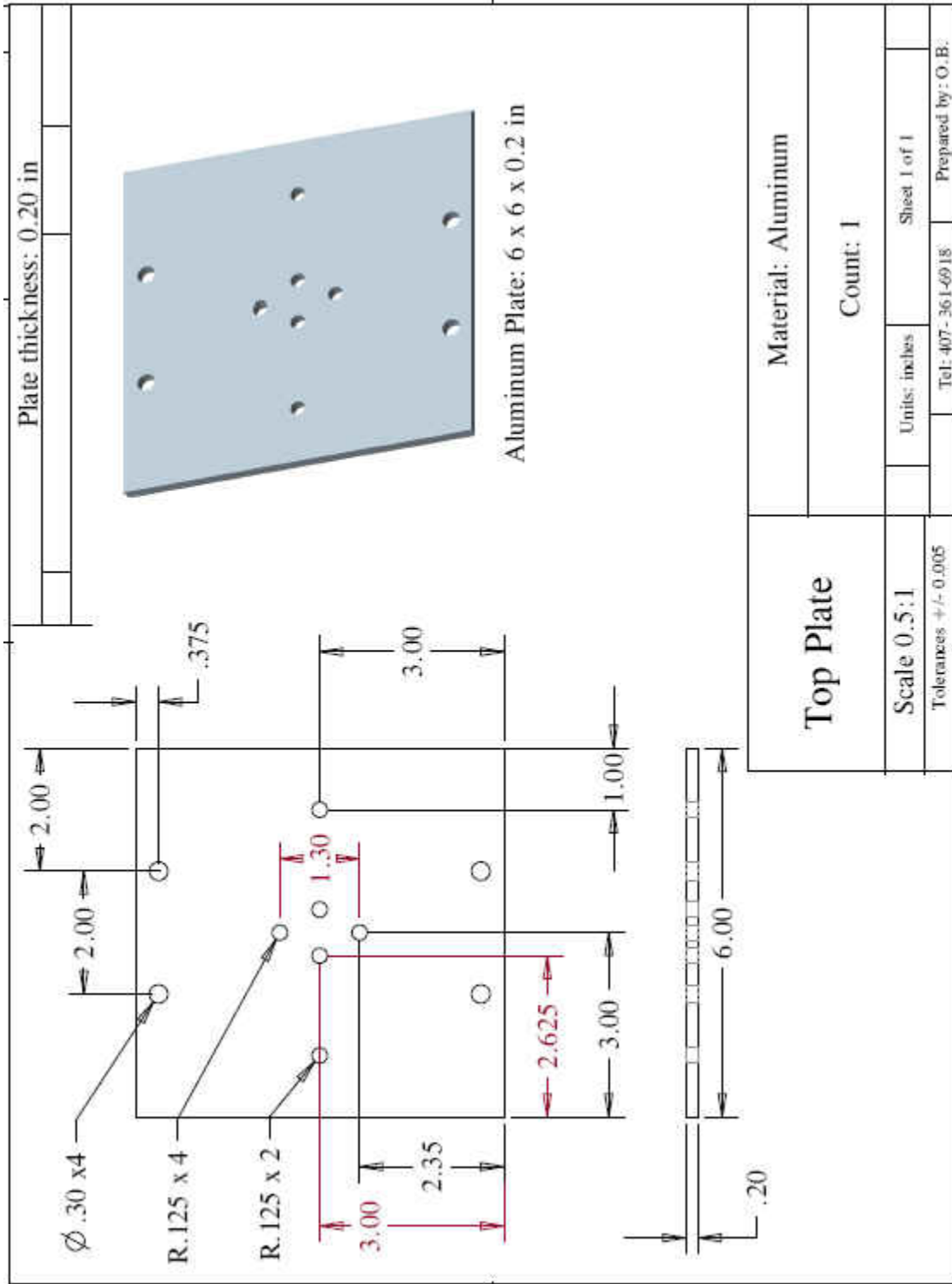




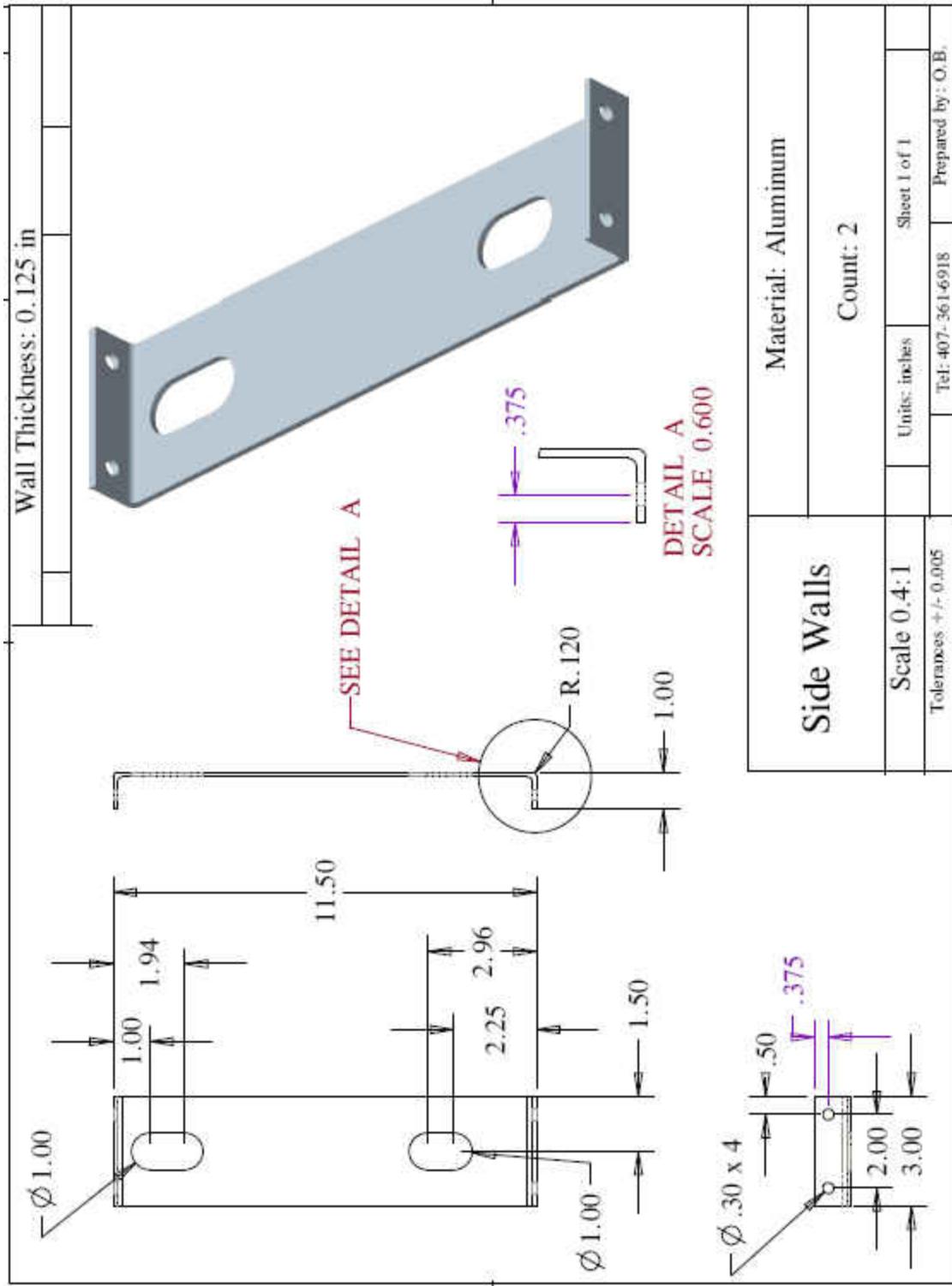


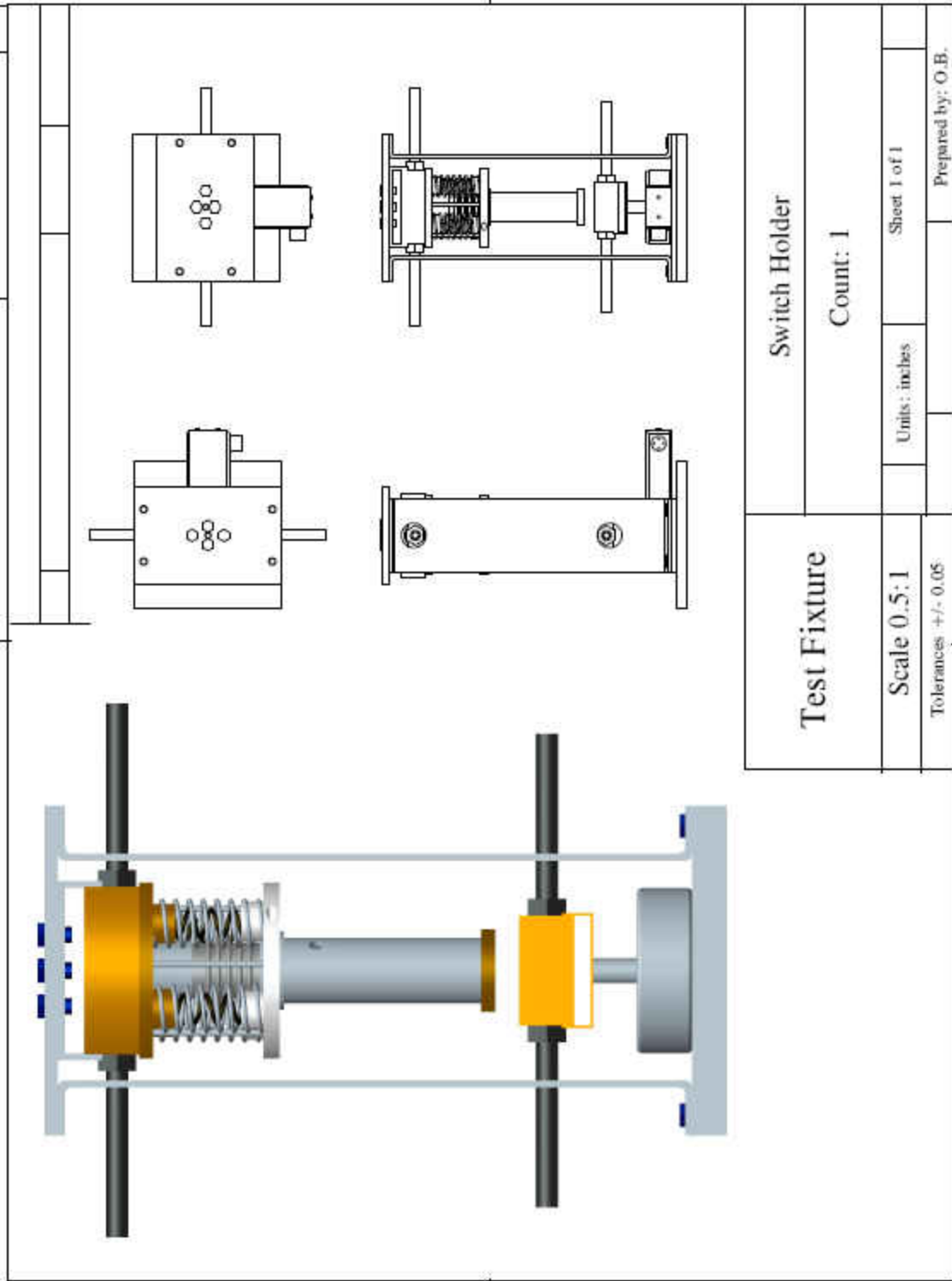
Assembly		Complete Assembly	
Scale 0.7:1	Units: inches	Sheet 1 of 1	
Tolerances +/- 0.005		Prepared by: O.B.	

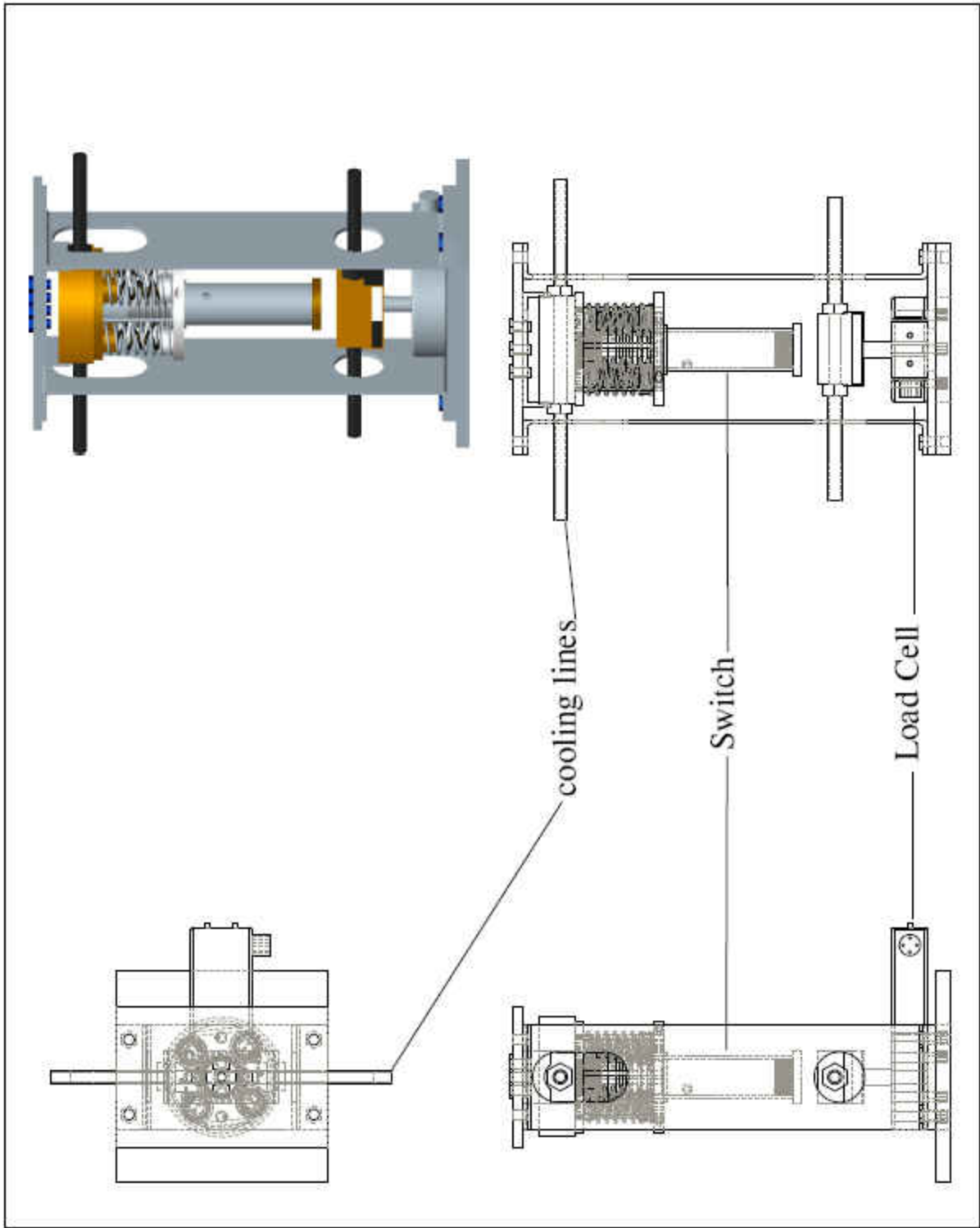
Test Stand Machine Drawings



Top Plate		Material: Aluminum	
		Count: 1	
Scale 0.5:1		Units: inches	Sheet 1 of 1
Tolerances +/- 0.005		Tel: 407-361-6918	Prepared by: O.B.







REFERENCES

- [1] Donabedian M., *Spacecraft Thermal Control Handbook*. Cryogenics Vol. II Cryogenics. 2003, Virginia: The Aerospace Press.
- [2] Duband L., A thermal switch for use at liquid helium temperature in space borne cryogenic systems. In Proc. 8th Int. Cryocooler Conf.(Colorado 1994). 1995. New York: Plenum Press.
- [3] Catarino I., Bonfait G., and Duband L., Neon Gas-Gap Heat Switch. *Cryogenics*, 2008. **48**: p. 17-25.
- [4] Frank D. J. and Nast T. C., Getter-activated cryogenic thermal switch. *Advances in Cryogenic Engineering*, 1986. **31**: p. 933-940.
- [5] Delaey L., et al., Review--Thermoelasticity, pseudoelasticity and the memory effects associated with martensitic transformations--Part 2: The macroscopic mechanical behavior. *Materials Science*, 1974. **9**: p. 1536-1544.
- [6] Duerig T. W., et al., *An Introduction to Martensite and Shape Memory*, in *Engineering Aspects of Shape Memory Alloys*. 1990, Butterworth-Heinemann: London.
- [7] McCormick P. G. and Y. Liu, Thermodynamic analysis of the martensitic transformation in NiTi--II. Effect of transformation cycling. *Acta Metallurgica et Materialia*, 1994. **42**(7): p. 2407-2413.
- [8] Miyazaki S., Igo Y. and Otsuka K., Effect of thermal cycling on the transformation temperatures of Ti--Ni alloys. *Acta Metallurgica*, 1986. **34**(10): p. 2045-2051.
- [9] Otsuka K. and Ren X., Martensitic transformations in nonferrous shape memory alloys. *Materials Science and Engineering A*, 1999. **273-275**: p. 89-105.
- [10] Perkins J., et al., *Thermomechanical characteristics of alloys exhibiting martensitic thermoelasticity*. *Shape Memory Effects in Alloys*, ed. P. J. 1976, New York: Plenum Press.
- [11] Funakubo H., *Shape Memory Alloys*. 1987, New York: Gordon and Breach.
- [12] Goo, E., et al., Mechanical twinning in Ti₅₀Ni₄₇Fe₃ and Ti₄₉Ni₅₁ alloys. *Acta Metallurgica*, 1985. **33**(9): p. 1725-1733.
- [13] Hwang C. M., Salamon M. B. and Wayman C. M., Transformation Behaviour of a Ti₅₀Ni₄₇Fe₃ Alloy: III. Martensitic Transformation. *Philosophical Magazine A*, 1983. **47**: p. 177-193.

- [14]Hwang, C.M. and Wayman C.M., Compositional dependence of transformation temperatures in ternary TiNiAl and TiNiFe alloys. *Scripta Metallurgica*, 1983. **17**(3): p. 381-384.
- [15]Leclercq S., et al., Thermodynamical modeling of recovery stress associated with R-phase transformation in TiNi shape memory alloys. *Materials Transactions JIM*, 1994. **35**: p. 325-331.
- [16]Miyazaki S. and Otsuka K., Deformation and transition behaviour associated with the R-Phase in TiNi alloys. *Metallurgical and Materials Transactions A*, 1986. **17A**: p. 53-63.
- [17]Krishnan, V.B., et al., Analysis of neutron diffraction spectra acquired in situ during mechanical loading of shape memory NiTiFe at low temperatures. *Materials Science and Engineering: A*, 2008. **481-482**: p. 3-10.
- [18]Lemanski, J.L., et al., A Low Hysteresis NiTiFe Shape Memory Alloy Based Thermal Conduction Switch. *AIP Conference Proceedings*, 2006. **824**(1): p. 3-10.
- [19]Krishnan, V.B., et al., A THERMAL CONDUCTION SWITCH BASED ON LOW HYSTERESIS NITIFE SHAPE MEMORY ALLOY HELICAL SPRINGS. *AIP Conference Proceedings*, 2008. **986**(1): p. 3-9.
- [20]Olander A., *J. Amer. Soc.*, 1932. **54**: p. 3819.
- [21]Greninger A. B. and Mooradian V. G., *trans. AIME*, 1938. **128**: p. 337-341.
- [22]Buehler W. J. and Wang F. E., A Summary of Recent Research on the Nitinol Alloys and their Potential Application in Ocean Engineering. *Ocean Eng.*, 1967. **1**: p. 105-120.
- [23]Melton K. R., ed. *General applications of shape memory alloys and smart. Shape Memory Materials*, ed. Otsuka K. and Wayman C. M. 1999, Cambridge University Press: Cambridge 220-239.
- [24]Schwartz M. M., *New Materials Processes, and Methods Technology*. 2006: Taylor and Francis. 217-233.
- [25]Pitt D. M., Dunne J. P., and White E. V., Design and Test of a SMA Powered Adaptive Aircraft Inlet Internal Wall. In 43rd AIAA/ASME/ASCE/AHS/ASC Structures, Structural Dynamics, and Materials Conference 2002. Denver, Colorado: AIAA.
- [26]Mabe J. H., Calkins F., and Butler G., Boeing's variable geometry chevron, morphing aerostructure for jet noise reduction. In 47th AIAA/ ASME/ ASCE / AHS / ASC Structures, Structural Dynamics and Materials Conference. 1997. Newport, Rhode Island.
- [27]Cross W.B., Kariotis A.H. and Stimler F.J., September 1969, NASA.

- [28]Miyazaki, S., et al., J. De Phys., 1982. **43**(12).
- [29]Fan, G., et al., Origin of abnormal multi-stage martensitic transformation behavior in aged Ni-rich Ti-Ni shape memory alloys. Acta Materialia, 2004. **52**(14): p. 4351-4362.
- [30]Khalil Allafi, J., Ren X., and Eggeler G., The mechanism of multistage martensitic transformations in aged Ni-rich NiTi shape memory alloys. Acta Materialia, 2002. **50**(4): p. 793-803.
- [31]Stuart R. W., Wakefield, and Hogan W. H., *Thermal Switch for Cryogenic Apparatus*. 1969: USA.
- [32]Catarino, I., et al., Gas gap thermal switches using neon or hydrogen and sorption pump. Vacuum, 2009. **83**(10): p. 1270-1273.
- [33]Altoz F. E. and Porter F., *Thermal Switch*. 1976: USA.
- [34]Otsuka K. and Wayman C. M., *Shape Memory Materials*. 1999, Cambridge: Cambridge University Press. p. 240-266.
- [35]Stebner A, et al., Development, characterization, and design consideration of Ni_{19.5}Ti_{50.5}Pd₂₅Pt₅ high temperature shape memory alloy helical actuators. Journal of Intelligent Material System and structures (in print), 2009.
- [36]Alghamdi S. A., A computer algorithm for the static analysis of circular helicoidal bars. Comput. Struct, 1991. **43**: p. 151-157.
- [37]Ancker C. J. Jr. and Goodier J. N., Theory of pitch and curvature corrections for helical spring-I (tension). J. Appl. Mech., 1958. **25**: p. 471-479.
- [38]Ancker C. J. Jr. and Goodier J. N., Pitch and curvature corrections for helical spring. J. Appl. Mech., 1958. **25**: p. 466-470.
- [39]Kamiya N. and Kita E., Boundary element method for quasi-harmonic differential equation with application to stress analysis and shape optimization of helical springs. Comput. Struct., 1990. **37** (1): p. 81-86.
- [40]Cook R. D., Finite element analysis of closely-coiled springs. Comput. Struct., 1990. **34**: p. 179-180.
- [41]Jiang W. G. and Henshall J. L., A novel finite element for helical springs. Finite Elements Anal. Design, 2000. **35**: p. 363-377.

- [42]Taktak M., et al., A mixed-hybrid finite element for three-dimensional isotropic helical beam analysis. *Int. J. Mech. Sci.*, 2005. **47** (2): p. 209-229.
- [43]Tautzenberger P., ed. *Thermal Actuators: A Comparison of Shape Memory Alloys with Thermostatic Bimetals and Wax Actuators*. ed. Duerig T W, et al. 1990, Butterworth-Heinemann: London. 207-218.
- [44]Hearn E. J., *Mechanics of Materials - An Introduction to the Mechanics of Elastic and Plastic Deformation of Solids and Structural Materials (3rd Edition)*. Vol. 1. 1997: Elsevier. 297-325.
- [45]Wahl A. M., *Mechanical Springs*. 1963, New York: McGraw-Hill.
- [46]Hearn E. J., *Mechanics of Materials - An Introduction to the Mechanics of Elastic and Plastic Deformation of Solids and Structural Materials (3rd Edition)*. Vol. 1. 1997: Elsevier. 176-198.
- [47]Liang C. and Rogers C. A., One-dimensional thermomechanical constitutive relations for shape memory materials. *Journal of intelligent Material System and structures* 1990. **2**(1).
- [48]Hodgson D. E., "Using Shape Memory Alloys", *Shape Memory Applications*. 1988.
- [49]Bejan A. and Kraus A. D., *Heat Transfer Handbook*. 2003, NY: John Wiley & Sons. pp. 1181-1229.
- [50]Lock G. S. H., *The Tubular Thermosyphon*. 1992: Oxford University Press.
- [51]Lock G. S. H. and Fu, Observations on an evaporative elbow thermosyphon. *Journal of Heat Transfer*, 1993. **115**: p. 501-503.
- [52]Cheng K. C. and Zarling J. P., Applications of heat pipes and thermosyphons in cold regions. In *Proceedings of the 7th international heat pipe conference*. May 1990. Minsk.
- [53]Harley C. and Faghri A., Complete transient two-dimensional analysis of two-phase closed thermosyphon including the falling condensate film. *Journal of Heat Transfer*, 1994. **116** (2): p. 418.
- [54]Gross U., *Reflux Condensation heat transfer inside a closed thermosyphon*. *International Journal of Heat and Mass Transfer*, 1992. **35** (2): p. 279-294.
- [55]Faghri A., Chen M. M. and Morgan M., Heat transfer characteristic in two-phase closed conventional and concentric annular thermosyphon *Journal of Heat Transfer*, 1989. **111**: p. 611-618.

- [56]Feldman K. T., Investigation of passive pressure-pumped thermosyphons. In Proceedings of the 6th international heat pipe conference. 1987. Grenoble, France.
- [57]Shiraishi M., Influences of evaporator geometry on performance limits in two-phase closed thermosyphon. In Proceedings of the 6th international heat pipe conference. 1987. Grenoble, France.
- [58]Shiraishi M., Yoneya M. and Yabe A., Visual study of operating limit in the two-phase closed thermosyphon. In Proceedings of the 5th international heat pipe conference. 1984. Tokyo.
- [59]Wang J.Y., et al., Performance evaluation of cell-based algorithms for domain decomposition in flow simulation. International Journal of Numerical Methods for Heat and Fluid Flow, 2008. **18**(5): p. 657-71.
- [60]Tabatabai A. and Faghri A., A new two-phase flow map and transition boundary accounting for surface tension effects in horizontal miniature and micro tubes. Journal of Heat Transfer, 2001. **123**: p. 958-968.
- [61]Wang J. Y. and Vafai K., An experimental investigation of the transient characteristics on a flat plate heat pipe during startup and shutdown operations. Journal of Heat Transfer, 2000. **122**: p. 525-535.
- [62]Nukiyama, S., The maximum and minimum values of the heat Q transmitted from metal to boiling water under atmospheric pressure. International Journal of Heat and Mass Transfer, 1966. **9**(12): p. 1419-1433.
- [63]Drew T. B. and Mueller A. C., *Boiling*. Transactions of AIChE, 1937. **33**: p. 449-471.
- [64]Yang, S. A. and Hsu C. H., Free- and forced-convection film condensation from a horizontal elliptic tube with a vertical plate and horizontal tube as special cases. International Journal of Heat and Fluid Flow, 1997. **18**(6): p. 567-574.
- [65]Shiraishi M., Kikuchi K., and Yamanishi T., eds. Investigation of heat transfer characteristics of a two-phase closed thermosyphon. Advances in Heat Pipe Technology, ed. Reay D A. 1981, Pergamon Press: New York. 95-103.
- [66]Lee Y. and Mital U., A two-phase closed thermosyphon. International Journal of Heat and Mass Transfer, 1972. **15**(9): p. 1695-1707.
- [67]Noie, S.H., Heat transfer characteristics of a two-phase closed thermosyphon. Applied Thermal Engineering, 2005. **25**(4): p. 495-506.

- [68] Rohsenow W. M., A method of correlating heat transfer data for surface boiling curves. *International Journal of Heat Transfer ASME*, 1962. **84**: p. 969.
- [69] Shalaby M. A., et al. Heat transfer performance of a two-phase closed thermosyphons. In *Proceedings of 6th International Heat Pipe Symposium*. 2000. Chiang Mia.
- [70] Farber E. A. and Scora E. L., *Trans. ASME*, 1948. **70**: p. 369.
- [71] Incropera F. P., Dewitt D. P., and Bergman T L, *Fundamentals of Heat and Mass Transfer*. 2007: John Wiley & Sons, Inc. p.629.
- [72] Nusselt W., Die oberflächen kondensation des wasserdampfes. *Zeitschrift des Vereines Deutscher Ingenieure*, 1916. **60**: p. 541-546.
- [73] Rosenhow W. M., Heat transfer and temperature distribution in laminar-film condensation. *Transactions of ASME*, 1956. **78**: p. 1645-1648.
- [74] Collier J. G., *Convective Boiling and Condensation*. 1981, London: McGraw-Hill.
- [75] Imura H., et al., Heat transfer in two-phase closed-type thermosyphons. *Transactions of Japan Society of Mechanical Engineers*, 1977. **22**: p. 485-493.
- [76] Faghri A., *Heat Pipe Science and Technology*. 1995, Washington, DC: Taylor & Francis. 221-245.
- [77] Uehara H., et al., Filmwise condensation for turbulent flow on a vertical plate. *Heat Trans.-Jpn. Res.*, 1983. 12((2)): p. 85-96.
- [78] Sparrow E. M. and Gregg J. L., A boundary-layer treatment of laminar film condensation. *Journal of Heat Transfer*, 1959. **81**: p. 13-18.
- [79] Chen M. M., An Analytical Study of Laminar Film Condensation: Part 1- Flat Plate. *Journal of Heat Transfer*, 1961. **83**: p. 48-54.
- [80] Dunn P D and Reay D A, *The heat pipe*. *Physics in Technology*, 1973. **4**: p. 187-201.
- [81] Faghri, A. and Thomas S., Performance characteristics of a concentric annular heat pipe: Part 1 - Experimental prediction and analysis of the capillary limit. *Journal of Heat Transfer (Transactions of the ASME)* 1989. **111**(4): p. 844-850.